Hox Genes And Tonotopic Organization Of Auditory Brainstem Circuits

Inauguraldissertation

zur

Erlangung der Würde eines Doktors der Philosophie

vorgelegt der

Philosophisch-Naturwissenschaftlichen Fakultät

der Universität Basel

von

Kajari Karmakar

aus Indien

Basel, December 2016

Genehmigt von der Philosophisch-Naturwissenschaftlichen Fakultät auf Antrag von

Prof. Dr. Filippo M. Rijli

(Dissertationsleiter)

Dr. J. F. Brunet

(Korreferent)

Basel, den 09 Dezember, 2014

Prof. Dr. Jörg Schibler

(Dekan)

Table of Contents

Summary

The formations of functional neuronal circuits are achieved through multiple developmental processes, beginning at neuronal progenitor specification and establishment of topographic connectivity to refinement of topographic circuits and synaptic maturation of the circuits. Though, most of the underlying neuronal connectivity in different circuits have been identified, the molecular mechanisms guiding the establishment and refinement of their input-output topographic relay, are largely unknown. Refinement and maturation of topographic connectivity is essential in the visual system (Huberman et al., 2008), the somatosensory system (Fox et al., 2005) as well as in the auditory system (Kandler et al., 2009). During my Ph.D, I studied two different neuronal circuits, one addressing the development of tonotopic organization in auditory sensory circuits; and the other unraveling the neuroanatomical pathways in whisker related sensori-motor interactions and whisker movements.

The auditory system has a unique topographic organization, such that all auditory nuclei represent a gradient of frequencies and two neighboring bands of neurons respond to neighboring sound frequencies. Such an organization with an orderly representation of frequencies is called tonotopy and tonotopic organization is essential for efficient discrimination of sound frequencies (Kandler et al., 2009). The tonotopic organization of the auditory nuclei are considered to be developmentally hardwired, however, elaborate processes of refinement are essential to achieve the precision of the adult tonotopic circuits (Kandler et al., 2009; Clause et al., 2014). The brainstem auditory circuits, which consist of the cochlear nucleus (CN) and the superior olivary complex (SOC) are also tonotopically organized. The CN is further subdivided into the anterior ventral cochlear nucleus (AVCN), posterior ventral cochlear nucleus (PVCN) and the dorsal cochlear nucleus (DCN). The AVCN arises from rhombomeric progenitor zones, r2-r3, which are characterized by the combinatorial expression of Hox paralogous group 2 genes (*Hox PG2*), *Hoxa2* and *Hoxb2* (Narita and Rijli, 2009; Di Bonito et al., 2013). Hox genes are determinants of topographic information and influence topographic organization as well as topographic input-output connectivity of several hindbrain nuclei (Philippidou and Dasen, 2013). In our present study, we investigate the role of *Hox PG2* genes in the tonotopic organization of the brainstem auditory circuits, with focus on AVCN.

Our results suggest an essential role of *Hox PG2* genes in the maturation and refinement of the tonotopic organization and connectivity of the AVCN. Using conditional deletions of *Hox PG2* genes targeting the post-mitotic bushy cells in the AVCN, we show that the gross tonotopic organization of the AVCN, which is established very early during development, is unaffected. However, processes involving refinement of the tonotopic organization are impaired in the absence of the *Hox PG2* genes. In the *Hox PG2* mutants, peripheral afferents of the spiral ganglion (SG) neurons target less precisely, resulting in a broader spread of targeting bands in the AVCN. These aberrant SG projections are not developmentally refined and are still maintained in the adult mutants as observed in the auditory pure tone stimulation experiments. Pure tone auditory stimulations activate broader bands with larger number of activated neurons in the mutants. The broadening of the activated bands leads to reduced separation (also overlap) between bands of activated neurons responding to two neighboring sound frequencies. This results in a decreased resolution of the tonotopic organization in the AVCN, affecting sound frequency discrimination in the *Hox PG2* conditional mutants. In an auditory tone based discriminating fear conditioning experiment, the *Hox PG2* mutants are unable to distinguish between two close sound frequencies, compared to the controls. To explore the molecular mechanisms underlying the described phenotype, we performed a transcriptome analysis on the mutant AVCN bushy cells. Our results showed a deregulation of acvitity associated genes and synapse associated genes in the absence of *Hox PG2* genes. Thus, we looked into the development of synapses between the SG afferents and the AVCN bushy cells, the giant Endbulb of Held synapses. The Endbulb of Held synapse maturation occurs in an activity dependent manner involving elimination of multi-axonal inputs to retain 1-2 major inputs, in the weeks after hearing onset. Our analysis showed that synaptic maturation of the Endbulb synapses were affected and the mutant Endbulbs receive higher numbers of SG axonal inputs. Thus, our results show that conditional deletion of *Hox PG2* genes in specific subsets of AVCN neurons affects several late developmental refinement processes, culminating in loss of resolution of tonotopic precision and reduction in sound frequency discrimination.

In addition to the above described study, this thesis manuscript also includes another study (currently in press, *European Journal of Neuroscience*) done in collaboration with Varun Sreenivasan from Prof. Carl C. Petersen's group, EPFL,

Switzerland. In this study, we map the neuronal pathways connecting cortical inputs to hindbrain facial motor nucleus (FMN), driving peripheral facial muscles in the mouse whisker system. We investigate how cortical inputs from motor cortex (M1) and somatosensory cortex (S1) interact with premotor and motor nuclei in the hindbrain, while driving different whisker movements. We identify distinct subsets of premotor nuclei associated with whisker retraction and whisker protraction, which receive differential cortical inputs from S1 and M1, respectively. Our results suggest two parallel pathways through which M1 driven whisker protraction and S1 driven whisker retraction are actuated. Thus, in this study, we further the understanding of the anatomical pathways underlying whisker movements.

Abbreviations

SG:	spiral ganglion
CN:	cochlear nucleus
CF:	characteristic frequency
AN:	auditory nerve
VCN:	ventral cochlear nucleus
DCN:	dorsal cochlear nucleus
BCNC:	brainstem cochlear nucleus complex
SOC:	superior olivary complex
LSO:	lateral superior olive
MSO:	medial superior olive
MNTB:	medial nucleus of trapezoid body
MGN:	medial geniculate nucleus
AVCN:	anterior ventral cochlear nucleus
PVCN:	posterior ventral cochlear nucleus
SBC:	spherical bushy cell
GBC:	gloubular bushy cell
r :	rhombomere
PG:	paralogous group
BrdU :	Bromodeoxyuridine
NMDAR:	N-methyl-D-aspartate receptor
AMPAR:	alpha-amino-5-methyl-4-isoxazolepropionic acid receptor
PrV:	principal nucleus of trigeminal V
SpV:	spinal trigeminal nucleus V
S1:	somatosensory cortex
M1:	motor cortex
FMN:	facial motor nucleus
vFMN:	vibrissal facial motor nucleus
MOC:	medial olivocochlear system

Chapter 1. Introduction

Part 1: Mammalian auditory system

1.1 The central auditory pathways

Hearing or audition is one of the most important sensations. The proper development of functional sensory pathways involved in audition is essential for communication. Sound is produced by vibrations that result in alternate compression and rarefraction of air. These vibrations are detected by the auditory receptors in the inner ear cochlea and transduced into neural activity. In mammals, sound is directed via the outer and middle ear components into the inner ear cochlea (**Fig. 1**), which consists of the basilar membrane, the Organ of Corti, located on the basilar membrane and the tectorial membrane.

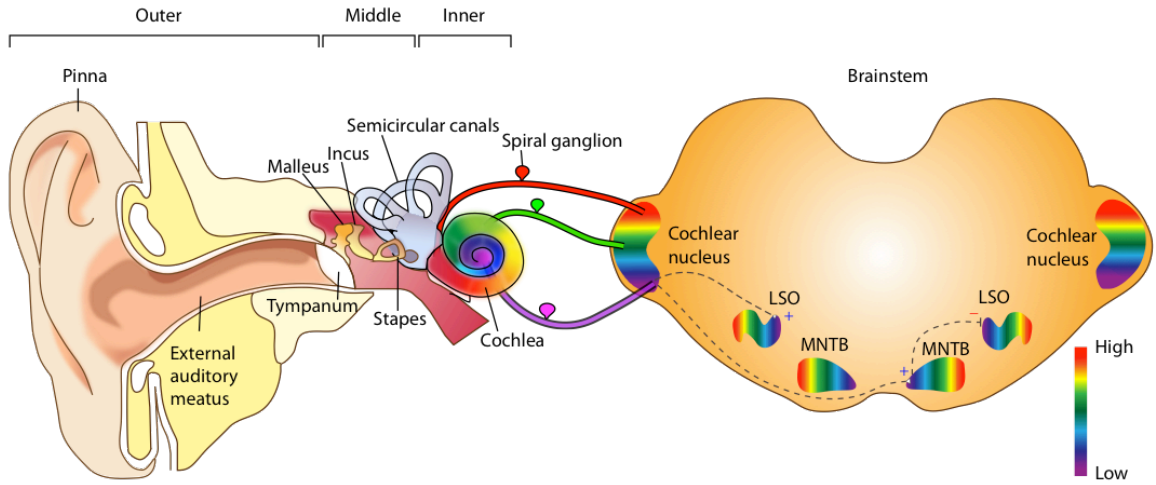

Fig. 1: Peripheral to central connectivity in auditory system: The peripheral auditory system consists of the Outer, Middle and Inner ear. The cochlea in the inner ear has a tonotopic organization (in different colors), which is relayed by the axons of the bipolar spiral ganglion neurons to the Cochlear nucleus (CN) in the brainstem. The CN sends excitatory inputs to LSO and MNTB. CN, LSO and MNTB are all tonotopically organized.

The hair cells on the organ of Corti are the sensory receptors for sound stimuli (**Fig. 2, A**). Hair cells are polarized epithelial cells, which have modified microvilli called 'sterocilia' on their apical ends that are in contact with the tectorial membrane. The displacement of the basilar membrane in relation to the tectorial membrane, in response to sound waves results in the displacement of the stereocilia and subsequent

depolarization of the hair cells. This in turn elicits an action potential in the afferent nerve terminal of the spiral ganglion (SG) neuron in contact with the base of the hair cell (**Fig. 2, A, B**). The action potential is conducted via the central axonal projections of the bipolar SG neurons to the first brainstem auditory nuclei, the cochlear nucleus (CN). These axons of the spiral ganglion neurons projecting to the hindbrain together form the auditory nerve (AN) (**Fig. 1**).

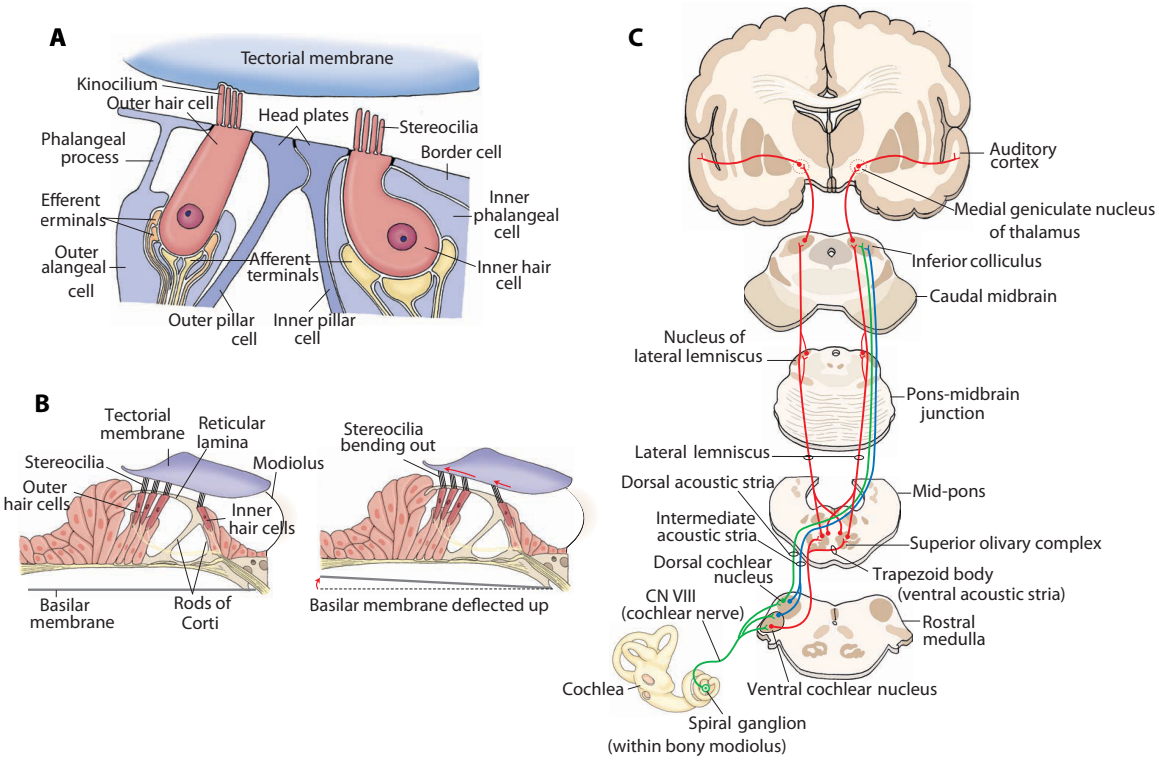

Fig. 2: Functional units in the cochlea and auditory relay system: (A) The hair cells on the basilar membrane are the sensor for sound frequencies. They have numerous stereocilia on their apical ends that are in contact with the tectorial membrane. (B) Displacement of the sterocilia due to sound induced displacement of the basilar membranes results in depolarization of hair cells and generation of action potentials (C) The acoustic information is relayed from the periphery by the CN and several hindbrain and midbrain nuclei to the auditory cortex. (Images taken from Essential Neuroscience, 3rd edition, Pg: 291, 292, 294)

The CN in the rostral hindbrain is the first relay station of the brainstem auditory circuits. The CN is composed of two main sub-divisions, ventral cochlear nucleus (VCN) and the dorsal cochlear nucleus (DCN), together referred to as the brainstem cochlear nuclear complex (BCNC). The second order neurons of the CN project to various higher order nuclei in the brainstem and the caudal midbrain, such as the superior olivary complex (SOC), (lateral and medial superior olive, LSO, MSO and medial nucleus of trapezoid body, MNTB) and the inferior colliclulus. The third order

neurons from the SOC and trapezoid body project to the ipsilateral and contralateral lateral lemniscus at the pons-midbrain junction. The lateral lemniscus then projects to the inferior colliculus in the midbrain, which in turn projects to the medial geniculate nucleus (MGN) in the caudal thalamus. The MGN projects to the primary auditory cortex (**Fig. 2, C**). All these central auditory nuclei share a common feature in their organization, i.e, 'tonotopy' or the spatial arrangement of sound frequencies.

1.2 Tonotopy: Fundamental principle of organization in the auditory system

Tonotopy is a fundamental organizing principle of the auditory system (Kandler et al., 2009). Tonotopy arises from the orderly representation of sound frequencies (low-high or vice versa) in a nucleus, such that tones close to each other in terms of frequency are represented in topologically neighboring regions in the brain. Also called cochleotopy, it begins at the basilar membrane in the cochlea.

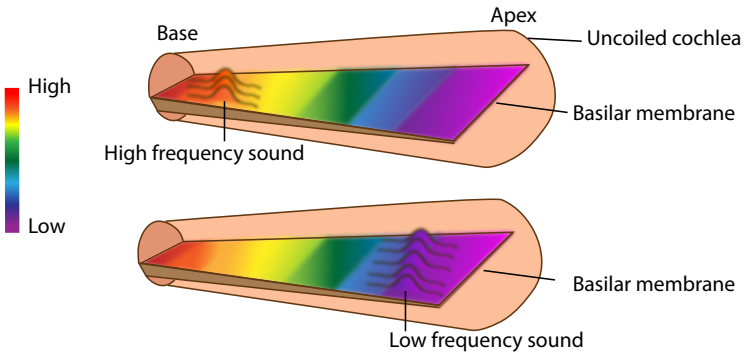

Fig. 3: Tonotopy in basilar membrane: The basilar membrane vibrates with a different characteristic frequency (CF) along its entire length. CFs are higher at the base of the basilar membrane than at the apex. High sound frequencies displace maximally the basal ends of the basilar membrane (top panel) while low sound frequencies displace maximally the apical end (bottom panel).

The basilar membrane, due to its lengthwise variation in width and thickness, vibrates with a different characteristic frequency at different positions along its length, such that points responding to high frequencies are located at the base of the basilar membrane, whereas, points responding to low frequencies are at the apex (**Fig. 3**). Hair cells located at the base of the basilar membrane are concomitantly activated by high sound frequencies, whereas, hair cells located in the apical end of the basilar membrane are activated in response to low sound frequencies (Mann and Kelley, 2011). This tonotopic arrangement in the periphery is relayed via the central axons of the SG neurons targeting the CN; such that SG afferents activated by high frequencies target the dorsal part of the CN and subsequent lower frequencies are conveyed to the ventral

part of the CN (**Fig. 1**). Such topographically restricted inputs result in formation of isofrequency bands, within which all neurons respond to a specific characteristic frequency (Kandler et al., 2009). This spatially segregated representation of sound frequencies is an important basis for auditory sound frequency processing and in sound frequency discrimination, and is maintained at all levels in the central auditory system.

1.3 The cochlear nucleus complex

The CN is the main relay station coupling the peripheral auditory inputs with the central auditory circuits. The fibers of the SG axons synapse onto the principal neurons of the CN to form different types of synapses encoding different information about the perceived sound (Rubel and Fritzsch, 2002). The CN consists of two broad subdivisions, the dorsal cochlear nucleus (DCN) and the ventral cochlear nucleus (VCN), which is further subdivided into antero-ventral cochlear nucleus (AVCN) and posterior-ventral cochlear nucleus (PVCN). These nuclei together are called the brainstem cochlear nuclear complex (BCNC). The ascending branches of the SG afferents bifurcate at the base of the VCN, sending an ascending branch to the AVCN and a descending branch to the PVCN and DCN (Young and Oertel, 2003, 2010). All divisions of the BCNC are tonotopically organized along their dorso-ventral axis, with low frequencies mapping at the ventral part and high frequencies mapping at the dorsal part of the nucleus (**Fig. 4, A**).

On the basis of cytoarchitectural criteria, ventral cochlear neurons can be classified into five main neuronal types (**Fig. 4, B**): spherical bushy cells (SBC) found in the rostral AVCN, globular bushy cells (GBC) found in the caudal AVCN and PVCN, octopus cells in the caudal PVCN, multipolar stellate cells and small cells that are dispersed throughout the VCN and granule cells that mainly forms the boundaries between VCN and DCN and are scarcely scattered throughout the core of the VCN (Young and Oertel, 2003, 2010). All the different cell types vary in their electrophysiological properties as well as in their neuronal connectivity. Amongst the various CN cell types, the bushy cells have been extensively studied.

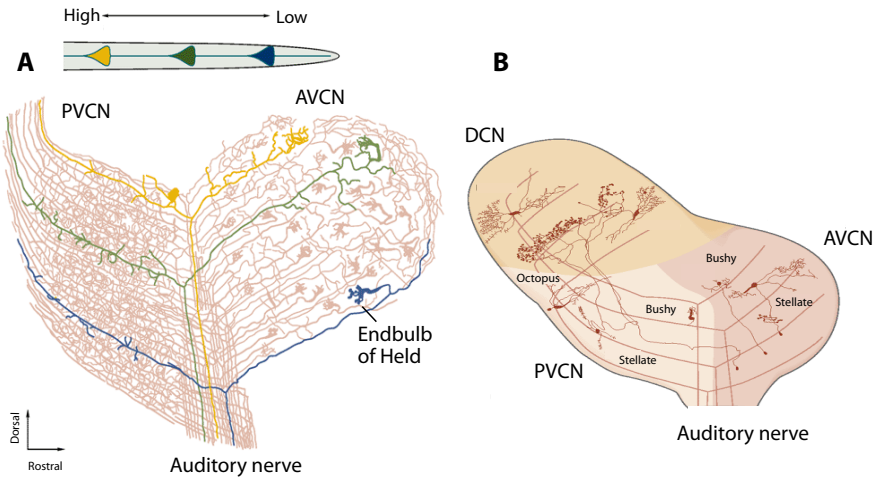

Fig. 4: Tonotopic organization of SG afferents in CN: (A) VCN is divided into AVCN and PVCN. The SG afferents target the dorso-ventral axis of the CN in a tonotopic order. SG axons form giant calyceal synapses in anterior AVCN, called Endbulb of Held. (B) Distribution of the CN neuronal subtypes in different subdivisions of the CN. (Images from Principles of neural science, Fifth edition, Pg: 688)

Due to many unique bushy cell membrane properties and interaction with AN inputs, bushy cells are capable of transmitting precise temporal information, necessary for both high and low frequency sound localization. They show primary-like responses to pure-tone stimulation. The bushy cells receive large axosomatic terminals from the SG afferents, forming either one gigantic calyceal synapse called the Endbulb of Held on the SBCs or a small number of smaller synapses called 'modified' Endbulbs on the GBCs (Rubel and Fritzsch, 2002). The axons of the SBCs project ipsilaterally to the LSO and bilaterally to the MSO, whereas, the axons of the GBCs project to the contralateral MNTB (Kandler et al., 2009). The axons of the GBCs form giant axosomatic synapses called Calyx of Held on the principal neurons of the MNTB (Borst and Soria van Hoeve, 2012).

1.4 Development of hindbrain auditory circuits

1.4.1 Rhombomeric origin of brainstem auditory complexes

Spatiotemporal origin

During embryonic development, the hindbrain is transiently segmented along its anterior-posterior axis into germinal zones, called 'rhombomeres' (r), containing heterogeneous progenitor cell pools (**Fig. 5, A**). In rodents, eight transient rhombomeres (r1-r8) give rise to cerebellum (r1) and several brainstem nuclei (r2-r8) (Philippidou and Dasen, 2013; Kiecker and Lumsden, 2005).

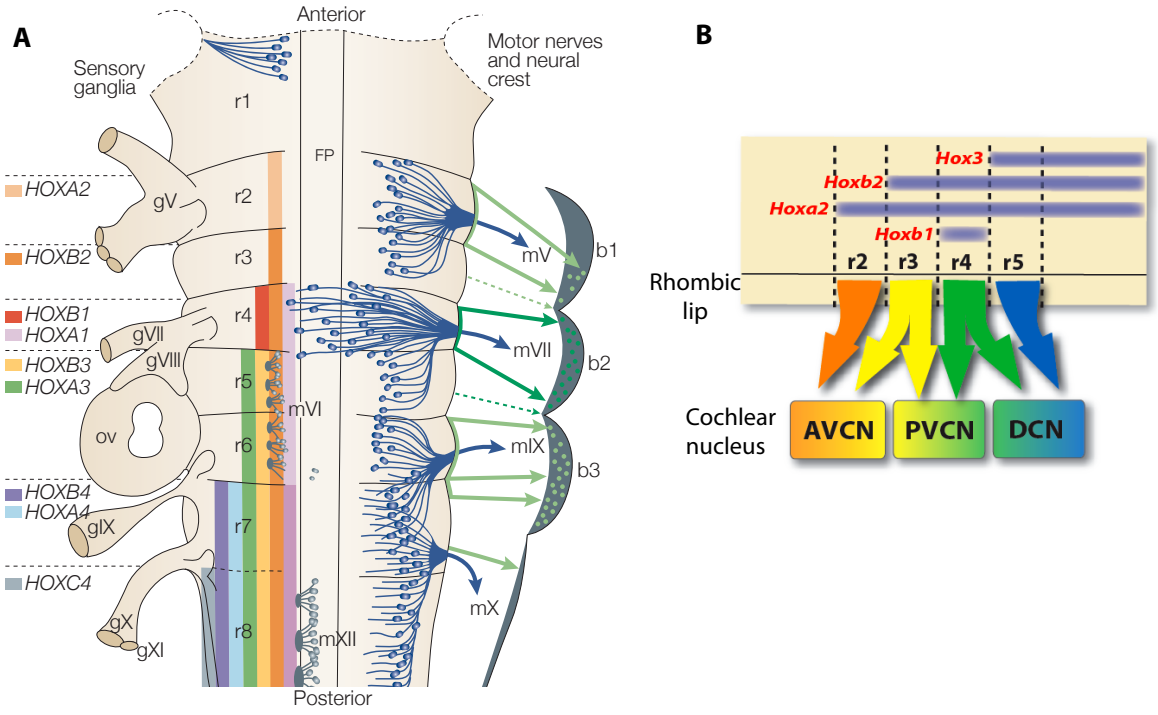

Fig. 5: Rhombomere formation and patterned Hox genes expression: (A) The hindbrain is transiently divided into compartments of progenitor pools called rhombomeres. Rhombomeres are characterized by combinatorial expression of Hox genes. Specific progenitor pools within the rhombomeres give rise to different sets of sensory and motor nuclei in the hindbrain (B) Rhombomeric origin of the subdivisions of the CN and the corresponding Hox gene expression patterns in the rhombomeres. (Images: (A) from Kiecker and Lumsden, 2005; (B) adapted from Farago et al.,2006).

Subtractive fate mapping studies in mice have shown that the auditory brainstem nuclei derive from r2-r5 ventricular neuroepithelium (Farago et al. 2006). Furthermore, different rhombomeres give rise to different sub-divisions and neuronal subtypes in the brainstem auditory circuits, such that, r2 and r3 derived neurons form the AVCN whereas, r3-r5 derived neurons form the PVCN and the DCN (**Fig. 5, B**). The r3 predominantly give rise to glutamatergic neurons in the AVCN, r3 and r5 give rise to glutamatergic neurons in the PVCN and DCN, and in the LSO and MSO. On the other hand, r4 gives rise to GABAergic and glycinergic neurons of the PVCN and DCN and cholinergic neurons in the SOC (Di Bonito et al., 2013).

Neuronal Specification

Although the various neuronal subtypes of the CN have been identified, their developmental molecular machinery still remains elusive. Transcription factors such as

Krox20, *MafB* and *Hox* genes are expressed in the progenitors of the brainstem auditory neurons, however, their specific roles in neuronal subpopulation specification and segmentation are yet to be fully explored. Recent studies have identified specific transcription factors that specify neuronal populations based on their neurotransmitter phenotype. For example, *Math1* (*Atoh1*), a basic helix-loop-helix transcription factor, specifies progenitors giving rise to excitatory glutamatergic neurons in several brainstem nuclei (Wang et al., 2005; Maricich et al., 2009). Genetic fate mapping strategies that enable us to follow the *Math1* derived cells as they exit the rhombic lip, show that these cells contribute to the glutamatergic population in the CN, forming the spherical and globular bushy cells, octopus and T-stellate cellsin the VCN; and also the glutamatergic cells in the LSO and MSO. *Math1* is expressed at early stages of development (E 9.5 in mice) in the rhombic lip and deletion of *Math1* results in the loss of VCN, which is mainly, composed of glutamatergic neurons and partial loss of the glutamatergic neurons in the remnant DCN. Another transcription factor, *Ptf1a* is essential for specification of GABAergic and glycinergic inhibitory neurons in the CN. Null mutants of *Ptf1a* exhibit a severely disorganized DCN, whereas, the VCN remains intact (Fujiyama et al., 2009). In addition, *Math5* (*Atoh7*), downstream of *Math1*, is developmentally expressed by SBCs and GBCs, however, its specific role in cochlear neuronal maturation is yet unknown. *MafB* is also expressed during development, as well as during postnatal stages in the neurons of the VCN, but the effect of its deletion on the development of the cochlear nucleus is also not known. Thus, molecular signaling pathways involved in actuating cochlear neuronal differentiation and maturation remains a poorly understood field.

1.4.2 Involvement of *Hox* genes in patterning the cochlear nuclear complex

During embryonic development, the position of rhombomeric progenitor pools along the rostro-caudal axis of the hindbrain influences the specification of the neuronal subtypes derived from them. These positional identities of the progenitor pools are determined by nested expression patterns of homeobox transcription factors called Hox genes during embryogenesis (**Fig. 5, A**). Hox genes play a key role in conferring segmental identity and patterning information to the neuroepithelial rhombomere compartments, thus patterning the hindbrain. Furthermore, the Hox genes are critically involved in stereotyped migratory behavior of neurons and in the establishment of

spatially restricted patterns of axonal connectivity. The mammalian Hox gene family, consisting of 39 members, is organized into four clusters. Each rhombomere, except r1, is characterized by a combinatorial Hox expression code (Philippidou and Dasen, 2013; Kiecker and Lumsden, 2005, Narita and Rijli, 2009).

The brainstem cochlear nucleus arises from rhombomeric domains r2-r5. Recent study (Di Bonito et al., 2013) showed that Hox paralogous group 2 (PG2) genes: *Hoxa2* and *Hoxb2* are essential for the specification and development of the subdivisions of the VCN. *Hoxa2* is expressed mainly in r2/r3 derived AVCN, whereas, *Hoxb2* is expressed in r2/r3 derived AVCN, r4 derived PVCN, and r3/r5 derived granule cells of the CN. Both *Hox PG2* genes are expressed in the r3/r4/r5 derived DCN. Deletion of *Hoxa2* during early embryogenesis affects the AVCN, impairing the projections from its principal neurons to the contralateral MNTB. Absence of *Hoxa2* results in downregulation of Slit receptor molecule *Rig1/ROBO3* that is known to regulate the crossing of the midline by commissural axons in the hindbrain. Thus, *Hoxa2* influences the development of the hindbrain sound localization circuitry. In contrast, in the absence of *Hoxb1* and *Hoxb2*, PVCN transforms into a r3-derived AVCN and the resultant axonal projections fail to connect to their normal targets, i.e.: the r4 derived ventral lateral lemniscus and medial olivocochlear system (MOC), which are also affected in these mutants. Deletion of *Hoxb1* and *Hoxb2* also results in hearing impairments to variable severities, due to defects in efferent reflexes and innervations of the outer hair cells in the cochlea by the MOC neurons. Thus, both Hox PG2 genes play important roles in forming the CN subdivisions and in developing their functional connectivity.

1.5 Development of tonotopic organization of the brainstem auditory complexes

The tonotopic organization of all the central auditory nuclei is a fascinating feature and many attempts have been made to understand the mechanisms involved in the development of precise tonotopic maps. Unlike in many other sensory systems, the topographic mapping of the auditory circuits is highly precise even at early stages of development. Earlier studies in birds and mammals have shown that growing axons project to defined topographic positions within their target nuclei at initial stages of auditory circuit formation. However, further investigations suggest that though the tonotopic organization of auditory circuits are developmentally predetermined and

hardwired, activity dependent refinement plays a critical role in fine-tuning of the auditory connectivity achieving the astonishingly high precision of the synaptic circuits (Kandler et al., 2009, Rubel and Fritzsch, 2002). This activity dependent refinement is dependent on pruning of axonal collaterals as well as on elimination and strengthening of excitatory or inhibitory inputs that together help to decrease the degree of synaptic convergence and increase the precision of the tonotopic maps.

In the CN, the incoming afferents of the peripheral SG neurons target specific regions forming isofrequency bands along the dorso-ventral axis. The SG neurons responding to high sound frequencies target dorsal CN, while, the subsequently low frequency responding SG neurons target the more ventral parts of the CN (**Fig. 1**). The dorso-ventral targeting of the high-low frequency responding SG afferents is temporally controlled during development. High frequency sensitive SG neurons are generated earlier during development compared to the low frequency responding SG neurons, as revealed by BrdU birth-dating studies. The earlier born high-frequency sensitive SG neurons target the dorsal parts of the CN earlier than the later born low frequency sensitive SG neurons that target the ventral parts of the CN (Koundakjian et al., 2007). This temporal development of the peripheral projections relates to their spatial segregation in the CN, resulting in tonotopic organization.

Studies from tracing experiments in chick and cats as well as from deaf or hearing-impaired animals have shown that topographic organization of the SG afferents in the CN undergoes further activity dependent refinement to form the finely tuned connectivity of the adult tonotopic maps (Kandler et al., 2009). Anatomical tracing of peripheral projections from the cochlea to the CN in cats, show that tonototopically similar auditory nerve fibres terminate in well defined isofrequency bands in the cochlear nucleus in neonatal cats. With development, as the size of the cochlear nucleus increases (in adult cats), the isofrequency bands also increase; however, the proportional increase in the size of the isofrequency bands compared to the increase in the size of the cochlear nucleus was smaller (**Fig. 6**). As a consequence, the relative width of termination bands decreased, resulting in an increase in the resolution of the tonotopic map (Leake et al., 2002; Leake et al., 2006).

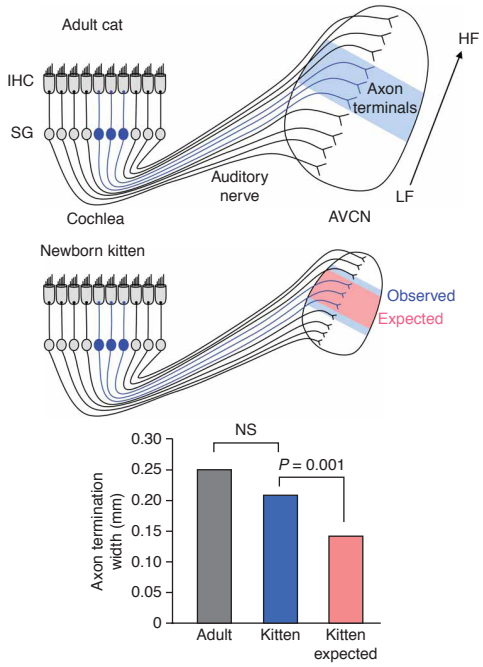

Fig. 6: The CN tonotopic map undergoes postnatal refinement: Tracing of SG afferents from the cochlea to the CN in adult cats and newborn kittens, shows that in the adult cats the projections labels a specific band (top panel), but the band labeled at the CN in newborn kitten is much broader than the band expected when compared to the result in the adult cat (middle panel). This suggests, bands in the adult cats are sharper than the bands in the kittens, suggesting refinement of the SG afferents. (Fig. from Kandler et al., 2009)

In addition to the cochlear nucleus, the tonotopic map is also known to undergo activity dependent refinement during development in the LSO and in the MNTB (Clause et al., 2014). Studies involving adult cats that were neonatally deafened showed that the auditory nerve projection to the CN was still tonotopically organized, however, the isofrequency bands in the adults were broader compared to the normal hearing adult cats (Leake et al., 2006).

Thus, the specificity of the adult tonotopic maps, which is highly essential for frequency resolution, was affected due to deprivation of auditory inputs during early neonatal stages. All these evidences together suggest that the development of the tonotopic map is a hardwired activity-independent process, however, establishment of precise tonotopic connectivity is an activity dependent process.

1.6 Role of neuronal activity in Tonotopic Refinement

Role of pre-hearing spontaneous activity

Patterned spontaneous activity before the onset of sensory experience acts as an instructive signal for the refinement of sensory circuits. In the auditory systems, spontaneous activity is generated in the pre-hearing cochlear hair cells. These hair cells fire trains of calcium action potentials that are propagated via the spiral ganglion neurons to the central auditory nuclei. This spontaneous activity is characterized by

rhythmic bursts of high levels of spike-like activity separated by periods of quiescence (Marrs and Spirou, 2012; Tritsch et al., 2010). Pre-hearing spontaneous activity is speculated to have an important role in the sharpening and refinement of tonotopic maps (Clause et al., 2014). Since, blocking of pre-hearing spontaneous activity or pre-hearing cochlear ablation results in death of spiral ganglion neurons and their synaptic targets in the cochlear nucleus, therefore, the direct involvement of pre-hearing activity in precise tonotopic circuit formation has been difficult to investigate. However, a recent study investigating the effect of changes in temporal patterns of spontaneous activity on the development of a central tonotopic map has shown that altering the patterns of firing of pre-hearing activity, results in reduced refinement in the MNTB-LSO inhibitory projections (Clause et al., 2014). In addition to reduced sharpening of the functional topography, axonal pruning, which occurs extensively in the first week after hearing onset, was also severely impaired. Thus, cochlea generated spontaneous activity patterns have important roles in precise topographic refinement of the already formed tonotopic circuitry in the hindbrain auditory nuclei.

Role of sound evoked neuronal activity

A lot has been speculated about the potential role of sound induced activity on the refinement of the tonotopic maps in the auditory nuclei. Classical studies involving abolishment of hearing by deafening show that removal of auditory inputs doesnot affect the overall tonotopic organization of the brainstem auditory nuclei but decrease the tonotopic precision and resolution. For example, sound induced activity is shown to be essential for pruning of MNTB axons targeting the LSO and in spatially restricting the dendrite of the LSO neurons along the tonotopic axis (Kandler et al., 2009). Consequently, cochlear ablation interferes with the pruning process and with the maintenance of a pruned state. Also, Endbulb of Held synapse formation that largely matures in the weeks after hearing onset also shows defects in absence of sound induced activity (Manis et al., 2012).

1.7 Endbulb of Held formation

The two types of bushy cells, spherical and globular, in the AVCN receive large auditory nerve terminals from the SG neurons, forming giant axosomatic synapses called ‘Endbulbs of Held’. These are giant high-fidelity synapses that are specialized

for temporal firing and are essential for coupling neural activity to acoustic events. They are glutamatergic and provide a coordinated release of neurotransmitter from their multiple presynaptic sites on the post-synaptic bushy cells (Manis et al., 2012; Lauer et al., 2013). Proper development and maturation of the Endbulb of Held is important for rapid, high fidelity synaptic transmission of acoustic signals, which is essential for the processing of binaural sound localization. Normally, at maturity the Endbulb engulfs more than half of the somata of the bushy cells. Studies on Endbulb inputs in mice show that SBCs in the anterior AVCN receive 1-2 auditory nerve terminals, whereas, the GBCs in the more posterior AVCN receive 3-4 auditory nerve terminals forming 'modified endbulbs' (Lauer et al., 2013).

During development, a number of auditory nerve axons compete to innervate the bushy cells and about half the number of initial innervations are retained to form the Endbulb structures. Studies from chick auditory system show that normal development of the Endbulb is accompanied by competitive elimination of cochlear nerve axons by 50% and retention of 1-2 cochlear nerve axons to form the giant calycine endbulbs (Jackson and Parks, 1982). This is also associated with reduction of branching of the cochlear nerve axons and functional synapse elimination. Neurons in the chick cochlear nucleus (NM) undergo a dramatic pruning of dendrites and axonal inputs, resulting by late embryonic stages in two-three large endbulb terminals on each nearly adendritic bushy cell body in a one axon-one cell body ratio. This axonal pruning and synapse elimination is an activity dependent process, which largely depends on the transition from the slow NMDA receptor mediated synaptic currents to fast AMPA receptor mediated synaptic currents. For instance, weak synapses, which are likely to be eliminated, have a higher proportion of NMDA-R and a sharply reduced AMPA-R quantal size (Lu and O.Trussel, 2007).

The development of the specialized Endbulb morphology is an elaborate process that takes place mainly through the second to eight postnatal weeks (approximately 2 months) in mice (Limb and Ryugo, 2000). Though the Endbulb formation already begins at a pre-hearing stage but the complete maturation of the Endbulb complex structure requires sound-evoked activity. During early postnatal days, the Endbulbs appear as a simple, small bouton. During the next two weeks, the boutons increase in size forming a cage like ending with filopodial extensions. By the fourth week, the Endbulb has several branches and acquires a more complex structure around the

postsynaptic bushy cell. By the ninth week, the Endbulbs acquire their mature structure with highly complex secondary and tertiary branching that engulfs most of the surface of the bushy cells (Limb and Ryugo, 2000). Levels of spike activity have been shown to influence the final Endbulb morphology and synaptic structure. Low levels of activity have been shown to produce more but smaller Endbulb components. Studies from deaf mice show impairment in the Endbulb formation with loss in their structural complexity (Limb and Ryugo, 2000). Similar observations are made with congenitally deaf mice and deaf white cats that show reduced and less complex branching and smaller than normal Endbulb structures (Ryugo et al., 1997).

The development of the Endbulb is also accompanied by changes in the intrinsic membrane properties of the postsynaptic bushy cells. In the bushy cells, there is a decrease in the synaptic currents mediated by NMDARs (N-methyl-D-aspartate receptors) and an increase in the components mediated by the fast AMPARs (alpha-amino-5-methyl-4-isoxazolepropionic acid receptors) resulting in faster rise and decay times of post synaptic currents. This results in a dramatic increase in the frequency of the miniature synaptic events, indicative of the formation of additional release sites at the enlarging Endbulbs (Lu and O.Trussel, 2007). Thus, the maturation of the pre-synaptic Endbulb and the postsynaptic bushy cells goes concomitantly during refinement, but their interdependence is large unknown.

1.8 Effector molecules involved in BCNC formation and connectivity

A few axon guidance-signaling molecules have been implicated in the proper formation of the brainstem auditory circuitry. The principal neurons of the MNTB receive their inputs from bushy cells in the contralateral VCN forming giant synaptic terminals called Calyx of Held (Borst and Soria van Hoeve, 2012). The axons of the tonotopically organized VCN bushy cells course through a complex path, past the ipsilateral MNTB, across the midline, into the topographically appropriate region of the contralateral MNTB. Two axon guidance pathways have been to direct the targeting of the MNTB neurons by the contralateral VCN axons, Robo3/Rig1 and Eph/Ephrin-b mediated signaling pathways. Genetic deletion of Robo3/Rig1, which codes for a transmembrance receptor essential for the axonal crossing of the midline, causes VCN axons to form aberrant calyces exclusively in the ipsilateral MNTB. Further, these calyces are functionally abnormal suggesting that axonal pathfinding decision also

influences the synaptic maturation of the circuit (Mikalski et al., 2013). Also, Hoxa2 has been shown to regulate Robo3/Rig1 expression in the VCN, such that a conditional deletion of Hoxa2 with a developmentally early Cre driver, $Wnt1^{Cre}$ decreases the Robo3/Rig1 expression in the cochlear column, resulting in a partial defect in the midline crossing with a few VCN axons innervating also the ipsilateral MNTB (Di Bonito et al., 2013).

Eph b2/Ephrin b2 pathways have also been shown to modulate tonotopic organization and axonal pathfinding in the auditory brainstem. Mutant mice with reduced Ephrinb2 (heterozygous mutants) show an increased positional spread of c-Fos activated cells in the DCN, when subjected to an auditory pure tone stimulation experiment, suggesting a role for Ephrinb2 in the topographic mapping of the CN connectivity. In addition, Ephrinb2 heterozygous also have a defective CN-MNTB connectivity (Miko et al., 2007). The VCN axons in the Ephrinb2 heterozygote mutants form Calyces on the ipsilateral MNTB, in addition to the contralateral MNTB (Hsieh et al., 2011). The ipsilateral Calyces are not removed at later stages and morphologically mature just like their contralateral counterparts. Similar aberrant ipsilateral terminations and Calyces are also observed in *Ephb2*-/-; *Ephb3*-/- compound mutants. Furthermore, Eph/Ephrin signaling has also been shown to be involved in circuit formation in the auditory midbrain, as well as, in frequency tuning in the auditory cortex (Cramer and Gabriele, 2014; Intskirveli et al., 2011).

Part 2: Mouse mystacial system

Vibrissae or whiskers are specialized hairs on the snouts of animals that detect tactile information from the environment. The whiskers are essential for navigation and exploration in certain nocturnal animals, such as rodents. Mice and rats extensively rely on whisker acquired tactile sensory information to explore their environment, as well as to find food. During exploratory whisking, the whiskers are moved forward and backward at very high frequency. As the moving whisker comes in contact with an object, it bends and exerts force within the whisker follicle. This in turn, opens stretch-activated ion channels driving action potential firing in the whisker sensory neurons. Sensory information from the whisker is conveyed by the infraorbital component of the trigeminal nerve through the peripheral sensory neurons of the trigeminal ganglion to the hindbrain sensory nuclei of the trigeminal system, the Principal nucleus V (PrV) in the rostral hindbrain and the Spinal Trigeminal Nuclei V (SpV) in the caudal hindbrain. From the brainstem, the sensory information is forwarded via the trigeminal thalamo-cortical pathway to the somatosensory cortex (S1), also called the barrel cortex. Further, the whisker related sensory information is sent from the brainstem nuclei to several downstream pathways, such as trigemino-tectal/-collicular, trigemino-facial and trigemino-pontine/-cerebellar/-olivary pathways. These interconnected-areas together control the whisker-sensorimotor coordination and sensory perception (Petersen, 2014; Erzurumlu et al., 2010).

In contrast, the movements of the whiskers are controlled by the motor cortex (M1). Cortical control of whisker movement is mediated via the facial nerve (Cranial nerve VII) in the perphery. The facial nerve is composed of the axons of the cholinergic motor neurons located in the lateral facial motor nucleus (FMN), also called vibrissal facial motor nucleus (vFMN), in the ventral hindrain. The facial motor nerve terminals innervate the muscles of the whiskerpad and instruct whisker movements (Berg and Kleinfeld, 2003). The output of the vFMN is modulated by its interactions with many premotor centres throughout the brain, which in turn receive instruction from the whisker motor cortex (wM1) (Matyas et al., 2010). Rhythmic whisking in mice and rats consists of two steps: protraction, driving the whisker forward and retraction, driving the whisker and the whiskerpad backward (**Fig. 7**). Both these steps are controlled by activation of separate regions in the mouse wM1 and are mediated through separate groups of motor neurons in the facial motor nucleus. Also, separate

groups of premotor circuitry and peripheral muscles are associated with these opposing whisker movements (Matyas et al., 2010, Takatoh et al., 2013).

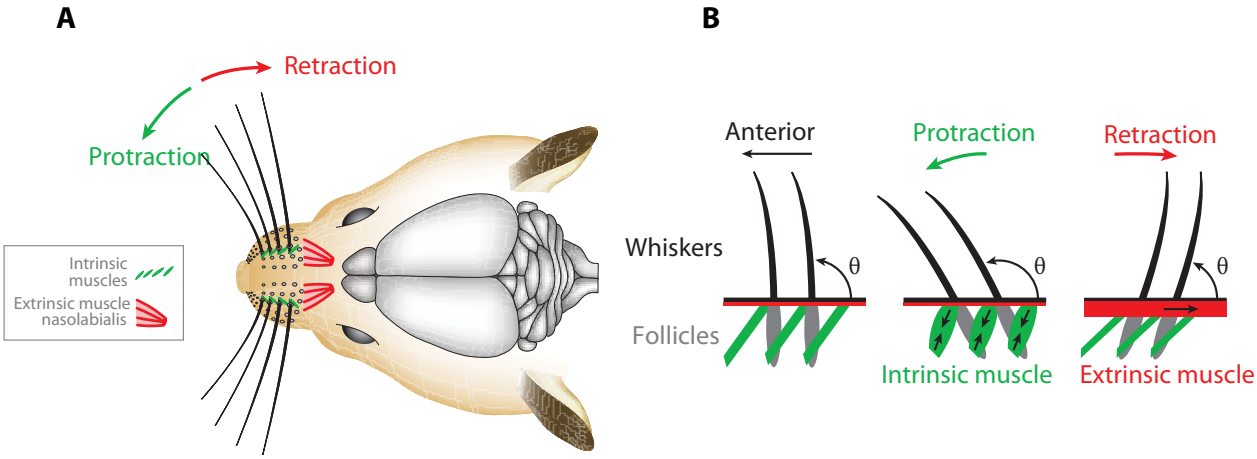

Fig. 7: Mechanism of whisker movement: (A) Whiskers are large, rigid modified hairs present on the snout of mice. Whisker movement consists of an active protraction phase, followed by either a passive retraction or an active retraction phase. (B) Muscular control of whisker movements; Intrinsic muscles associated with each whisker follicle moves the whisker forward producing protraction. Extrinsic muscles move the whiskers and the whisker pad backward, producing retraction. (Image from Petersen, 2014)

2.1 Whisker organization and Whisker-pad musculature in mice

Studies from rodents reveal that whiskers are organized in a topographic array on the snout or the whisker pad. The typical organization of the whiskers consists of four straddlers (alpha-delta) and five rows (A-E) of whiskers. In mice, the first two rows consist of 4 whiskers and the remaining rows consist of 7 whiskers, all organized into arcs (Haidarliu et al., 2010) (**Fig. 8**). This topographic organization of the whiskers on the peripheral whiskerpad is essential to topographically relay sensory information to the trigeminal brainstem nuclei (Erzurumlu et al., 2010), as well as, in the organization of pools of facial motor neurons, innervating each whisker follicle (Petersen, 2014). Whisker movement is controlled by a set of muscles present in the whisker pad musculature. These muscles can broadly be classified into two groups: intrinsic muscles and extrinsic muscles. Intrinsic muscles are associated with the vibrissal follicles and partially with the corium, but not directly attached to the skull. The intrinsic muscles are organized as slings around the whisker follicle and their contraction results in a

forward rotation of the whisker producing protraction (**Fig 7, B**). In contrast, extrinsic muscles originate on the skull or on the nasal cartilage and insert into the mystacial pad from different directions. One of the major sets of extrinsic muscles is the *M. nasolabialis,* originating from the orbital surface of the frontal bone, caudal to the nasofrontal suture and medial to the medial corner of the eye. Contraction of the extrinsic muscles results in backward rotation of the whisker resulting in retraction (**Fig 7, B**). Both the intrinsic and extrinsic muscles are innervated by the facial nerve, formed by the axons of the neurons in the FMN. Different sets of FMNs motor pools controlling the activation of the extrinsic and intrinsic muscles, receive different sets of subcortical and cortical inputs (Takatoh et al., 2013; Petersen, 2014).

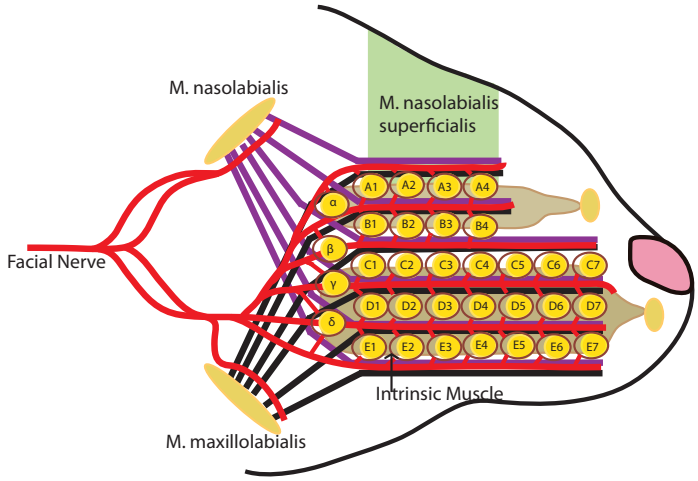

Fig. 8: Whisker arrangement and whisker related musculature: The whiskers are arranged in an array on the snout of the mice. The intrinsic muscles form a sling around the whisker follicles (labeled). Several sets of extrinsic muscles are associated with the whisker pad; amongst which M. nasolabialis forms a major set of extrinsic muscles. Different branches of the facial nerve innervate the whisker related intrinsic and extrinsic muscles.

2.2 Cortical control of whisker movement

Both primary motor cortex (M1) and somatosensory cortex (S1) has been shown to control different aspects of whisking (Matyas et al., 2010). M1 activity can initiate whisking, though additional pathways may be involved in exploratory whisking. M1 cortical neurons increase their firing rates both before the onset of whisking as well as during whisking and they modulate their firing rates in response to changes in amplitudes of whisking (Petersen, 2014). Lesion of M1, however, does not affect the normal exploratory whisking. Studies in Matyas et al., 2010, have shown that ascribed a specific role to M1 in whisker protraction. An M1 activation result in whisker protraction and the signal is relayed via the reticular formation in the hindbrain to the FMN.

S1 undergoes specific reorganization of circuits during whisking, which is not dependent on sensory inputs. Pharmacological inactivation of S1 can result in reduced whisker retraction. Further, Matyas et al., 2010, has shown that S1 inactivation reduces both S1 as well as M1 driven whisker retraction, possibly via the S1-SpVi –FMN relay pathway.

2.3 Brainstem centers of whisker movement control

Several premotor areas at subcortical levels have been identified by electrophysiological and lesion studies to control whisker motion. Retrograde labeling from the peripheral muscles has also helped to identify several hindbrain nuclei that may relay the cortical inputs from M1 and S1 to the facial motor nucleus. Monosynaptic tracing studies using glycoprotein deleted rabies virus (Takatoh et al., 2013) has identified several premotor centres in the subcortical and hindbrain regions that may modulate whisker movement, e.g., dorsal medullary reticular nucleus of the brain stem, the intermedi- ate reticular nucleus of the brain stem, the gigantocellular reticular nucleus of the brain stem, the Kolliker-Fuse nucleus, the pre-Botzinger and Botzinger complexes, the rostral part of the lateral paragigantocellular nucleus, the rostral part of the spinal trigeminal interpolaris nucleus (SP5i), the spinal trigeminal oralis nucleus, the superior colliculus, and the mesencephalic reticular nucleus (Takatoh et al., 2013). An interesting observation from the monosynaptic tracing studies was that the motor neurons controlling whisker related intrinsic muscles were strongly innervated by premotors in the IRt, whereas, the motor neurons controlling extrinsic muscles are preferentially innervated by premotor neurons in the rostral SpVi, suggesting two parallel pathways associated with whisker protraction and whisker retraction.

2.4 Transynaptic tracing with Glycoprotein-deleted Rabies virus

Recent development of the glycoprotein deleted Rabies virus (ΔG-Rabies) for neuronal tracing has helped in the identification of monosynaptic connectivity. Classical rabies tracing is limited by the continuous transynaptic spread of the rabies virus through the entire circuit, thus, hindering the identification of monosynaptic contacts (Petersen, 2014). In a modified variation of the rabies virus, the glycoprotein gene that codes for the viral coat-protein, glycoprotein is deleted and replaced by a fluorescent reporter

gene (ΔG-Rabies-EGFP/mCherry). In the absence of the glycoprotein gene, the retrograde synaptic transmission of the mutant rabies virus to the presynaptic partners is blocked. However, the rabies glycoprotein can be complemented by expression from another source, such a helper virus or by genetically induced expression in the infected cell type. This trans-complementation can enable the ΔG-Rabies to spread retrogradely into the presynaptic neurons that make direct contacts with the infected neuron. However, the further spread of the rabies virus from the first-order presynaptic neurons is inhibited by the lack of the rabies glycoprotein in the genome of the ΔG-Rabies. This serves as an effective neuronal tracing method to trace monosynaptic circuits and has been used extensively to trace premotor circuits in the spinal cord (Tripodi et al., 2012; Esposito et al., 2014). It has also been shown to work efficiently to trace the whisker premotor circuits in a previous study (Takatoh et al., 2013).

Part 3: Aim of the thesis

Complex neuronal circuits are the frameworks of the central nervous system. The study of the development of functional circuits is as interesting as unraveling the circuits themselves. My Ph.D thesis aims to address two different questions, firstly, to understand how Hox genes influence the development of functional tonotopic circuits in the brainstem auditory system; and secondly, to understand the motor and premotor pathways of whisker movements in mice.

Hox genes display versatile roles during development. They are essential for early progenitor specification as well as for functional circuit assembly. Emerging evidences also point towards late developmental roles of Hox genes in topographic maturation of neuronal circuits (Philippidou and Dasen, 2013). In the auditory system, the tonotopic organization is functionally critical for the processing of different sound frequencies. This frequency dependent topographic organization is present at all levels of the auditory system, including the brainstem cochlear nucleus (CN). The tonotopic organization of the CN is considered to be developmentally hard-wired and is present at very early stages of development (Kandler et al., 2009). Little is known about molecular mechanisms that may be involved in laying out the tonotopic map. *Hox PG2* genes, *Hoxa2* and *Hoxb2* are strongly expressed in the ventral CN (VCN) during early stages of development and previous studies have demonstrated their involvement in specification of the subdivisions of the VCN (Narita and Rijli, 2009; Di Bonito et al., 2013). *Hox PG2* genes are the only Hox genes in the anterior division of the VCN (AVCN) during early development and are also maintained till late embryonic and early postnatal stages in the AVCN, during which AVCN undergoes topographic refinement in its tonotopic organization and fine-tunes its connectivity. Since Hox genes have been shown to regulate various aspects of neural circuit formation, so we were interested in investigating the roles of *Hox PG2* genes in the development of precise tonotopic maps at the AVCN.

To this end, we generated conditional knockouts of *Hox PG2* genes in the bushy cells of the AVCN and examined the tonotopic map formation in the AVCN. Our results suggested that, though the overall topography of the AVCN was unchanged, there was a lack of refinement resulting in impaired tonotopic precision. Since tonotopic precision of the auditory circuits is essential for frequency discrimination, we next addressed whether the lack of tonotopic precision affected the functional hearing

in the mutant mice. Our auditory stimulation experiments and auditory fear conditioning experiments suggested that the *Hox PG2* conditional mutants lacked precision in their frequency representation in the AVCN and the ability to distinguish two neighboring sound frequencies was compromised in the mutants. We further explored the affected principle neurons, bushy cells, in the mutant AVCN and also found defects in synapse formation between them and presynaptic peripheral spiral ganglion (SG) afferents. Transcriptome analysis of the mutant AVCN bushy cells revealed a deregulation of genes associated with activity and synapse formation and maturation.

In the second part of my thesis, I attempted to unravel the motor control pathways of specific whisker movements. It is known that different sets of facial muscles drive whisker protraction and retraction movements. These different muscles receive inputs from different sets of motor neuron pools in the facial motor nucleus (FMN), which in turn receive cortical inputs form either M1 or S1 via different sets of premotor neurons. (Petersen, 2014; Matyas et al., 2010) Thus in this study, we (in collaboration with Varun Sreenivasan from Prof. Carl.C. Petersen's lab, EPFL, Switzerland), traced the complete neuronal pathways from the cortex to the periphery that are associated with whisker retraction and whisker protraction movements.

To this end, we coupled retrograde labeling techniques from the peripheral facial muscles with anterograde tracing from the different cortical regions. Thus, we demonstrated plausible anatomical pathways that may control whisker protraction or retraction. In addition, we also characterize the premotor circuits involved with each specific motion and verify previous published results (Takatoh et al., 2013).

Chapter 2: Manuscript in preparation

***"Hoxa2* and *Hoxb2* are required for tonotopic map precision and sound discrimination in the mouse auditory brainstem."**

Abstract

Tonotopic development of auditory circuits is a hard-wired developmental process, which is fine-tuned through elaborate activity dependent processes to achieve the precision of the adult auditory circuits. Proper topographic relay of acoustic information is essential for frequency discrimination and for sound localization. Though the underlying neuronal circuits have been partially unraveled, little is known about the molecular mechanisms involved in the topographic development and refinement of these circuits. Hox transcription factors are known determinants of topographic development of several hindbrain nuclei and their input-output connectivity. In this present study, we investigate the involvement of Hox paralogous group 2 (*Hox PG2)* genes in the development of tonotopic organization of the anterior ventral cochlear nucleus (AVCN) in the brainstem auditory circuit. Our results show that *Hox PG2* genes do not control the gross tonotopic framework of the AVCN, but control the refinement of the tonotopic organization. Conditional deletion of *Hox PG2* genes from the AVCN results in reduced resolution in the tonotopic representation, impairing the ability to discriminate close sound frequencies. Synapse formation and maturation between peripheral spiral ganglion (SG) afferents and the AVCN principal neurons is also affected in these mutants. Finally, activity related genes and synapse formation associated genes are deregulated in these conditional mutants as revealed by transcriptome analysis.

Author contribution statement: I designed and performed all the experiments (except those in Figure 2, done by Yuichi Narita), analyzed all the results and prepared the manuscript. Gene expression profiling and analysis was done in collaboration with Alberto Loche (from Rijli lab) and Genomics facility at FMI. The behavioral experiments were done in collaboration with Yuichi Narita and A. Luethi.

Hox2 Genes Are Required for Tonotopic Map Precision and Sound Discrimination in the Mouse Auditory Brainstem

Kajari Karmakar[1,2,3,*], Yuichi Narita[1,4,*], Jonathan Fadok[1], Sebastien Ducret[1], Alberto Loche[1,2], Taro Kitazawa[1], Christel Genoud[1], Thomas Di Meglio[1,5], Raphael Thierry[1], Joao Bacelo[1,6],

Andreas Lüthi[1,2], and Filippo M. Rijli[1,2,£]

[1]Friedrich Miescher Institute for Biomedical Research, 4058 Basel, Switzerland

[2]University of Basel, 4003 Basel, Switzerland

[3]Present address: Biozentrum, University of Basel, 4056 Basel, Switzerland

[4]Present address: Nagoya Bunri University, Faculty of Health and Human Life, Inazawa 492-8520, Japan

[5]Present address: Centro de Biología Molecular Severo Ochoa, Universidad Autonoma de Madrid, 28049 Madrid, Spain

[6]Present address: Brain Institute, Federal University of Rio Grande do Norte, 59056-450 Natal, Brasil

[*] These authors contributed equally to the work

[£]Correspondence and Lead Contact: filippo.rijli@fmi.ch

KEYWORDS: Tonotopic Map Formation, Homeodomain Transcription Factors, Brainstem Auditory Nuclei Development, Glutamatergic Cochlear Neurons, Bushy Cells, Endbulb of Held, Sound Frequency Discrimination, Auditory Circuit Refinement.

SUMMARY

Tonotopy is a hallmark of auditory pathways and provides the basis for sound discrimination. Little is known about the involvement of transcription factors in brainstem cochlear neurons orchestrating the tonotopic precision of pre-synaptic input. In the absence of Hoxa2 and Hoxb2 function in *Atoh1*-derived glutamatergic bushy cells of the anterior ventral cochlear nucleus, broad input topography and sound transmission were largely preserved. However, fine-scale synaptic refinement and sharpening of isofrequency bands of cochlear neuron activation upon pure tone stimulation were impaired in *Hox2* mutants, resulting in defective sound frequency discrimination in behavioral tests. These results establish a novel role for Hox factors in tonotopic refinement of connectivity and ensuring precision of sound transmission in the mammalian auditory circuit. They may also advance our understanding of the genetic basis of central auditory processing disorders.

INTRODUCTION

Tonotopy is a major organizing principle of auditory circuits (Kandler et al., 2009). Tonotopic arrangement of neuronal connectivity along the auditory pathway firstly arises from the orderly encoding of sound frequencies along the apical to basal axis of the inner ear cochlea that in turn activate specific subsets of spiral ganglion (SG) primary sensory neurons of the vestibulocochlear nerve. SG afferents relaying low-to-high sound frequencies topographically target the ventral-to-dorsal axis of the brainstem cochlear nuclear complex, forming isofrequency bands of activation of neighbor target cochlear neurons. Sound information is in turn relayed from brainstem

cochlear nuclei to midbrain, thalamus, and cortex maintaining a tonotopic organisation of connectivity at all levels of the pathway (Kandler et al., 2009).

The brainstem cochlear nuclear complex is composed of the anterior (AVCN) and posterior (PVCN) ventral cochlear nuclei, and the dorsal cochlear nucleus (DCN). Distinct cochlear nuclei are generated by different subsets of progenitors spatially segregated along the brainstem rostrocaudal axis, termed rhombomeres (r) (Di Bonito et al., 2013; Farago et al., 2006; Kiecker and Lumsden, 2005; Wang et al., 2005). The AVCN, involved in binaural sound localisation circuitry, is mostly derived from r3 with a small contribution from r2 (Farago et al., 2006; Maricich et al., 2009; Wang et al., 2005). Moreover, AVCN excitatory, glutamatergic, cells originate from the dorsal *Atoh1* expressing rhombic (auditory) lip progenitor domain (Fujiyama et al., 2009; Maricich et al., 2009; Wang et al., 2005). The auditory nerve fibers innervating the *Atoh1*-derived glutamatergic bushy cells in AVCN form large axo-somatic synaptic endings, the endbulbs of Held, ensuring the fidelity of sound transmission (Limb and Ryugo, 2000; Ryugo et al., 2006). SG axon topographic input to cochlear nuclei is developmentally hardwired before birth (Kandler et al., 2009; Koundakjian et al., 2007). Nonetheless, pre-hearing and post-hearing axon refinement and synaptic elimination play critical roles in achieving the high tonotopic precision of the mature brainstem auditory circuits (Clause et al., 2014; Kandler et al., 2009; Leake et al., 2002). Although the morphological and physiological processes leading to the development of tonotopic maps have been studied, to date no transcription factors have been identified in post-synaptic cochlear neurons that are necessary to orchestrate the fine-tuned tonotopic precision of SG afferent connectivity and synaptic development.

The homeodomain transcription factors of the *Hox* gene family are expressed in rhombomere derived mitotic progenitors and are essential for providing rostrocaudal

subtype identity to neuronal subsets contributing to sensory nuclei of multi-rhombomeric origin (Bechara et al., 2015; Di Bonito et al., 2013; Di Meglio et al., 2013; Narita and Rijli, 2009; Oury et al., 2006; Philippidou and Dasen, 2013). *Hox* gene expression is maintained in post-mitotic neurons during stereotypic migration, nuclear assembly, and establishment of broad topographic connectivity (Philippidou and Dasen, 2013). However, whether Hox factors may also be required during sensory circuit refinement and synapse maturation is unknown.

Hox paralogous group 2 (*Hox2*) genes, *Hoxa2* and *Hoxb2*, are the only *Hox* genes expressed in the AVCN, whereas in PVCN and DCN their expression overlaps with additional Hox factors (Di Bonito et al., 2013; Narita and Rijli, 2009). In AVCN, *Hox2* genes are expressed throughout its pre-natal and post-natal development and at least up to two months of age (Narita and Rijli, 2009) (Figures 1, S1A-B and S2). *Hoxa2* full deletion affected AVCN formation, due to early rhombomere progenitor repatterning (Gavalas et al., 1997). Mouse *Hoxa2* and human HOXA2 are also necessary for the morphogenesis of neural crest-derived external and middle ear structures (Alasti et al., 2008; Gendron-Maguire et al., 1993; Minoux et al., 2013; Rijli et al., 1993). Conditional ablation of *Hoxa2* in early rhombic lip progenitors did not affect AVCN formation, though resulted in reduced contralateral and increased ispilateral AVCN axon projections to the medial nucleus of trapezoid body (MNTB) due to down-regulation of the *Rig1* (*Robo3*) axon guidance receptor (Di Bonito et al., 2013). In contrast, *Hoxb2* deletion affected formation of PVCN, but not AVCN, suggesting functional redundancy with *Hoxa2* during early AVCN development (Di Bonito et al., 2013). However, these studies did not provide information about *Hox2* potential involvement in AVCN tonotopy and circuit refinement.

Here, we evaluated the developmental, morphological, molecular, functional, and behavioral consequences of the conditional inactivation of *Hox2* genes in mouse AVCN glutamatergic postmitotic bushy cells. While inner ear input broad topography and sound transmission were largely preserved, presynaptic endbulb of Held maturation and sharpening of isofrequency bands of AVCN neuron activation upon pure tone stimulation were impaired in *Hox2* mutant bushy cells. These defects resulted in degradation of tonotopic tuning of AVCN cochlear neurons and defective sound frequency discrimination in behavioral tests. Transcriptome analysis revealed that Hox2 factors may regulate expression of genes involved in target-derived signaling, adhesion, synaptogenesis, and synaptic transmission. These results provide novel insights into the role of Hox transcription factors during the development and maturation of highly topographic brainstem sensory circuits.

RESULTS

Hox2 Genes are Expressed in Glutamatergic Bushy Cells of the Anterior Ventral Cochlear Nucleus through Postnatal Stages

We generated a *Atoh1::Cre* (*Atoh1*^{Cre}) transgenic line in which *Cre* is driven by the *Atoh1* enhancer (Helms et al., 2000; Machold and Fishell, 2005) (Figure S2A). In *Atoh1*^{Cre};*ROSA*$^{(LSL)ZsGreen}$ (*Atoh1*$^{ROSA::ZsGreen}$) or *Atoh1*^{Cre};*ROSA*$^{(LSL)tdTomato}$ (*Atoh1*$^{ROSA::tdTomato}$) mice, prenatal and postnatal distribution of *ZsGreen* or *RFP* reporter expression was in keeping with the previously reported pattern for rhombic lip *Atoh1* derivatives, including cerebellar, cochlear, precerebellar and dorsal spinal cord neurons, as well as inner ear hair cells (Figures 1, S2B-C) (Machold and Fishell, 2005; Wang et al., 2005). Moreover, ZsGreen^{+} or RFP^{+} auditory neurons were glutamatergic (*vGlut2*$^{+}$) (Figure

1A), as expected for the *Atoh1*-derived lineage (Fujiyama et al., 2009). Notably, in $Atoh1^{ROSA::ZsGreen}$ or $Atoh1^{ROSA::tdTomato}$ mice no ZsGreen$^+$ or RFP$^+$ cells were found at any stage analyzed in the auditory lip progenitor domain (Figures S2C-E). *Cre* expression was barely detectable in the *Atoh1*$^+$ auditory lip and mostly restricted to postmitotic neurons ingressing the cochlear nucleus (compare Figures S2F-G). $Atoh1^{Cre}$ is therefore a suitable driver to conditionally inactivate *Hox2* genes in AVCN glutamatergic neurons while bypassing their early requirements in rhombomere patterning and mitotic progenitor specification (Di Bonito et al., 2013; Gavalas et al., 1997).

To identify *Atoh1*-derived *Hoxa2*-expressing AVCN neurons through prenatal and postnatal stages, we used an intersectional strategy and crossed $Atoh1^{Cre}$ with the $Hoxa2^{(lox-neo-lox)EGFP}$ knockin allele expressing EGFP from the *Hoxa2* locus upon Cre-mediated recombination (Pasqualetti et al., 2002) ($Atoh1^{Hoxa2::EGFP}$) (Figures 1B-D, S2H-I, S2K). In $Atoh1^{Hoxa2::EGFP}$ mice, *Cre*-induced *Hoxa2*-driven EGFP expression was only present in postmitotic AVCN neurons and not in the progenitor domain (Figures S2H-I), in keeping with the $Atoh1^{Cre}$ activity profile described above. *Atoh1*-derived *Hoxa2*-expressing EGFP$^+$ AVCN neurons co-expressed *Hoxb2* and *vGlut2* mRNA and their soma was surrounded, as assessed by immunohistochemistry, by large presynaptic VGLUT1$^+$ endings characteristic of endbulb of Held synapses (Figures 1B-D), thus identifying *Atoh1*-derived *Hoxa2*$^+$/*Hoxb2*$^+$ AVCN neurons as glutamatergic bushy cells. Neither *Hoxa2/EGFP* nor *Hoxb2* expression was detected in inner ear *Atoh1*-derived hair cells (Figures S2L-O). Moreover, in $Atoh1^{ROSA::tdTomato}$ mice no Cre-mediated excision was detected in the MafB$^+$ spiral ganglion of the inner ear, as assessed by the lack of RFP$^+$ cells (Figures S2P-R). Thus, the $Atoh1^{Cre}$ line is suitable to study the consequences of *Hox2* deletion in brainstem cochlear glutamatergic postmitotic neurons.

AVCN Size, Patterning, and Broad Connectivity Are Not Affected in *Atoh1*^{Hox2cKO} Mutants

Next, we crossed *Atoh1*^{Cre} with *Hoxa2*^{flox} and *Hoxb2*^{flox} conditional alleles (Di Bonito et al., 2013; Ren et al., 2002) and generated single *Atoh1*^{Hoxa2cKO}, *Atoh1*^{Hoxb2cKO}, and compound *Atoh1*^{Hox2cKO} conditional mutants, respectively. Quantitative PCR (qPCR) analysis of the extent of the targeted deletion in dissected cochlear nuclei from *Atoh1*^{Hox2cKO} compound mutants (see Experimental Procedures) confirmed nearly complete Cre-mediated excision of both *Hoxa2* and *Hoxb2* conditional alleles (Figures S3A-B). *Atoh1*^{Cre} driven *Hox2* single or double conditional deletions did not significantly affect AVCN size nor AVCN cell density, as compared to wild type (Figures 1E and S1C). Moreover, in single or compound *Atoh1*^{Hox2cKO} mutant fetuses *Atoh1* was normally expressed at the rhombic lip, abutting the *Lmx1b* expressing choroid plexus domain, and maintained in the developing AVCN (Figures S3C-F). *Atoh1*-derived AVCN neuron specification and postmitotic differentiation proceeded normally as assessed by expression of the bushy cell specific marker *Math5* (*Atoh7*) (Saul et al., 2008) and *MafB* (Figure S3G-J). Notably, unlike when using a mouse line expressing *Cre* at early progenitor stages (see Figures 5D,E in Di Bonito et al., 2013), in *Atoh1*^{Hox2cKO} animals *Rig1* was also normally expressed and AVCN axons projected normally to contralateral MNTB and ipsilateral lateral superior olive (iLSO) nuclei (Figures S3K-L, S-V). Furthermore, mutant AVCN displayed a normal distribution of excitatory and inhibitory neurons as assessed by expression of *vGlut1*, *vGlut2*, and *vGat* mRNA, as compared to wild type (Figures S3M-R). Thus, *Atoh1*^{Cre} driven conditional inactivation of *Hox2* genes did not affect specification, broad connectivity, or neurotransmitter phenotype of AVCN glutamatergic neurons.

Broad Tonotopic Organisation of Inner Ear Afferents is Preserved at Birth in AVCN of Single and Compound *Atoh1*^{Hox2cKO} Mutants

We then asked whether *Hox2* genes might be required in AVCN neurons to organize topographic precision of inner ear afferent tonotopic input. We inserted tiny strips of Neurovue filters coated with different lipophilic fluorescent dyes at distinct positions in the cochlear middle and basal turns of E18.5 wild type, single and *Atoh1*^{Hox2cKO} conditional mutants (Figure 2A). This allowed for focal tracing of distinct afferent subsets spatially segregated within the auditory nerve tract. We evaluated the correlation between dye angular spread in the cochlea (Figure 2A) and corresponding targeted area of labeled SG afferents along the AVCN tonotopic axis (Figure 2B). For each injection, the surface fraction of AVCN targeted by the SG afferents labeled from basal or middle cochlear turn ($S_b/S_{AVCN}*100$ and $S_m/S_{AVCN}*100$, respectively) was normalized according to the corresponding dye angular spread in the cochlea basal (θ_b) or middle (θ_m) turns ($[(S_b/S_{AVCN}*100)/\theta_b]$ and $[(S_b/S_{AVCN}*100)/\theta_m]$), respectively (Figures 2C-D).

Comparison of quantifications did not show significant alteration of cochleotopic arrangement of afferent input into E18.5 AVCN of *Atoh1*^{Hoxa2cKO} or *Atoh1*^{Hoxb2cKO} single mutants, as compared to control littermates (Figures 2C-D). In compound *Atoh1*^{Hox2cKO} E18.5 mutants, SG axons traced from basal or middle cochlear turn projected topographically along the tonotopic AVCN axis. Thus, cochleotopic organization of incoming SG fibers is not dependent on *Hox* gene expression in second order AVCN neurons, in keeping with the pre-targeting topographic ordering of SG projections (Koundakjian et al., 2007; Yu and Goodrich, 2014). However, SG axons targeted about 50% broader dorsoventral areas in *Atoh1*^{Hox2cKO} AVCN than in single mutants or controls (Figures 2C-D), suggesting that topographic precision of SG axon

prenatal targeting is in part influenced by *Hox2* expression in AVCN target neurons, with *Hoxa2* and *Hoxb2* displaying functionally redundant roles.

Tonotopic Bands of Neuronal Activation Upon Pure Tone Stimulation Are Broader in the AVCN of Adult Compound *Atoh1*^{Hox2cKO} mutants

During postnatal development, the cochleotopic map resolution increases due to refinement of functional connectivity and synapse elimination resulting in sharpening of the prenatal isofrequency bands (Clause et al., 2014; Kandler et al., 2009; Leake et al., 2002). Thus, we asked whether in adult *Atoh1*^{Hox2cKO} mutants lower tonotopic precision of SG axon targeting at birth might be rescued during postnatal refinement and whether SG afferents formed functional synapses onto AVCN bushy cells.

We subjected freely moving adult mice to pure tone auditory stimulation with 15 kHz or 8 kHz pips at 75 dB for 90 minutes in a sound proof chamber and analysed induction in AVCN neurons of the immediate early response gene c-fos (Figures 3 and S4; Experimental Procedures). In control mice, isofrequency bands of c-fos induction were detected upon 15 kHz or 8 kHz stimulation at distinct dorsoventral levels of the AVCN tonotopic axis, as assessed by immunohistochemistry or in situ hybridization (Figures 3A-C). In *Atoh1*^{Hox2cKO} double mutants, stimulation by either tone also induced distinct c-fos^{+} bands along the AVCN tonotopic axis. However, mutant c-fos^{+} bands were broader than in controls (Figures 3A-C, E-F). A similar spread of the c-fos activation area was also observed along the tonotopic (mediolateral) axis of the MNTB, directly downstream of the AVCN (Figures S4B-D). Moreover, the number of c-fos^{+} neurons activated by tone stimulation was significantly higher in the mutants (Figure S4E-F). Further supporting these findings, simultaneous stimulation with alternating 8

kHz and 15 kHz pips at 75dB for 90 minutes generated two distinct non-overlapping c-fos^{+} bands in controls whereas resulted in a large, unresolved, territory in *Atoh1*^{Hox2cKO} mutants (Figures 3D, G).

Altogether, these results suggest that individual AVCN bushy cells in *Hox2* mutants receive multiple innervations driven by distinct sound frequencies. Nonetheless, while the tonotopic precision of activity transmission was degraded, mutant AVCN readily responded to tone stimulation indicating establishment of functional synapses between SG afferents and AVCN bushy cells.

Atoh1^{Hox2cKO} Mutant Mice Fail to Discriminate Between Close Pure Tone Frequencies

Next, we asked whether the *Atoh1*^{Hox2cKO} mutant animals were capable of discriminating two close yet distinct frequencies (8 kHz and 15 kHz). We subjected control and mutant adult animals to a discriminative auditory fear conditioning paradigm (Experimental Procedures, Figure 4A and 4B). During the acquisition phase, freely moving mice were exposed in an experimental chamber to 10 pairings of two pure tones (8 kHz and 15 kHz, 30 secs each), one paired with a foot shock (conditioned stimulus) (CS+) and the other without any foot shock (CS-). To avoid any bias due to the frequency used, both 8 kHz and 15 kHz tones were used as CS+ in a counterbalanced manner for different animals. Moreover, *Atoh1*^{Hox2cKO} mutant animals and controls did not show any significant difference in behaviors that could affect the readout of the conditioning experiment, such as general mobility (i.e. distance travelled or speed of movement) or the freezing behavior itself (Figures S4G-I).

To assess the specificity of fear memory, animals were exposed to the CS+ and the CS- 24 hrs after acquisition, and stimulus evoked freezing behavior was quantified (Experimental Procedures, Figure 4A and 4B). The ratio of the percentage of freezing during CS+ and CS- (freezing CS+/ CS-) was calculated as an indication of tone discrimination (Figure 4C). Notably, the conditioned control animals exhibited significantly higher CS+/CS- discrimination ratio compared to *Atoh1*^{Hox2cKO} mutant animals (Figure 4C). Thus, tone based discriminative behavior is impaired in *Atoh1*^{Hox2cKO} mutants, supporting the c-fos activity patterns (Figure 3).

Endbulb of Held Synapse Maturation is Impaired in *Atoh1*^{Hox2cKO} Mutant AVCN Bushy Cells

In the mouse, endbulb of Held synapse development takes place postnatally during pre-hearing and post-hearing stages. At birth endbulbs appear as small boutons, which subsequently grow in size to a large calycine or club-shaped terminal, reaching their mature volume and shape by about two months of age (Limb and Ryugo, 2000). These maturation steps are accompanied by loss of axon terminal branches and reduction to only up to 1-4 terminals contacting individual bushy cells at the end of the process (Jackson and Parks, 1982; Lu and Trussell, 2007). This process is fundamental to achieve tonotopic sound transmission.

VGLUT1, labeling endbulbs, and parvalbumin, labeling AVCN bushy cell somata, antibody immunostaining revealed endbulb synapse morphological abnormalities in *Atoh1*^{Hox2cKO} mutants, as compared to control adult mice (Figure 5A). In order to carry out a 3D-reconstruction at cellular resolution of single axonal synaptic input to individual AVCN bushy cells, we carried out serial block face-scanning

electron microscopy. In control bushy cells, a single axonal input generated a large volume calyceal terminal surrounding most of the soma surface with additional smaller endings (2-6) from distinct axon terminals (Figures 5B-C). In contrast, *Atoh1*^{Hox2cKO} mutant bushy cells were targeted by up to 12-15 distinct axon terminals bearing small volume endings (Figures 5B-C).

Thus, the observed overlapping and broadening of c-fos^{+} responsive bands induced upon tone stimulation could be explained by multiple inputs relaying distinct frequencies and converging on individual bushy cells (Figures 3 and 4; model, Figure 5D), resulting in degradation of tonotopic tuning of mutant AVCN bushy cells and in failure to discriminate two close pure tone frequencies.

Hox2 Factors Regulate Expression of Genes Involved in Target-Derived Signaling, Adhesion, Synaptogenesis, and Synaptic Transmission

Presynaptic afferent refinement resulting in precise frequency tuning requires pruning of axon branches, synapse strengthening and elimination but also interactions with post-synaptic molecules and cell membrane bound receptors in the target nuclei (Brenowitz and Trussell, 2001; Kandler et al., 2009; Jackson and Parks, 1982; Leake et al., 2002; Ryugo et al., 2006; Yu and Goodrich, 2014).

To gain insights into the molecular programs regulated by *Hox2* transcription factors which might influence early steps of pre-synaptic maturation, we carried out transcriptome analysis in newborns by RNA sequencing (RNA-Seq). We dissected out the AVCN and isolated neurons by Fluorescence Activated Cell Sorting (FACS) from control (*Atoh1*$^{Rosa::tdTomato}$; n = 4 replicates, 3-4 AVCN per replicate) and mutant (*Atoh1*$^{Hoxa2hetHoxb2cKO;Rosa::tdTomato}$; n = 4 replicates, 3-4 AVCN per replicate) newborn

animals recovered at E18.5 by cesarian sections. We identified 400 differentially expressed genes (FC>1.5; p-value: <0.01) (Figures 6A-B; Table S1). Amongst them, Gene Ontology (GO) analysis (Table S2) identified molecules involved in calcium signaling pathway regulating synaptogenesis and synaptic transmission, cell adhesion molecules, and target-derived cues involved in axon pruning and synapse development (Figures 6C).

For example, genes up-regulated in mutant AVCN neurons included the voltage sensitive Ca^{2+} channels *Cacna1g (Cav3.1)* and *Cacna1i* (*Cav3.3*), calcium homeostasis regulating *Mctp1*, calcium modulator *Pcp4*, Ca^{2+}/calmodulin dependent protein kinase *Camk2b* (whereas *Camk4* was down-regulated), calcium binding protein of the calmodulin family *Caln1*, *Tspan7* involved in morphological and functional maturation of glutamatergic synapses, synaptic adhesion-like molecule *Lrfn5* binding postsynaptic density 95 (PSD95) and regulating synapse formation, core protein of the glutamatergic receptor postsynaptic scaffold complex *Dlgap1*, neuron-specific tyrosine phosphatase *Ptpn5* regulating glutamatergic synaptic plasticity, and the NMDA receptor subunit *Grin1*. Several cell adhesion molecules, potentially involved in cell-cell recognition during synapse formation, were also up-regulated including *Ajap1*, *Igsf5*, *Svep1*, members of the cadherin superfamily such as *Cdhr1*, *Cdh4*, *Cdh7*, *Cdh13*, and the protocadherin *Pcdh11x*.

Target-derived cues and retrograde signaling by secreted molecules may also be involved in pre-synaptic axon branch pruning, synapse strengthening, and elimination (Bagri et al., 2003; Kalinovsky et al., 2011; Umemori et al., 2004; Xiao et al., 2013). We detected an up-regulation of *Bmp2*, *Bmp6*, and *Fgf10* and concomitant down-regulation of the repulsive molecules *Sema6a* and *Slit2*, whereas we did not detect significant expression changes of ephrins and/or Eph receptors, involved in axon

guidance during early auditory circuit development (Cramer and Gabriele, 2014). Lastly, a panel of differentially expressed genes from the RNA-Seq analysis, namely *Caln1, Ptpn5*, *Dlgap1*, *Cdhr1*, *Cdh7*, *Camk4,* and *Sema6a*, was further validated by quantitative reverse transcription PCR (RT-qPCR) of RNA from dissected and FACS isolated AVCN neurons from *Atoh1*$^{Rosa::tdTomato}$ control, *Atoh1*$^{Hoxa2hetHoxb2cKO;Rosa::tdTomato}$, as well as *Atoh1*$^{Hox2cKO;Rosa::tdTomato}$ double homozygous mutant newborns (Figure 6D-E).

Altogether, the transcriptional changes detected in AVCN glutamatergic neurons deficient for *Hox2* function provide a post-synaptic molecular correlate to understand the multiple innervation of AVCN bushy cells, impairment of endbulb synapse development, and lack of tonotopic precision of AVCN neuron response (Figures 3, 4 and 5).

DISCUSSION

This study further expands the repertoire of emerging roles of *Hox* genes in orchestrating topographic circuit assembly (reviewed in Philippidou and Dasen, 2013). *Hox* genes are key regulators of neuronal anteroposterior identity, but the link between *Hox*-mediated neuronal diversification, assembly of regionally specialized circuits, and refinement of topographic precision of connectivity is still poorly understood. We have recently shown that in the principal trigeminal nucleus of the somatosensory brainstem *Hoxa2* is sufficient to organize topographic input-output connectivity of barrelette neurons underlying whisker map formation (Bechara et al., 2015). Here, we found that *Hox2* genes are required in *Atoh1*-derived glutamatergic bushy cells of the AVCN, which receive cochleotopic input from SG afferents. In the absence of *Hox2* function, broad input topography and sound transmission is largely preserved as supported by the

c-fos activation patterns in AVCN and behavioral functional tests. However, the fine-scale tonotopic refinement and maturation of the brainstem auditory circuit is impaired resulting in defective frequency tuning in the mutant animals. These findings point to an important role of *Hox2* genes during the development of highly topographic brainstem sensory circuits.

We did not attempt in this study to investigate whether *Hoxa2* or *Hoxb2* carry out distinct roles or whether they are fully or only partially redundant during maturation. Nonetheless, molecular, anatomical, and functional analyses indicated that collectively Hox2 transcription factors orchestrate the refinement of pre-synaptic input tonotopic precision in the post-synaptic neuron through transcriptional regulation of target-derived signaling molecules, activity dependent calcium signaling molecules, neurotransmitter receptor expression, axon pruning, and endbulb synapse maturation. Tonotopic map refinement of brainstem circuits has been shown to be dependent on prehearing activity bursts generated by cochlear hair cells and propagated by SG neurons to brainstem auditory nuclei (Clause et al., 2014). It will be interesting to investigate whether late stage *Hox* gene expression might be involved in activity-dependent transcriptional regulation. Altogether, these results provide novel insights into the multifaceted involvement of *Hox* transcription factors in central nervous system and circuit development. They establish a novel non-cell autonomous role for Hox factors in the post-synaptic cochlear neuron regulating pre-synaptic Endbulb of Held development and the precision of sound transmission in the first central station of the auditory circuit, with their absence resulting in central auditory discrimination deficits.

Lastly, these findings may also advance our understanding of the genetic basis of children central auditory processing disorders (CAPD) (Bellis and Ferre, 1999). CAPD are detected in humans, especially children, where the peripheral hearing is

intact but the processing of auditory information in the central nervous system is impaired, similar to the phenotype described here in mice carrying mutations of *Hox2* genes in brainstem cochlear nuclei. The difficulty in decoding and processing auditory information in children suffering from CAPD often results in deterioration in social behavior due to defects of expressive and receptive communication. For example, children with dyslexia, autism and attention deficit hyperactivity disorder are often diagnosed with CAPD. The current work might provide a suitable genetic model to improve our understanding of CAPD molecular, cellular, and behavioral etiology.

EXPERIMENTAL PROCEDURES

Animals All animal procedures were performed in accordance with institutional guidelines and were approved by the Veterinary Department of the Canton of Basel-Stadt.

Generation of *Atoh1^{Cre}* Line The *Atoh1^{Cre}* mouse line was generated by subcloning the 1.7 kb *Atoh1* (Helms et al., 2000; Machold and Fishell, 2005) enhancer in the pKS-ß-globin-Cre-SV40pA plasmid. The *Atoh1* enhancer was PCR amplified from genomic DNA using the primers: 5'AGT TGT GCC TGT CTA AGG TC 3' and 5'ATC TAC TAG TGC TCT GGC TTC TGT AAA CTC 3'. The PCR band was purified and inserted 5' to the ß-globin promoter using restriction sites *SacII* and *SpeI*. The resulting construct consisted of the *Atoh1* enhancer, ß-globin minimal promoter, and *Cre recombinase* encoding sequence. The construct was linearized, purified and microinjected into the pronuclei of mouse zygotes. Founders were identified by PCR using the following primers: 5'AGT GGA GAA TGG GTT AAA TCC 3' and 5'ATC AGT GCG TTC GAA CGC TA 3'.

Histological Analysis, Immunostaining, and *In Situ* Hybridization Prenatal or

postnatal brains, dissected when necessary, were fixed in 4% PFA diluted in phosphate buffer (PBS 1x) from 30 minutes at room temperature to overnight at 4° C. For cryostat sections, tissues were cryoprotected in 20% sucrose (Fluka) / PBS1x and embedded in gelatine 7.5% (Sigma) / 10% sucrose / PBS1x before being frozen at -80°C. Cryostat (Microm HM560) sections (20 μm and 30 μm) were cut in coronal and sagittal planes. For immunohistochemistry, cryoprotected tissues were mounted with normal water and frozen to -50 °C and cut at 40 um thickness. Vibratome (Leica VT10005) sections (60 um) were prepared from postnatal brains after embedding in 4% agarose (Promega)/0.1 M phosphate buffer (pH 7.4). Immunohistochemistry was performed as described using the antibodies: ZsGreen (rabbit, Clontech, Cat. No. 632474), (Di Meglio et al., 2013) BARHL1 (rabbit, Sigma, HPA004809), MafB P-20: sc-10022 (goat, Santa Cruz Biotechnology, Inc), Parvalbumin 28 (rabbit, Swant), Pax6 (Cat. No. AB2237, Millipore), Streptavidin Alexa-488 conjugates (Life Technologies, Cat. No. S-11223), GFP (rabbit, Life Technologies, A6455), GFP (chicken, Invitrogen, A10262), RFP (rabbit, Rockland, Cat. No. 600-401-379), c-Fos Ab-5, 4-17 (rabbit, Calbiochem, Cat. No. PC38), VGLUT1 (mouse, Chemicon, Cat. No. MAB5502). Standard *in situ* hybridization was performed as described[16]. Fluorescent *in situ* hybridizations were performed as described in the Perkin Elmer, TSA Plus Fluorescence kit manual. The following probes(Di Bonito et al., 2013; Di Meglio et al., 2013) were used: *Barhl1, Hoxa2, Hoxb2, Rig1, Math5*, *MafB*. Other probes were synthesized by amplifying the region of interest by PCR from template cDNA prepared from whole RNA extacted from E14.5 brain and by cloning the amplicons into pCRII-TOPO vector using a TOPO TA cloning kit (Life Technologies). Namely, *Vglut1* (Forward: CCT GTT CTG GTT GCT TGT CTC; Reverse: TCG TCC TCC ATT TCA CTT TC, XhoI, Sp6 promoter), *Vglut2* (Forward: CCA AAT CTT ACG GTG CTA CCTC; Reverse: TAG CCA TCT

TTC CTG TTC CACT, XhoI, Sp6 promoter), *c-fos* (Forward: AGA ATC CGA AGG GAA CGG; Reverse: GGA GGC CAG ATG TGG ATG, XbaI, Sp6 promoter). For double *in situ* hybridization and immunohistochemistry stainings, *in situ* hybridization was carried out prior to immunohistochemistry. X-galactosidase staining on whole embryos, whole brains or cryostat sections was performed as described (Di Meglio et al., 2013).

RT-PCR Analysis of *Hox2* Gene Expression at Postnatal Stages To average variability between individuals, gene expression analysis was performed on two sets (duplicates) of wild type pups or animals at P0, P2, P6, P11, P16, P21, P30 and P60. In brief, AVCN and somatosensory cortex (negative control) were hand-dissected from brains at different stages under a microscope (Leica, MZ7s) and used for total RNA extraction using Arcturus Pico Pure RNA Isolation kit (Applied Biosystems). RNA extracted from E10.5 branchial arch was used as a positive control. cDNA was synthesized using Superscript III Reverse Transcriptase (Life Technologies) kit. RT-PCR with primers for *Hox2* genes and β-tubulin genes was performed. Primers are: *Hoxa2* (Fwd: GTGTTGGTGTACGCGGTT; Rev: GATGAAGGAGAAGAAGGCGG); *Hoxb2* (Fwd1: AGAAACCCAGCCAATCCG; Rev: GCAGTTGCGTGTTGGTGT).

Analysis of *Hox2* Gene Deletion Mosaicism by Quantitative PCR Mosaicism analysis was performed on E16.5 $Atoh1^{Hox2cKO;Rosa::tdTomato}$ mutant fetuses. In brief, the fluorescent cochlear nuclei from each mutant were hand-dissected, pooled, and collected in individual tubes and incubated in DMEM (Gibco)/0.1% trypsin (Gibco) for 8 min at 37 °C. Tissue was then transferred to and rinsed four times in DMEM / 10% FBS before mechanical dissociation. Fluorescent cells were collected by fluorescence activated cell sorting (FACSCalibur, Becton Dickson). The sorted cells were digested with proteinase K and the genomic DNA was extracted with phenol / chloroform /

isoamyl alcohol, precipitated with ethanol / sodium acetate and then resuspended in water. To serve as reference values, we also extracted genomic DNA from E12.5 littermate control (carrying 2 wild type alleles) and *Hoxa2* (Pasqualetti et al., 2002) or *Hoxb2* (Di Bonito et al., 2013) heterozygous mutant (carrying only one *Hoxa2* or *Hoxb2* wild type allele, respectively) embryos. Quantitative PCR analysis was carried out on each $Atoh1^{Hox2cKO;Rosa::tdTomato}$ double homozygous and *Hoxa2* and *Hoxb2* single heterozygous mutant and control samples using the StepOne Real Time PCR System (Applied Biosystems) and primers located within the floxed alleles for *Hoxa2* and *Hoxb2* (target genes), and in *Hoxa5* (reference gene) for the normalization (see table for the sequence of the primers). The mosaicism was calculated using the $2^{-\Delta\Delta Ct}$ calculation (Tesson et al.,) where $\Delta\Delta Ct=(Ct_{\text{gene target}} - Ct_{\text{reference gene}})_{\text{unknown}} - (Ct_{\text{gene target}} - Ct_{\text{reference gene}})_{\text{known}}$ and "known" refers to heterozygous controls. The final values are expressed in percentage of remaining gene = $(2^{-\Delta\Delta Ct})$ x 50. Primers for qPCR are: *Hoxa2* (Fwd: TACGAATTTGAGCGAGAGATTGG; Rev: AAGCGTCGAGGTCTTGATTG); *Hoxb2* (Fwd: CCTACACCAACACGCAACTGCT; Rev: CTTGTGTTTCATGCGTCGGTTC); *Hoxa5* (Fwd: AAAAAGAAATCGGGCGCCCCA; Rev: GAAACGCACTGAAGCACTAC).

Neurovue Labeling from Cochlea to AVCN and Quantification The heads of E18.5 fetuses were fixed in 4% PFA diluted in phosphate buffer (PBS 1x), overnight at 4° C. After removing the heads from the PFA, the lower jaw, tongue and attached tissue on the ventral side of the head were removed to reveal the bony labyrinth. Dissecting through the bony labyrinth, the cochlea was revealed. Small incisions were made into the cochlea with microscissors (F.S.T. 15000-03) to insert tiny strips of Neurovue (Red FS 1002, Maroon FS-1001, Molecular Targeting Technologies, Inc). Neurovue strips coated with distinct fluorescent dyes were inserted into different turns of the cochlea.

The heads were then incubated in 4% PFA in PBS 1x at 37 ° C, for 10 days. The brains were then dissected out and embedded in 4% agarose (Promega)/0.1 M phosphate buffer (pH 7.4) for sectioning with vibratome (60 um). Sections anterior to the auditory nerve entry point were identified as AVCN, collected (2-3 sections), and briefly counterstained with DAPI (1:10,000 DAPI in PBS1x) before being imaged with Leica Z16 Apo macroscope using Image Access software. The sections were then stained with an anti-MafB antibody to label the AVCN. The cochlea was dissected out and counterstained in DAPI, before being imaged. For image quantification, Image Access software was used to calculate areas of the respective labeled regions in the images. S_b: AVCN area targeted by afferents labeled from basal turn; S_m: AVCN area targeted by afferents labeled from middle turn labeling; S_{AVCN}: total AVCN area stained by anti-MafB; θ_b: angle of spread of Neurovue dye in basal turn; θ_m: angle of spread of Neurovue dye in middle turn. For data plotting, the ratios for basal and middle turn were calculated as $(S_b/S_{AVCN}*100)/\theta_b$ and $(S_m/S_{AVCN}*100)/\theta_m$, respectively.

Biotinylated Dextran Amine (BDA) Axonal Tracing The BDA labeling from the AVCN was performed as described(Di Bonito et al., 2013) in P7 control and mutant dissected brains. Following incubation for 6 hours at room temperature, the brains were fixed as described before and vibratome sections at 60 um were made the following day. The sections were stained with Streptavidin Alexa-488 (Invitrogen) and immunohistochemistry was carried out with anti-VGLUT1. The sections were counterstained in DAPI and imaged with confocal microscope LSM 700 (Axio Imager Z2, upright microscope + LSM 700 scanning head; Software: ZEN Black 2012).

SBF-SEM and 3D Reconstructions Adult mice were fixed by cardiac perfusion with paraformaldehyde and glutaraldehyde, and brain areas including the AVCN were

sectioned with a vibratome (Leica). Sections were stained according to NCMIR protocol (http://ncmir.ucsd.edu/sbfsem-protocol.pdf). The slices were further rinsed in cacodylate buffer 0.1M pH 7.4 and post-fixed with 1.5% ferrocyanide in 2% osmium for one hour. After extensive rinsing in ddH2O, sections were stained in 1% thiocarbohydrazide for 20 minutes at 60 degree followed by rinsing in ddH2O. A second osmium post-fixation in 2% osmium was done for 30 minutes. Sections were then stained in uranyl acetate 1% overnight. Next day, sections are stained for 20 minutes in Walton's lead aspartate before dehydration and embedding in epoxy resin. SBFSEM was done as described (Denk and Horstmann, 2004) using the 3View microtome (GATAN) mounted on a QUANTA 200 VP-FEG (FEI). The AVCN was identified on vibratome sections, cut out of the section and mounted on aluminium stubs for the sample holder of the 3View. The blocks were then trimmed on pyramidal shape and sputter-coated with gold. Once placed on the microtome, the surface of the block was imaged (4 kV beam, spot size 3, low vacuum mode with 0.22 Torr of water pressure in the chamber). Two fields of view with an overlap of 15% were determined in the center of the AVCN. Each field of view represents a surface of 51× 51 μm (8,192 × 8,192 pixels, 6nm pixel size). After imaging of the block face using the backscattered electron detector of 3View (GATAN), a diamond knife removed 100 nm from the surface of the block, and the new surface was imaged using the same parameters. This cycle was repeated 1000 times (150 h of image acquisition per block). Images were then preprocessed to equalize the contrast and to be registered (TrakEM2, FIJI). Further 3D reconstruction was done using TrakEM2, FIJI. The volumes of the presynaptic axonal terminals were measured using the FIJI software.

RNA Sequencing Analysis and Quantitative Reverse Transcription PCR To average variability between individuals, RNA-Seq expression analysis was performed

on four sets of control and mutant embryos, each consisting of pooled hand-dissected fluorescent cochlear nuclei from 3-4 *Atoh1*$^{ROSA::tdTomato}$ or *Atoh1*$^{Hoxa2hetHoxb2cKO;Rosa::tdTomato}$ newborns, respectively, recovered by cesarian sections at E18.5 from different litters. In brief, hand-dissected fluorescent cochlear nuclei were incubated in DMEM (Gibco)/0.1% trypsin (Gibco) for 8 min at 37 °C. Tissue was then transferred to and rinsed four times in DMEM / 10% FBS before mechanical dissociation. Fluorescent cells were collected by fluorescence activated cell sorting (FACSCalibur, Becton Dickson). RNA was extracted using the PicoPure RNA Isolation Kit (Applied Biosystems, Calif., USA) and retro-transcribed. Libraries were prepared using the Total RNA Sequencing TotalScript Kit (Epicenter) and sequencing was performed using Hi-Seq 2500 Illumina solid sequencer. Data analysis was performed using the Bioconductor QuasR Package (release 3.0). Gene Ontology analysis was performed using the GO Enrichment Analysis tool powered by PANTHER (http://geneontology.org/page/go-enrichment-analysis). GEO Accession number GSE64092. For validation of gene expression changes between control and mutants, we performed quantitative RT-PCR. Fluorescent cochlear nuclei were collected from E18.5 *Atoh1*$^{ROSA::tdTomato}$, *Atoh1*$^{Hoxa2hetHoxb2cKO;Rosa::tdTomato}$ and *Atoh1*$^{HoxPG2cKO;Rosa::tdTomato}$ by dissection and then cells were isolated by FACS. RNA was extracted using the Norgen RNA Purification Kit (Norgen Biotek Corp., Ontario, Canada) and the cDNA was prepared using Superscript III reverse transcriptase system (Life Technologies). QPCR was carried out with StepOne Real Time PCR System and TaqMan Gene Expression Assays (Applied Biosystems): *Caln1*(Mm01201254_m1), *Ptpn5* (Mm00479063_m1), *Cdh7* (Mm00556135_m1), *Cdhr1* (Mm00499982_m1), *Dlgap1* (Mm00510688_m1), *Camk4* (Mm01135329_m1), *Sema6a* (Mm00444441_m1) and *Gapdh* (Mm99999915_g1). Gapdh was used for the normalization and the relative gene expression was calculated

using the $2^{-\Delta\Delta Ct}$ calculation where $\Delta\Delta Ct=(Ct_{gene\ target} - Ct_{Gapdh})_{Mutant}$ - $(Ct_{gene\ target} - Ct_{Gapdh})_{Control}$. The fold change is expressed in percentage = $(2^{-\Delta\Delta Ct})$ x 100.

Auditory Stimulation and c-fos Response Analysis Auditory stimulation experiments were performed as describe (Miko et al., 2007). Awake, freely moving 2-3 month old mice were placed within a round glass enclosure on a platform in a sound insulated chamber. Speakers (Coulburn speakers # H12-01R) delivering auditory tones were placed directly overhead the platform. Tones were delivered through a DENON CD player DN-D4500 with Sony integrated stereo amplifier TA–FE370. Calibration was performed using a microphone (Bruel and Kjaer, Norcross, GA) in the position of the animal. Mice were kept in silence for 60 minutes, followed by free field tone pips at 75 dB SPL for 90 minutes. For some animals, sound was delivered as 8 kHz tone pips, of 50 msec duration, with a 4 msec rise-fall time and 40 msec gap, played at 11.1 Hz frequency, for 90 minutes. For another group of animals, sound was delivered as 15-kHz tone pips, of 400 msec duration, with a 5 msec rise-fall time and 300 msec gap, played at 1.43 Hz frequency, for 90 minutes. For dual presentation of 8 and 15 kHz tones, alternating 8 kHz (400ms, 1.43 Hz) and 15 kHz (400ms, 1.43 Hz) were presented for 90 minutes. After 90 minutes, the animals were transcardially perfused with 4% PFA in PBS1x and the brains collected. The brains were processed for immunohistochemistry as described before. Cryostat sections of 40um thickness were prepared and immunohistochemistry with anti c-Fos Ab-5, 4-17 (rabbit, Calbiochem, Cat. No. PC38) was performed on free-floating sections. It labeled activated cells in AVCN and DCN. No other c-Fos antibody was found to label the activated cells in the AVCN, though activated cells in the DCN could be detected with other anti-c-Fos antibodies. As the production of the anti c-Fos antibody Ab-5, 4-17 (rabbit, Calbiochem, Cat. No. PC38) was discontinued; further experiments were carried out by

in situ hybridization with *c-fos* antisense mRNA probe that resulted in similar results as the c-fos antibody stainings (Figure 3C). Quantification of the c-Fos labeled cells was done using Cell Counter plugin in ImageJ software (http://fiji.sc/wiki/index.php/Fiji). For calculation, the number of cells or the area covered by the labeled cells was normalized over the size of the AVCN for each section and the ratio was used to plot the graphs using Graphpad prism software (version 6). The area size of the AVCN on each section was measured using ImageJ software. The ratio between c-Fos labeled cells and the area of AVCN was fed into a R-script for automated quantification. Samples were randomized before quantification to enable quantification blind to genotype.

Auditory Fear Conditioning Experiments We carried out a discriminative auditory fear conditioning paradigm (Ciocchi et al., 2010). Before behavioural experiments, control and mutant 2–3 month old mice were individually housed in a 12h light/dark cycle. Behavioural experiments were performed during the light cycle. Fear conditioning experiments were performed as described (Ciocchi et al., 2010). Fear conditioning and fear test took place in two different contexts (context A and B). The conditioning and test boxes and the floor were cleaned with 70% ethanol or 1% acetic acid before and after each session, respectively. Freezing behavior was scored blind to genotype, by using an automatic infrared beam detection system placed on the bottom of the experimental chambers (Coulbourn Instruments). Mice were considered to be freezing if no movement was detected for 2s and the measure was expressed as a percentage of time spent freezing. On day 1, mice were submitted to a habituation session in context B, in which they received 4 presentations of the CS^+ and the CS^- (each CS duration of 30s). Discriminative fear conditioning was performed on day 1 in

context A by pairing the CS^+ with a foot shock (1s foot shock, 0.6 mA). The onset of the foot shock coincided with the offset of the CS^+. The CS^- was presented after each CS^+/foot shock association but was never reinforced (inter-trial interval: 20–180 s). Each animal was trained to 10 pairings of CS^+/foot shock and CS^-. Both 8 kHz and 15 kHz were used as CS^+ or CS^- to avoid any bias due to the tone used, and the CS+ was counterbalanced across animals. On day 2, conditioned mice were submitted to fear retrieval in context B. Following a 3 minute baseline period in which no tones were played, mice received four presentations of the CS^- and the CS^+ (each 30s long, variable inter-trial interval), respectively and the freezing responses were compared. To compare the discriminative fear response, the ratio of freezing response in CS^+ to freezing response in CS^- was calculated.

Quantification of Behavior All behavioral sessions were recorded to video using Cineplex software (Plexon) and mice were tracked using contour tracking. Behavior was scored from the video recording by an observer blind to the condition, using the assistance of a frame-by-frame analysis of pixel changes (Cineplex Editor, Plexon). By calibrating the known size of the chambers with the pixel dimensions of the camera to determine a calibration coefficient, speed (cm/s) was extracted using the animal center of gravity. To assess general mobility traits in control and mutant mice, we used the speed calibration to quantify the average speed and distance traveled during the 3 minute baseline period of the retrieval session.

Image Processing Fluorescent images were acquired with LSM700 (Laser Scanning Microscope; Axio Imager Z2, upright microscope + LSM 700 scanning head; Software: Zen Black 2012) unless mentioned otherwise. The chromogenic images of the *in situ* hybridization were obtained with a brightfield Microscope (Nikon E600 Eclipse).

Image analysis was performed using Fiji imaging analysis software (http://fiji.sc/wiki/index.php/Fiji).

Statistical Analysis Statistical analyses were done with Graphpad Prism 6 software. All results are expressed as the mean ± s.e.m. For statistical analyses, normality tests were done for all datasets. Nonpaired, two-tailed Student's *t* test and One-way ANOVA were performed for datasets that passed normality tests and were accepted at the $P < 0.05$ level. For datasets that did not pass the normality tests, the non-parametric Mann-Whitney and Kruskal-Wallis tests were performed, as mentioned.

AUTHOR CONTRIBUTIONS

KK carried out anatomical and molecular assays, auditory stimulation and fear conditioning tests and data analysis. YN started the project, carried out afferent tracing assays, as well as initial auditory stimulation and fear conditioning tests. ALo and TK carried out RNA-Seq and analysis. JF, JB, and SD set up fear conditioning experiments. SD generated and characterised transgenic lines and carried out mosaicism analysis. CG helped with data collection and supervised EM data analysis. RT created MatLab scripts. TDM carried out some in situ hybridisation experiments. ALu supervised fear conditioning tests and provided input to the manuscript draft. FMR conceived and supervised the project and wrote the manuscript based on a first draft by KK.

ACKNOWLEDGEMENTS

We thank Nathalie Vilain, Christian Müller, and Milica Markovic for technical assistance, Moritz Kirschmann for help with EM data collection, Hubertus Kohler for FACS experiments, Tim Roloff for help with RNA-Seq data. We also thank Claudius Kratochwil for discussions and Ralf Schneggenburger for comments on the manuscript.

This work was supported by grants from the Swiss National Science Foundation, ARSEP, and the Novartis Research Foundation.

REFERENCES

Alasti, F., Sadeghi, A., Sanati, M.H., Farhadi, M., Stollar, E., Somers, T., Van Camp, G. (2008) A Mutation in HOXA2 Is Responsible for Autosomal-Recessive Microtia in an Iranian Family. The American Journal of Human Genetics *82*, 982–991.

Bagri, A., Cheng, H.-J., Yaron, A., Pleasure, S.J., Tessier-Lavigne, M., (2003). Stereotyped pruning of long hippocampal axon branches triggered by retraction inducers of the semaphorin family. Cell *113*, 285–299.

Bechara, A., Laumonnerie C., Vilain N., Kratochwil C., Cankovic V., Maiorano N., Kirschmann M., Ducret S., Rijli, F.M. (2015) Hoxa2 selects barrelette neuron identity and connectivity in the mouse somatosensory brainstem. Cell Reports *13*, 783-797.

Bellis, T.J., Ferre, J.M., (1999). Multidimensional approach to the differential diagnosis of central auditory processing disorders in children. J Am Acad Audiol *10*, 319–328.

Brenowitz, S., Trussell, L.O., (2001). Maturation of synaptic transmission at end-bulb synapses of the cochlear nucleus. J. Neurosci. *21*, 9487–9498.

Ciocchi, S., Herry, C., Grenier, F., Wolff, S.B.E., Letzkus, J.J., Vlachos, I., Ehrlich, I., Sprengel, R., Deisseroth, K., Stadler, M.B., Müller, C., Lüthi, A., (2010). Encoding of conditioned fear in central amygdala inhibitory circuits. Nature *468*, 277–282.

Clause, A., Kim, G., Sonntag, M., Weisz, C.J.C., Vetter, D.E., Rűbsamen, R., Kandler, K., (2014). The Precise Temporal Pattern of Prehearing Spontaneous Activity Is

Necessary for Tonotopic Map Refinement. Neuron *82*, 822–835.

Cramer, K.S., Gabriele, M.L., (2014). Axon guidance in the auditory system: multiple functions of Eph receptors. Neuroscience *277*, 152–162. doi:10.1016/j.neuroscience.2014.06.068

Denk, W., Horstmann, H., (2004). Serial Block-Face Scanning Electron Microscopy to Reconstruct Three-Dimensional Tissue Nanostructure. PLoS Biol. *2*, e329.

Di Bonito, M., Narita, Y., Avallone, B., Sequino, L., Mancuso, M., Andolfi, G., Franzè, A.M., Puelles, L., Rijli, F.M., Studer, M., (2013). Assembly of the auditory circuitry by a Hox genetic network in the mouse brainstem. PLoS Genet *9*, e1003249.

Di Meglio, T., Kratochwil, C.F., Vilain, N., Loche, A., Vitobello, A., Yonehara, K., Hrycaj, S.M., Roska, B., Peters, A.H.F.M., Eichmann, A., Wellik, D., Ducret, S., Rijli, F.M. (2013). Ezh2 orchestrates topographic migration and connectivity of mouse precerebellar neurons. Science *339*, 204–207. doi:10.1126/science.1229326

Farago, A.F., Awatramani, R.B., Dymecki, S.M. (2006). Assembly of the Brainstem Cochlear Nuclear Complex Is Revealed by Intersectional and Subtractive Genetic Fate Maps. Neuron *50*, 205–218.

Fujiyama, T., Yamada, M., Terao, M., Terashima, T., Hioki, H., Inoue, Y.U., Inoue, T., Masuyama, N., Obata, K., Yanagawa, Y., Kawaguchi, Y., Nabeshima, Y.-I., Hoshino, M., (2009). Inhibitory and excitatory subtypes of cochlear nucleus neurons are defined by distinct bHLH transcription factors, Ptf1a and Atoh1. Development *136*, 2049–2058.

Gavalas, A., Davenne, M., Lumsden, A., Chambon, P., Rijli, F.M. (1997). Role of Hoxa-2 in axon pathfinding and rostral hindbrain patterning. Development *124*, 3693–3702.

Gendron-Maguire, M., Mallo, M., Zhang, M., Gridley, T. (1993). Hoxa-2 mutant mice exhibit homeotic transformation of skeletal elements derived from cranial neural crest. Cell *75*, 1317–1331.

Helms, A.W., Abney, A.L., Ben-Arie, N., Zoghbi, H.Y., Johnson, J.E. (2000). Autoregulation and multiple enhancers control Math1 expression in the developing nervous system. Development *127*, 1185–1196.

Jackson, H., Parks, T.N. (1982). Functional synapse elimination in the developing avian cochlear nucleus with simultaneous reduction in cochlear nerve axon branching. J. Neurosci. *2*, 1736–1743.

Kalinovsky, A., Boukhtouche, F., Blazeski, R., Bornmann, C., Suzuki, N., Mason, C.A., Scheiffele, P. (2011). Development of axon-target specificity of ponto-cerebellar afferents. PLoS Biol. *9*, e1001013.

Kandler, K., Clause, A., Noh, J. (2009). Tonotopic reorganization of developing auditory brainstem circuits. Nat Neurosci *12*, 711–717.

Kiecker, C., Lumsden, A. (2005). Compartments and their boundaries in vertebrate brain development. Nat Rev Neurosci *6*, 553–564.

Koundakjian, E.J., Appler, J.L., Goodrich, L.V. (2007). Auditory neurons make stereotyped wiring decisions before maturation of their targets. J. Neurosci. *27*, 14078–14088.

Leake, P.A., Snyder, R.L., Hradek, G.T. (2002). Postnatal refinement of auditory nerve projections to the cochlear nucleus in cats. J. Comp. Neurol. *448*, 6–27.

Limb, C.J., Ryugo, D.K., (2000). Development of Primary Axosomatic Endings in the Anteroventral Cochlear Nucleus of Mice. JARO *1*, 103–119.

Lu, T., Trussell, L.O. (2007). Development and elimination of endbulb synapses in the chick cochlear nucleus. J. Neurosci. *27*, 808–817.

Machold, R., Fishell, G. (2005). Math1 Is Expressed in Temporally Discrete Pools of Cerebellar Rhombic-Lip Neural Progenitors. Neuron *48*, 17–24.

Maricich, S.M., Xia, A., Mathes, E.L., Wang, V.Y., Oghalai, J.S., Fritzsch, B., Zoghbi, H.Y. (2009). Atoh1-lineal neurons are required for hearing and for the survival of neurons in the spiral ganglion and brainstem accessory auditory nuclei. J. Neurosci. *29*, 11123–11133.

Miko, I.J., Nakamura, P.A., Henkemeyer, M., Cramer, K.S. (2007). Auditory brainstem neural activation patterns are altered in EphA4- and ephrin-B2-deficient mice. J. Comp. Neurol. *505*, 669–681.

Minoux, M., Kratochwil, C.F., Ducret, S., Amin, S., Kitazawa, T., Kurihara, H., Bobola, N., Vilain, N., Rijli, F.M. (2013). Mouse Hoxa2 mutations provide a model for microtia and auricle duplication. Development *140*, 4386–4397.

Narita, Y., Rijli, F.M. (2009). Chapter 5 - Hox Genes in Neural Patterning and Circuit Formation in the Mouse Hindbrain, 1st ed, Current Topics in Developmental Biology, Current Topics in Developmental Biology. Elsevier Inc. doi:10.1016/S0070-2153(09)88005-8

Oury, F., Murakami, Y., Renaud, J.-S., Pasqualetti, M., Charnay, P., Ren, S.-Y., Rijli, F.M., (2006). Hoxa2- and rhombomere-dependent development of the mouse facial somatosensory map. Science *313*, 1408–1413.

Pasqualetti, M., Ren, S.-Y., Poulet, M., LeMeur, M., Dierich, A.E., Rijli, F.M. (2002). A Hoxa2 knockin allele that expresses EGFP upon conditional Cre-mediated recombination. genesis *32*, 109–111.

Philippidou, P., Dasen, J.S. (2013). Hox Genes: Choreographers in Neural Development, Architects of Circuit Organization. Neuron *80*, 12–34.

Ren, S.-Y., Pasqualetti, M., Dierich, A.E., Le Meur, M., Rijli, F.M. (2002). AHoxa2

mutant conditional allele generated by Flp- and Cre-mediated recombination. genesis *32*, 105–108.

Rijli, F.M., Mark, M., Lakkaraju, S., Dierich, A., Dollé, P., Chambon, P. (1993). A homeotic transformation is generated in the rostral branchial region of the head by disruption of Hoxa-2, which acts as a selector gene. Cell *75*, 1333–1349.

Ryugo, D.K., Montey, K.L., Wright, A.L., Bennett, M.L., Pongstaporn, T. (2006). Postnatal development of a large auditory nerve terminal: The endbulb of Held in cats. Hearing Research *216-217*, 100–115.

Saul, S.M., Brzezinski, J.A., Altschuler, R.A., Shore, S.E., Rudolph, D.D., Kabara, L.L., Halsey, K.E., Hufnagel, R.B., Zhou, J., Dolan, D.F., Glaser, T. (2008). Math5 expression and function in the central auditory system. Mol. Cell. Neurosci. *37*, 153–169.

Tesson, L., Rémy, S., Ménoret, S., Usal, C., Anegon, I. (2010) Analysis by quantitative PCR of zygosity in genetically modified organisms. Methods Mol Biol. *597*, 277-85.

Umemori, H., Linhoff, M.W., Ornitz, D.M., Sanes, J.R. (2004). FGF22 and its close relatives are presynaptic organizing molecules in the mammalian brain. Cell *118*, 257–270.

Wang, V.Y., Rose, M.F., Zoghbi, H.Y. (2005). Math1 Expression Redefines the Rhombic Lip Derivatives and Reveals Novel Lineages within the Brainstem and Cerebellum. Neuron *48*, 31–43.

Xiao, L., Michalski, N., Kronander, E., Gjoni, E., Genoud, C., Knott, G., Schneggenburger, R. (2013). BMP signaling specifies the development of a large and fast CNS synapse. Nature Neurosci. *16*, 856–864.

Yu, W.-M., Goodrich, L.V. (2014). Morphological and physiological development of

auditory synapses. Hearing Research *311*, 3–16.

FIGURE LEGENDS

Figure 1 Characterization of *Atoh1* Derived *Hox2* Expressing Cells in Anterior Ventral Cochlear Nucleus

(A) E18.5 $Atoh1^{ROSA::tdTomato}$ positive cells, detected by anti-RFP (red) immunohistochemistry, are $vGlut2^{+}$ (green) glutamatergic, as assessed by fluorescent in situ hybridization (FISH).

(B-D) *Hoxa2* expressing *Atoh1*-derived cells**,** as detected by anti-EGFP (green) in E18.5 $Atoh1^{Hoxa2::EGFP}$ animals, are $vGlut2^{+}$ glutamatergic (red) **(B)** and coexpress *Hoxb2* (red) **(C)** as assessed by FISH. **D,** anti-VGLUT1 (red) immunostaining labels developing endbulb of Held synapses (white arrows) onto P14 $Atoh1^{Hoxa2::EGFP}$ (green) cells, identifying *Atoh1*-derived *Hoxa2* expressing AVCN bushy cells.

(E) The size of AVCN is not affected in $Atoh1^{Hox2cKO}$ (n = 4), $Atoh1^{Hoxa2cKO}$ (n = 3), $Atoh1^{Hoxb2cKO}$ (n = 3), as compared to control (n = 7) animals (One-way ANOVA analysis, p-value = 0.2448). Values are mean ± S.E.M. Statistical analysis in Methods. AVCN, anterior ventral cochlear nucleus. Scale bar, 5 um.

Figure 2 Altered Precision of Tonotopic Input Targeting the $Atoh1^{Hox2cKO}$ Anterior Ventral Cochlear Nucleus

(A) Neurovue labeled basal (green) or apical (red) turn of E18.5 cochlea from control.

(B) The Neurovue labeled axon terminals of E18.5 SG neuron afferents innervating the cochlear basal (green) or apical (red) turns, target distinct areas along the tonotopic (dorsoventral) axis of AVCN, immunostained with anti-MafB (white).

(C) Comparison of tracing from basal turn [$(S_b/S_{AVCN}*100)/\ \theta_b$] in E18.5 control (n = 5), *Atoh1*^{Hox2cKO} (n = 5), *Atoh1*^{Hoxa2cKO} (n = 5), and *Atoh1*^{Hoxb2cKO} (n = 3) fetuses. Kruskal-Wallis test shows significant differences amongst the samples (P< 0.0001). Multiple comparison shows significant difference between control and *Atoh1*^{Hox2cKO} but non-significant differences between control and *Atoh1*^{Hoxa2cKO} or *Atoh1*^{Hoxb2cKO}.

(D) Comparison of tracing from middle turn (grey bars) [$(S_m/S_{AVCN}*100)/\ \theta_m$] in E18.5 control (n = 5), *Atoh1*^{Hox2cKO} (n = 5), *Atoh1*^{Hoxa2cKO} (n = 5), and *Atoh1*^{Hoxb2cKO} (n = 3) fetuses. Kruskal-Wallis test shows significant differences amongst the samples (P<0.0001). Multiple comparison shows significant difference between control and *Atoh1*^{Hox2cKO} but non-significant differences between control and *Atoh1*^{Hoxa2cKO} or *Atoh1*^{Hoxb2cKO}.

Figure 3 Altered Isofrequency Bands in Anterior Ventral Cochlear Nucleus and Impaired Tone Discrimination in *Hox2* Mutants

(A-B) Activated neurons in adult control and *Atoh1*^{Hox2cKO} mutant AVCN labeled by anti-c-fos antibody staining (in white) in response to 15 kHz **(A)** or 8 kHz **(B)** pure tone stimulation.

(C) *c-fos* activated neurons detected by *in situ* hybridization in response to 15 kHz stimulation in control and *Atoh1*^{Hox2cKO} mutant AVCN.

(D) Anti-c-fos labeled AVCN activated neurons (white) in response to simultaneous 15 and 8 kHz pure tone stimulation. In controls, a separation area between the two activated isofrequency bands is readily detected (white doublehead arrow), whereas no obvious band separation is observed in *Atoh1*^{Hox2cKO} mutants.

(E-F) Quantification of AVCN activated areas normalized to the total AVCN size in response to 15 kHz (**E**) (control (n = 5), *Atoh1*^{Hox2cKO} (n = 3), p value= 0.0002, Mann-Whitney test) or 8 kHz (**F**) (control (n = 3), *Atoh1*^{Hox2cKO} (n = 4), p value= 0.0194, Mann-Whitney test) stimulations.

(G) Quantification of the area of band separation normalized to total AVCN area in control (n = 4) and *Atoh1*^{Hox2cKO} (n = 5) mutant animals, p value= 0.0004, Mann-Whitney test.

Figure 4 *Atoh1*^{Hox2cKO} Mutant Mice Fail to Discriminate Between Close Pure Tone Frequencies in Discriminative Auditory Fear Conditioning Setup

(A) Schematic for the fear conditioning setup. Adult control or *Hox2* mutant mice were subjected to discriminative fear conditioning behavioral test. During the training (acquisition) phase, the animals were subjected to a pure tone (CS+) at the end of which a foot-shock was administered; after a period of silence another pure tone (CS-) was played but not coupled to any foot-shock. Training consisted of 10 pairings of CS+ and CS-.

(B) In the recall test, four sets of CS- were played, followed by four sets of CS+. Freezing response was compared with response to no sound (baseline).

(C) *Atoh1*^{Hox2cKO} mutants show impaired discriminative (CS+/CS- freezing ratio) fear response; control (n = 30) and *Atoh1*^{Hox2cKO} (n = 28) mutants, p value = 0.0112, Mann-Whitney test. AVCN, anterior ventral cochlear nucleus. Scale bar, 50 um.

Figure 5 Multiple Innervation of Bushy Cells and Altered Endbulb of Held Synapse Formation in *Atoh1*^{Hox2cKO} Mutant Anterior Ventral Cochlear Nucleus

(A) Anti-VGLUT1 (green) labels endbulb of Held synapses whereas anti-Parvalbumin (red) labels the bushy cell soma in adult control and *Atoh1*^{Hox2cKO} mutant AVCN.

(B) 3D reconstruction of AVCN principal neurons using serial block face scanning electron microscopy; in control bushy cells (n = 3 cells from n = 2 control animals), the cell body (blue) is surrounded by one large volume endbulb terminal (yellow) and 2-6 additional small volume terminals; in *Atoh1*^{Hox2cKO} mutant animals (n = 4 cells from n = 3 mutants), the cell body is contacted by multiple, up to 12-15, small volume terminals (color coded). One control and two (*Atoh1*^{Hox2cKO} -1 and *Atoh1*^{Hox2cKO} -3) mutant representative cell examples are shown.

(C) Quantification of the volumes of each axonal terminal forming synapses on control or *Atoh1*^{Hox2cKO} single AVCN bushy cells.

(D) Model of tonotopic phenotype in *Hox2* mutants. In control mice, SG afferents relaying distinct frequencies target individual AVCN cells within their corresponding isofrequency band. In conditional *Hox2* mutants, principal sensory cells in AVCN receive multiple frequency inputs. AVCN, anterior ventral cochlear nucleus. SG, spiral ganglion. Scale bar, 2 um.

Figure 6 Transcriptome Analysis of Ventral Cochlear Neurons in Control and *Hox2* Mutant Newborns.

(A) Volcano plot of differentially expressed transcripts (Fold change:>1.5; p-value:<0.01).

(B) Heat map showing hierarchical clustering of downregulated (in red) and upregulated (in green) genes in *Atoh1*$^{Rosa::tdTomato}$ and *Atoh1*$^{Hoxa2hetHoxb2cKO;Rosa::tdTomato}$ mutant FAC-sorted cochlear neurons.

(C) Gene Ontology (GO) analysis of the differentially expressed genes. Clustering of genes was based on enrichment for biological processes, molecular function, and cellular compartment for upregulated (in purple) and downregulated (in blue) genes.

(D) Validation by quantitative PCR of relative differential expression of selected genes, as indicated, in control *Atoh1*$^{Rosa::tdTomato}$, *Atoh1*$^{Hoxa2hetHoxb2cKO;Rosa::tdTomato}$, and *Atoh1*$^{Hox2cKO;Rosa::tdTomato}$ cochlear neurons.

FIGURE 1

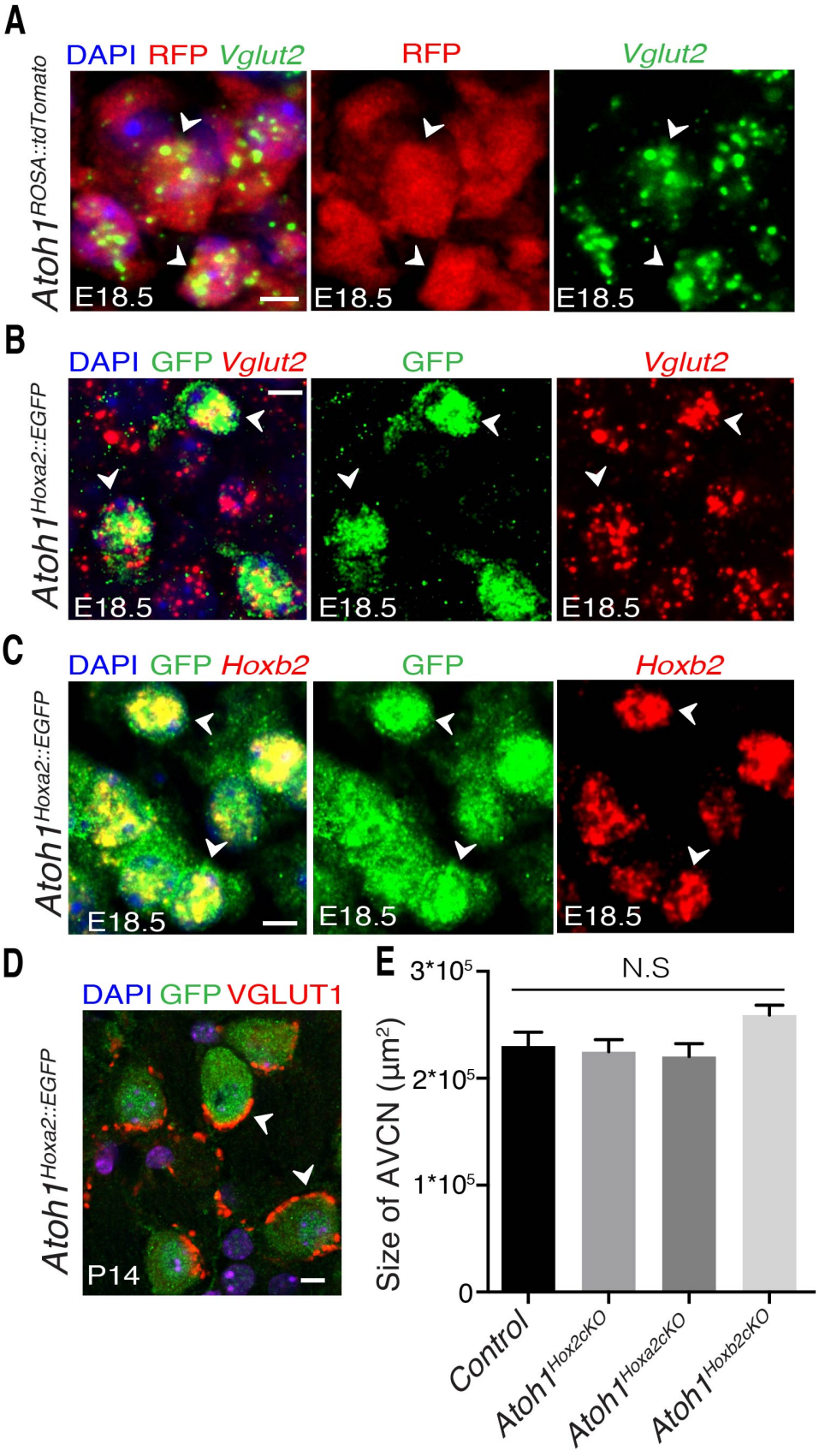
A
Atoh1ROSA::tdTomato
DAPI RFP Vglut2
RFP
Vglut2
E18.5
B
Atoh1Hoxa2::EGFP
DAPI GFP Vglut2
GFP
Vglut2
E18.5
C
Atoh1Hoxa2::EGFP
DAPI GFP Hoxb2
GFP
Hoxb2
E18.5
D
Atoh1Hoxa2::EGFP
DAPI GFP VGLUT1
P14
E
N.S
Size of AVCN (µm2)
3*10^5
2*10^5
1*10^5
0
Control
Atoh1Hox2cKO
Atoh1Hoxa2cKO
Atoh1Hoxb2cKO

FIGURE 2

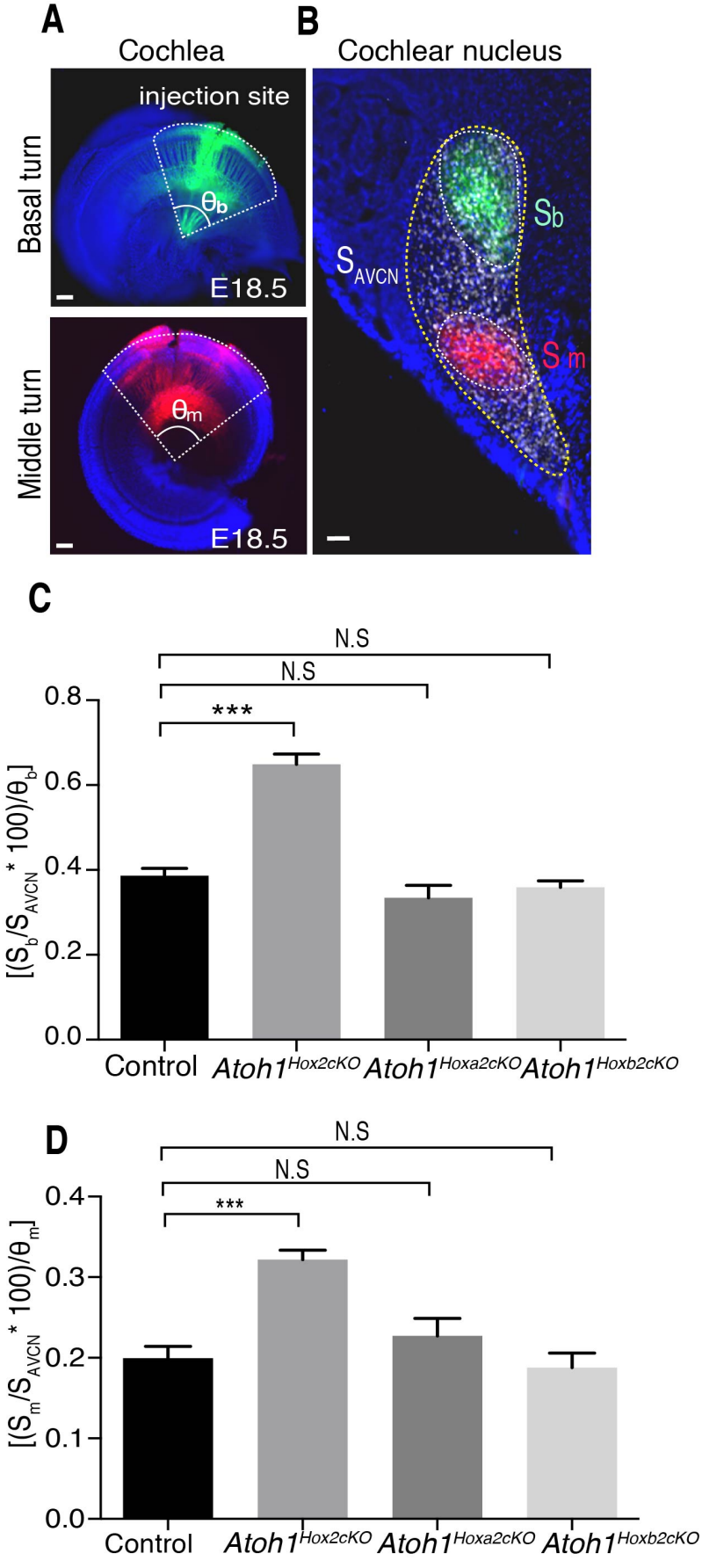
A
Cochlea
B
Cochlear nucleus
injection site
Basal turn
θb
E18.5
Middle turn
θm
E18.5
Sb
SAVCN
Sm
C
N.S
N.S
***
0.8
0.6
0.4
0.2
0.0
[(Sb/SAVCN * 100)/θb]
Control
Atoh1Hox2cKO
Atoh1Hoxa2cKO
Atoh1Hoxb2cKO
D
N.S
N.S
***
0.4
0.3
0.2
0.1
0.0
[(Sm/SAVCN * 100)/θm]
Control
Atoh1Hox2cKO
Atoh1Hoxa2cKO
Atoh1Hoxb2cKO

FIGURE 3

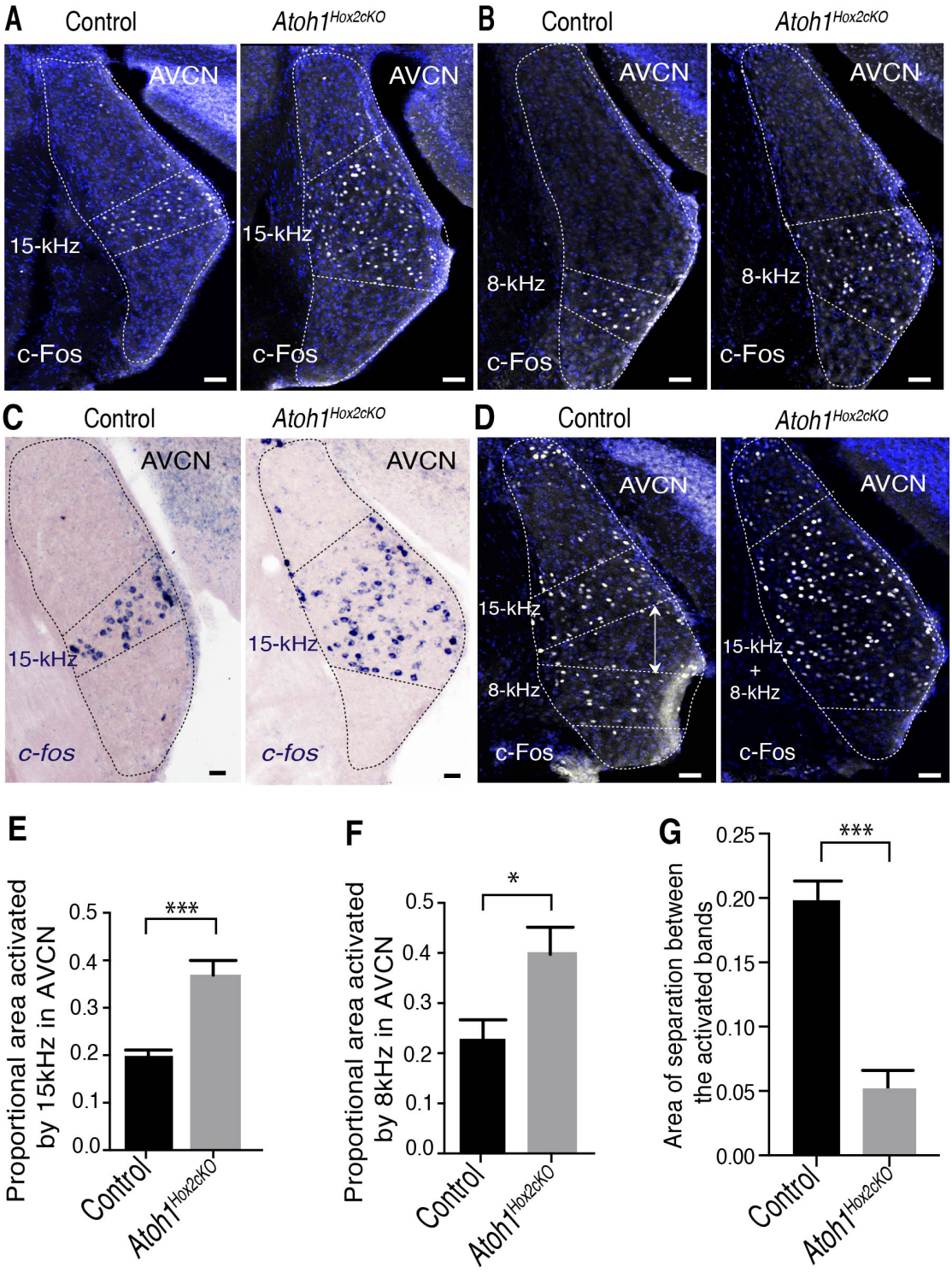
A
Control
Atoh1Hox2cKO
AVCN
15-kHz
c-Fos
B
8-kHz
C
c-fos
D
15-kHz
+
8-kHz
E
Proportional area activated by 15kHz in AVCN
***
0.5
0.4
0.3
0.2
0.1
0.0
F
Proportional area activated by 8kHz in AVCN
*
G
Area of separation between the activated bands
0.25
0.20
0.15
0.10
0.05
0.00

FIGURE 4

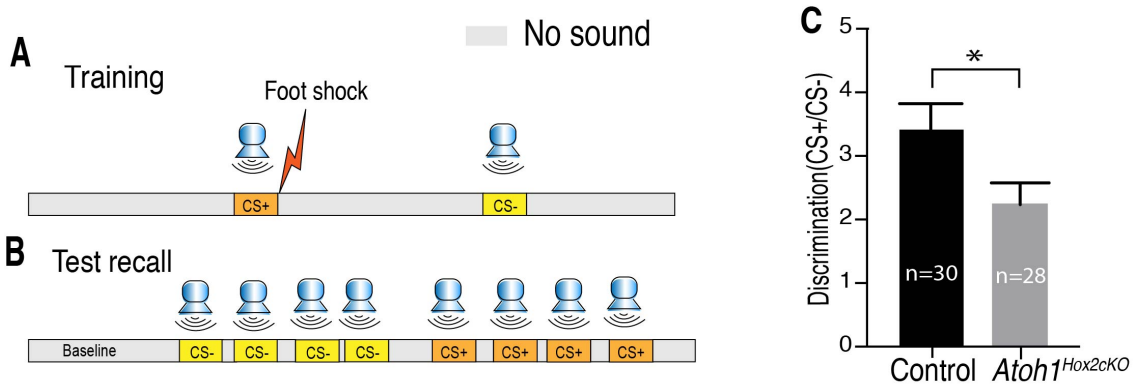
A
Training
No sound
Foot shock
CS+
CS-
B
Test recall
Baseline
CS-
CS-
CS-
CS-
CS+
CS+
CS+
CS+
C
Discrimination(CS+/CS-)
0
1
2
3
4
5
*
n=30
n=28
Control
Atoh1Hox2cKO

FIGURE 5

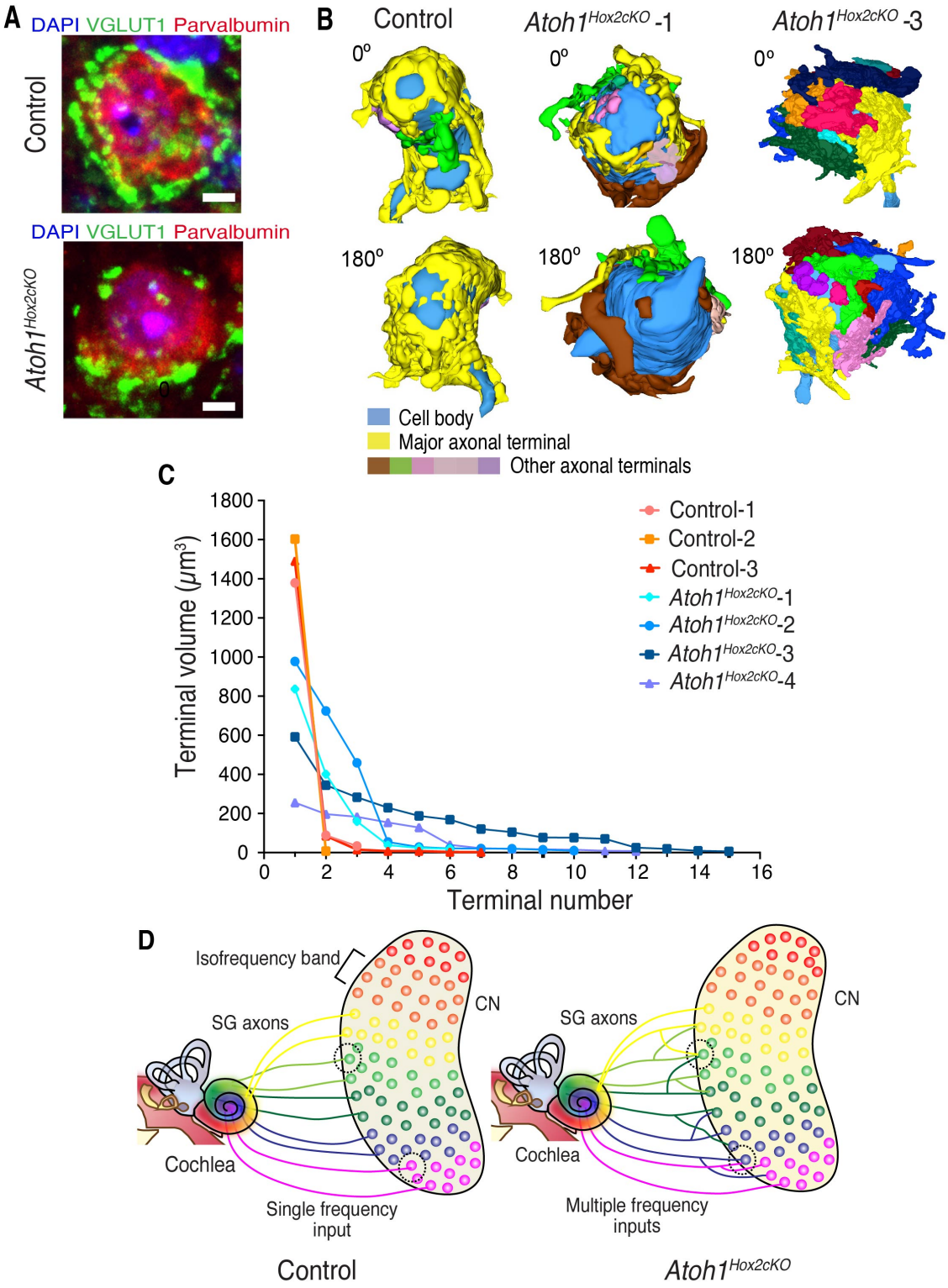
A
DAPI VGLUT1 Parvalbumin
Control
DAPI VGLUT1 Parvalbumin
Atoh1Hox2cKO
B
Control
Atoh1Hox2cKO -1
Atoh1Hox2cKO -3
0º
180º
Cell body
Major axonal terminal
Other axonal terminals
C
Terminal volume (μm3)
Terminal number
Control-1
Control-2
Control-3
Atoh1Hox2cKO-1
Atoh1Hox2cKO-2
Atoh1Hox2cKO-3
Atoh1Hox2cKO-4
D
Isofrequency band
SG axons
CN
Cochlea
Single frequency input
Multiple frequency inputs
Control
Atoh1Hox2cKO

FIGURE 6

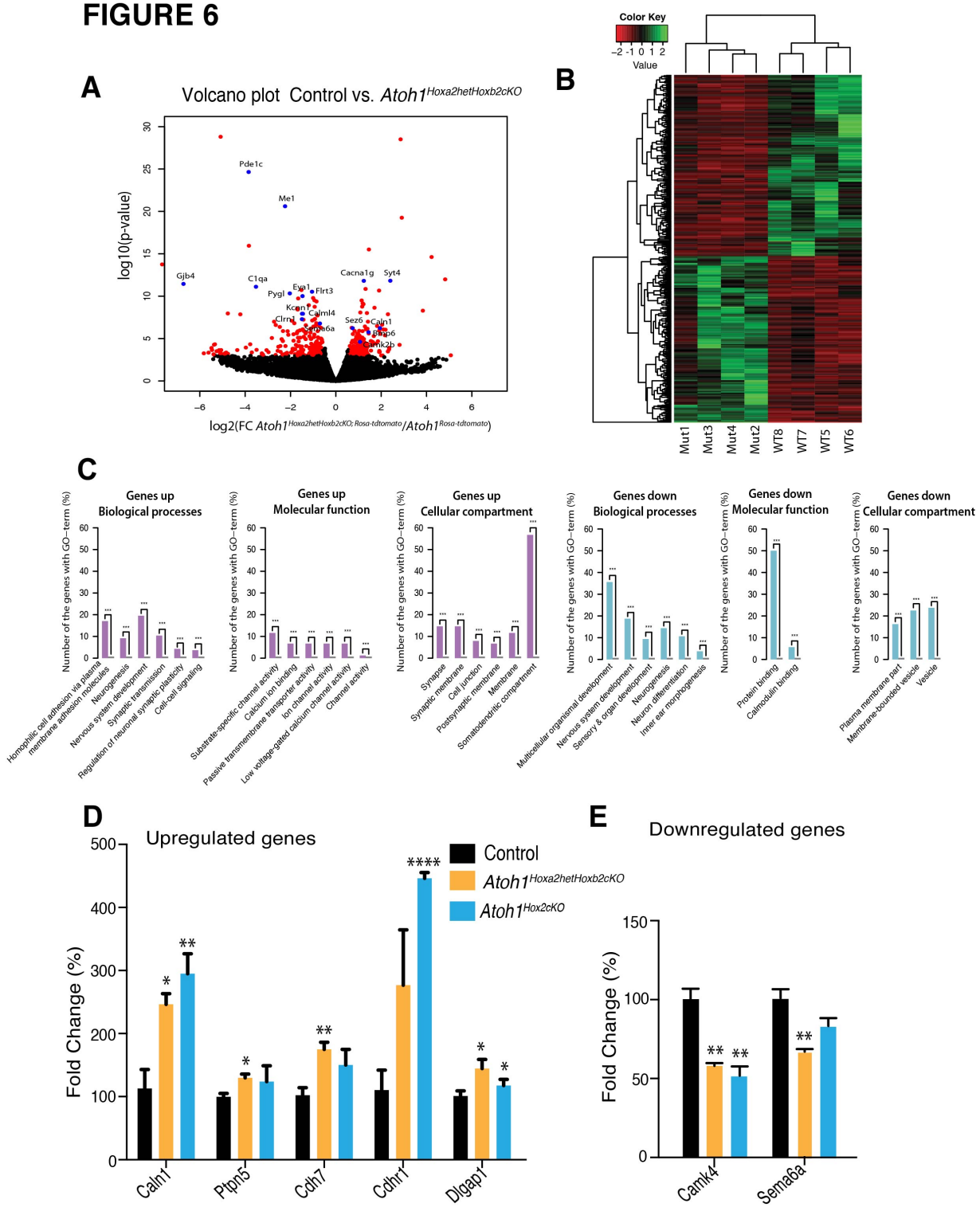
A
Volcano plot Control vs. Atoh1Hoxa2hetHoxb2cKO
log10(p-value)
log2(FC Atoh1Hoxa2hetHoxb2cKO;Rosa-tdtomato/Atoh1Rosa-tdtomato)
Pde1c
Me1
Gjb4
C1qa
Pygl
Eya1
Flrt3
Kcnn1
Calml4
Clrn1
Sema6a
Sez6
Caln1
Bhlhe6
Camk2b
Cacna1g
Syt4
B
Color Key
Value
Mut1
Mut3
Mut4
Mut2
WT8
WT7
WT5
WT6
C
Genes up Biological processes
Genes up Molecular function
Genes up Cellular compartment
Genes down Biological processes
Genes down Molecular function
Genes down Cellular compartment
Number of the genes with GO−term (%)
Homophilic cell adhesion via plasma membrane adhesion molecules
Neurogenesis
Nervous system development
Synaptic transmission
Regulation of neuronal synaptic plasticity
Cell-cell signaling
Substrate-specific channel activity
Calcium ion binding
Passive transmembrane transporter activity
Ion channel activity
Low voltage-gated calcium channel activity
Channel activity
Synapse
Synaptic membrane
Cell junction
Postsynaptic membrane
Membrane
Somatodendritic compartment
Multicellular organismal development
Nervous system development
Sensory & organ development
Neurogenesis
Neuron differentiation
Inner ear morphogenesis
Protein binding
Calmodulin binding
Plasma membrane part
Membrane-bounded vesicle
Vesicle
D
Upregulated genes
Fold Change (%)
Control
Atoh1Hoxa2hetHoxb2cKO
Atoh1Hox2cKO
Caln1
Ptpn5
Cdh7
Cdhr1
Dlgap1
E
Downregulated genes
Fold Change (%)
Camk4
Sema6a

SUPPLEMENTAL INFORMATION

FIGURE S1

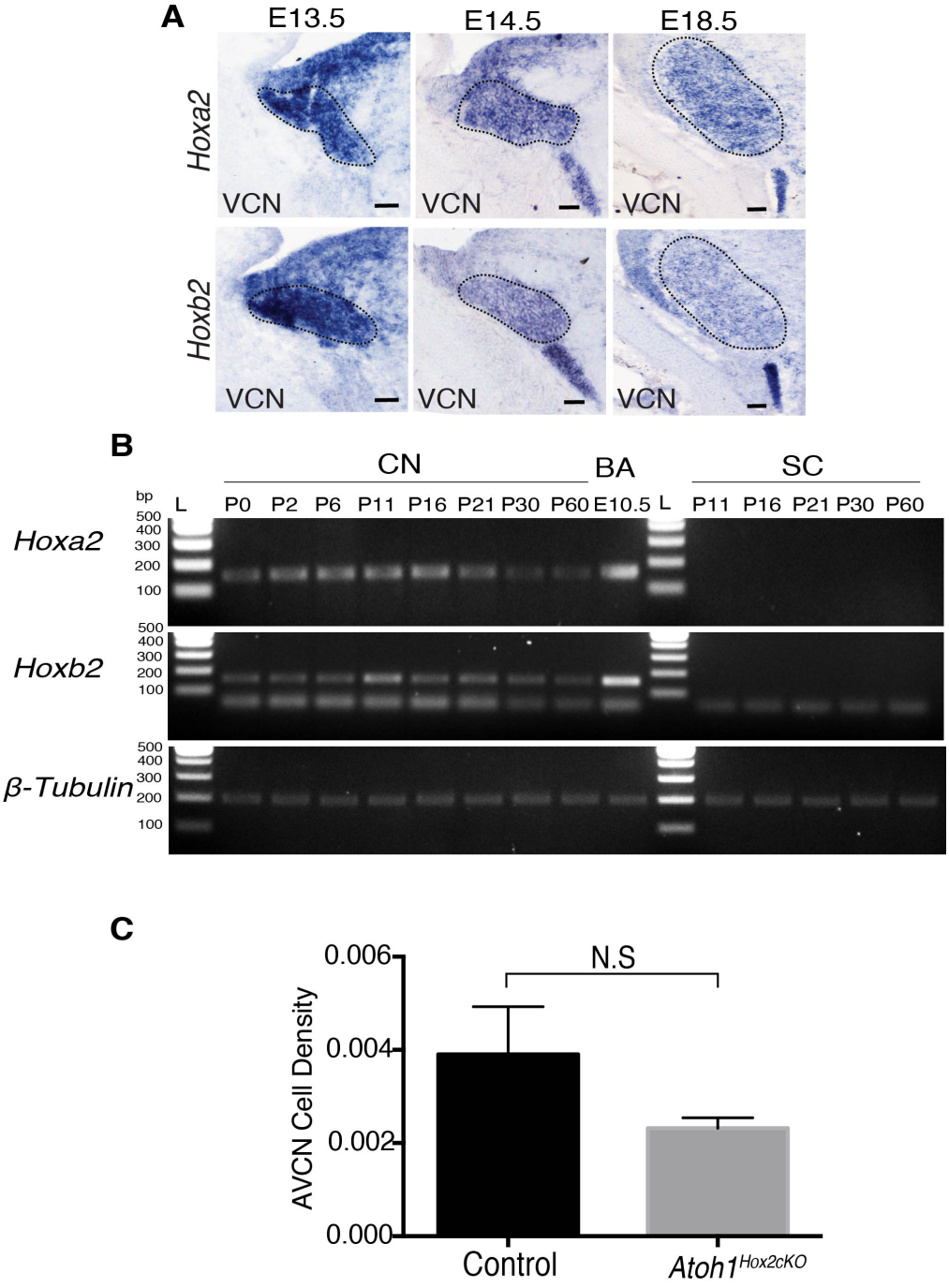

Figure S1: Temporal Expression Pattern of *Hox2* Genes in Ventral Cochlear Nucleus (Related to Figure 1)

(A) Temporal expression of *Hoxa2* and *Hoxb2* in AVCN during early and late embryonic stages (E13.5, E14.5 and E18.5) as detected by *in situ* hybridization with *Hoxa2* and *Hoxb2* RNA probes.

(B) *Hoxa2* and *Hoxb2* detection in AVCN by RT-PCR at early postnatal (P) stages P0, P2 and P6, P11 (in duplicates, each set comprising n=3 pups for P0 and P2, and n=1 pup for P6) and at late stages P16, P21, P30, P60 (in triplicates, each comprising n=1 animal). E10.5 branchial arch (BA) was used as a positive control and somatosensory cortex (SC) at P11, P16, P21, P30 and P60 was used as a negative control. Scale bar, 50 um.

(C) No significant difference of cell-density in control (n = 10) and $Atoh^{Hox2cKO}$ (n = 8) AVCN (P=0.1579, Mann-Whitney test).

FIGURE S2

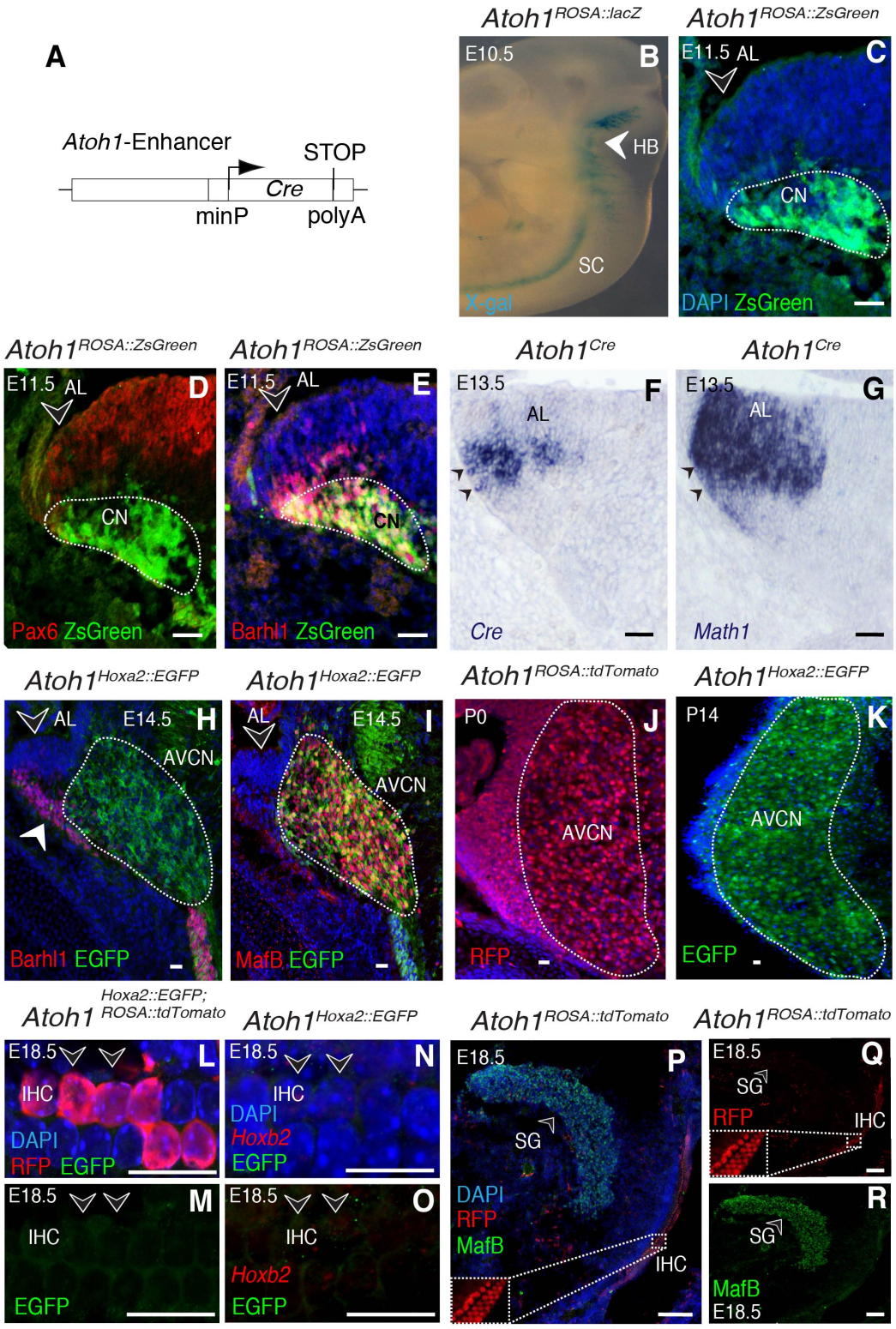
A
Atoh1-Enhancer
STOP
Cre
minP
polyA
Atoh1ROSA::lacZ
E10.5
B
HB
SC
X-gal
Atoh1ROSA::ZsGreen
E11.5 AL
C
CN
DAPI ZsGreen
Atoh1ROSA::ZsGreen
E11.5 AL
D
CN
Pax6 ZsGreen
Atoh1ROSA::ZsGreen
E11.5 AL
E
CN
Barhl1 ZsGreen
Atoh1Cre
E13.5
F
AL
Cre
Atoh1Cre
E13.5
G
AL
Math1
Atoh1Hoxa2::EGFP
AL
E14.5
H
AVCN
Barhl1 EGFP
Atoh1Hoxa2::EGFP
AL
E14.5
I
AVCN
MafB EGFP
Atoh1ROSA::tdTomato
P0
J
AVCN
RFP
Atoh1Hoxa2::EGFP
P14
K
AVCN
EGFP
Atoh1
Hoxa2::EGFP;
ROSA::tdTomato
E18.5
L
IHC
DAPI
RFP EGFP
E18.5
M
IHC
EGFP
Atoh1Hoxa2::EGFP
E18.5
N
IHC
DAPI
Hoxb2
EGFP
E18.5
O
IHC
Hoxb2
EGFP
Atoh1ROSA::tdTomato
E18.5
P
SG
DAPI
RFP
MafB
IHC
Atoh1ROSA::tdTomato
E18.5
Q
SG
RFP
IHC
E18.5
R
SG
MafB
E18.5

Figure S2: Characterization of *Atoh1*^{Cre} Mouse Line (Related to Figure 1)

(A) *Atoh1*^{Cre} construct used to generate the *Atoh1*^{Cre} line.

(B) In *Atoh1*^{Cre}*;ROSA::(LSL)lacZ* (*Atoh1*$^{Rosa::lacZ}$) embryos, earliest lacZ expression is detected at E10.5 by Xgal staining in hindbrain (HB) and spinal cord (SC).

(C-E) In *Atoh1*$^{Rosa::ZsGreen}$ E11.5 embryos, anti-ZsGreen antibody staining reveals ZsGreen expression in Barhl1^{+} (red) postmitotic neurons forming the cochlear nucleus (CN), but not in the auditory lip (AL) (open arrowhead) stained by anti-Pax6 (red).

(F-G) *Cre* and *Atoh1* mRNA expression in adjacent coronal sections through the E13.5 anterior ventral cochlear nucleus. *Cre* expression is barely detectable in the *Atoh1*$^{+}$ AL domain and mostly restricted to neurons ingressing the nucleus (arrowheads).

(H-I) *EGFP*$^{+}$ cells (green) in E14.5 *Atoh1*$^{Hoxa2::EGFP}$ fetuses, identifying *Atoh1*-derived *Hoxa2*-expressing cells, are selectively detected in the anterior ventral cochlear nucleus (AVCN) co-labeled with the MafB marker (red), and are excluded from AL (open arrowhead) and Barhl1^{+} (red) cochlear neurons in the migratory stream (arrowhead).

(J) *Atoh1*-derived neurons stained with anti-RFP in P0 *Atoh1*$^{Rosa::tdTomato}$ AVCN.

(K) *EGFP*$^{+}$ (green) cells identify *Atoh1*-derived *Hoxa2*-expressing neurons in P14 *Atoh1*$^{Hoxa2::EGFP}$ AVCN.

(L-O) In E18.5 in *Atoh1*$^{Hoxa2::EGFP;Rosa\text{-}tdTomato}$ specimen, cochlear hair cells are labeled with anti-RFP (red), confirming they are *Atoh1*-derived, but they do not express *Hoxa2*-driven EGFP nor *Hoxb2* (open arrowheads).

(**P-R**) In E18.5 inner ear *Atoh1*$^{Rosa::tdTomato}$, RFP (red) positive cells are not detected in the spiral ganglion (SG) labeled with MafB (green) (P and R). RFP (red) signal is detected in hair cells (P and inset in Q). Scale bar, 20um

FIGURE S3

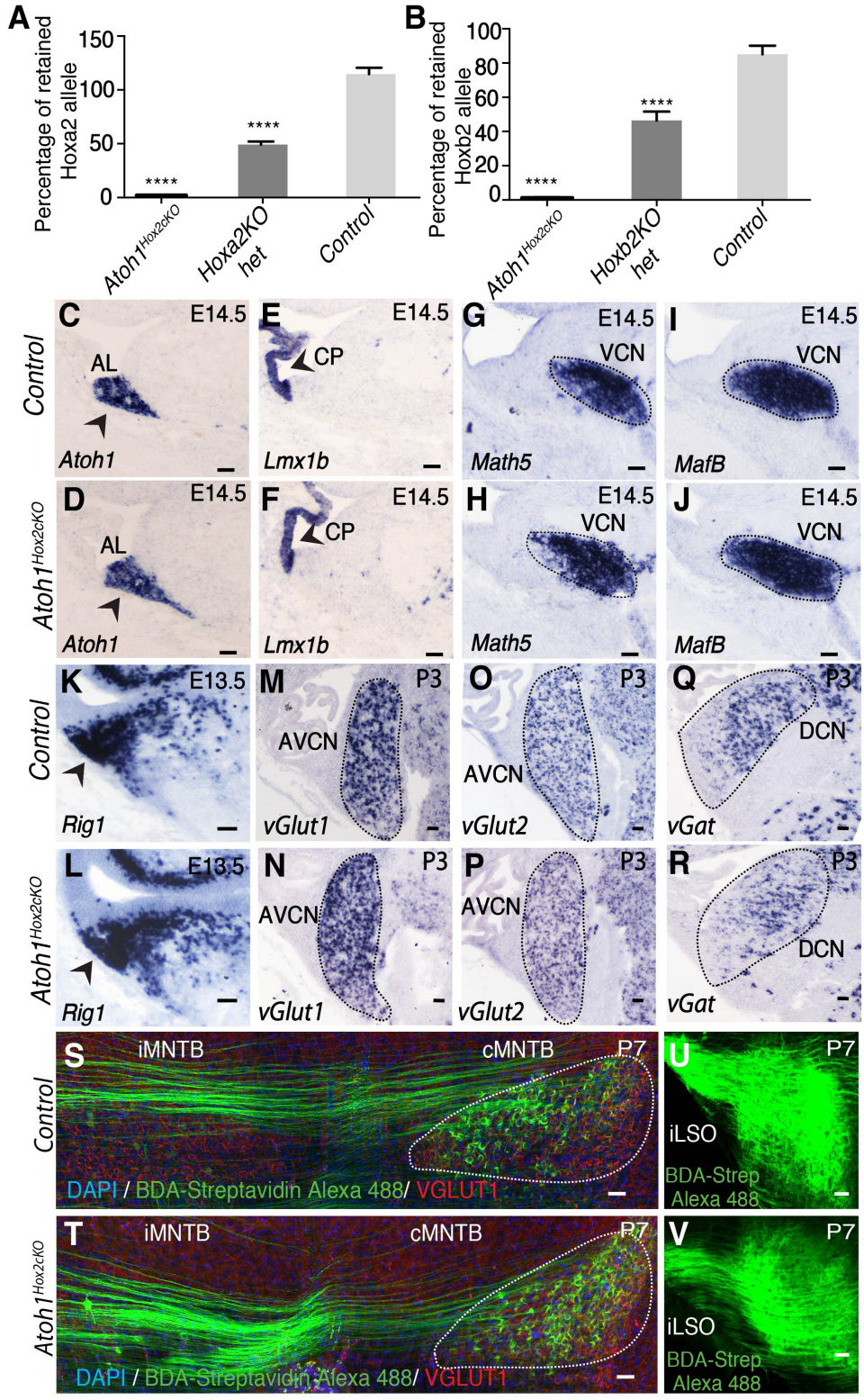
A
Percentage of retained Hoxa2 allele
150
100
50
0
****
****
Atoh1Hox2cKO
Hoxa2KO het
Control
B
Percentage of retained Hoxb2 allele
100
80
60
40
20
0
****
****
Atoh1Hox2cKO
Hoxb2KO het
Control
Control
Atoh1Hox2cKO
C E14.5 AL Atoh1
E E14.5 CP Lmx1b
G E14.5 VCN Math5
I E14.5 VCN MafB
D E14.5 AL Atoh1
F E14.5 CP Lmx1b
H E14.5 VCN Math5
J E14.5 VCN MafB
K E13.5 Rig1
M P3 AVCN vGlut1
O P3 AVCN vGlut2
Q P3 DCN vGat
L E13.5 Rig1
N P3 AVCN vGlut1
P P3 AVCN vGlut2
R P3 DCN vGat
S iMNTB cMNTB P7 DAPI / BDA-Streptavidin Alexa 488/ VGLUT1
U P7 iLSO BDA-Strep Alexa 488
T iMNTB cMNTB P7 DAPI / BDA-Streptavidin Alexa 488/ VGLUT1
V P7 iLSO BDA-Strep Alexa 488

Figure S3: Normal Cochlear Nucleus Patterning and Axon Guidance in *Atoh1*^{Hox2cKO} Mutants (Related to Figure 1)

(A-B) Quantitative PCR analysis to determine the degree of mosaicism of *Hox2* gene deletion in cochlear nuclei. Percentage of retained *Hoxa2* **(A)** and *Hoxb2* (**B**) alleles in E16.5 dissected and FACS isolated cochlear nuclei from conditional *Atoh1*$^{Hox2cKO;Rosa::tdTomato}$ double homozygous mutant animals (n = 7), as compared to *Hoxa2* heterozygous knockout (Hoxa2KO het, n = 4), *Hoxb2* heterozygous knockout (Hoxb2KO het, n = 4), and wild type control samples (n = 4, in (A); n = 5, in (B)) used as reference genotypes. Note nearly complete Cre-mediated excision of both *Hoxa2* and *Hoxb2* conditional alleles in conditional *Atoh1*$^{Hox2cKO;Rosa::tdTomato}$ cochlear nuclei (P< 0.0001).

(C-D) Normal *Atoh1* expression in E14.5 *Atoh1*^{Hox2cKO} (**D**) as compared to control (**C**) auditory lip (AL) and forming cochlear nucleus**.**

(E-F) Normal *Lmx1b* expression domain in developing choroid plexus (CP) in E14.5 *Atoh1*^{Hox2cKO} (**F**) as compared to control (**E**)**.**

(G-J) Normal *Math5* and *MafB* expression in E14.5 *Atoh1*^{Hox2cKO} (**H, J**) as compared to control (**G, I**) ventral cochlear nucleus (VCN).

(K-R) Normal expression of *Rig1* (**K, L)** at E13.5 and *vGlut1*, *vGlut2, vGat* (**M-R**) in P3 AVCN (**M, N, O, P**) and DCN (**Q, R**) in *Atoh1*^{Hox2cKO} (**L, N, P, R**) as compared to control (**K, M, O, Q**) specimen.

(**S-T**) Normal AVCN-MNTB contralateral connectivity at P7 in *Atoh1*^{Hox2cKO} (**T**) as compared to controls (**S**). VGLUT1 (red) staining labels nascent Calyx of Held synapses in MNTB.

(U-V) Normal AVCN-iLSO connectivity at P7 in *Atoh1*^{Hox2cKO}. (**V**) as compared to controls (**U**). AVCN, anterior ventral cochlear nucleus; cMNTB, contralateral medial nucleus of the trapezoid body; iMNTB, ipsilateral MNTB; iLSO, ipsilateral lateral superior olive. Scale bar, 50 um.

FIGURE S4

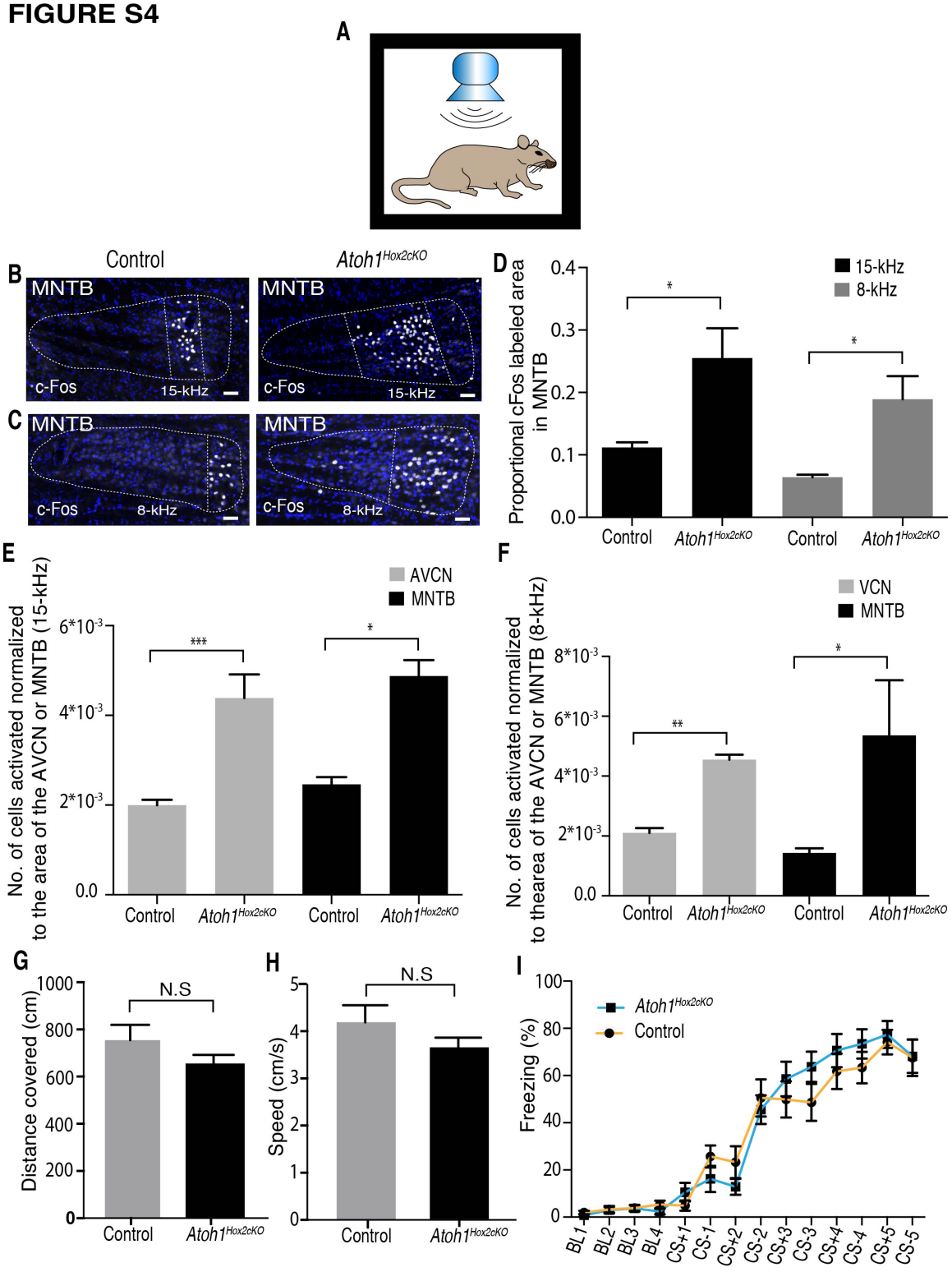
A
B
Control
Atoh1Hox2cKO
MNTB
c-Fos
15-kHz
C
8-kHz
D
Proportional cFos labeled area in MNTB
15-kHz
8-kHz
E
No. of cells activated normalized to the area of the AVCN or MNTB (15-kHz)
AVCN
MNTB
F
No. of cells activated normalized to thearea of the AVCN or MNTB (8-kHz)
VCN
G
Distance covered (cm)
N.S
H
Speed (cm/s)
I
Freezing (%)
BL1
BL2
BL3
BL4
CS+1
CS-1
CS+2
CS-2
CS+3
CS-3
CS+4
CS-4
CS+5
CS-5

Figure S4 Altered Isofrequency Bands of c-Fos Activation Upon Pure Tone Stimulation in Adult Mutants (Related to Figure 3).

(A) Drawing of auditory stimulation set-up. Mice are placed in a sound proof chamber and pure-tones are played through speakers placed in the chamber.

(B-C) anti-c-Fos immunostaining showing c-Fos expressing bands of activated cells in MNTB in response to 15 kHz (**B**) or 8 kHz (**C**) stimulation in control and *Atoh1*^{Hox2cKO} adult mice. Note the increase of c-fos activation area in mutants.

(D) Quantification of activation areas in MNTB normalized to total MNTB size in response to 15 kHz stimulation (black bars) in control (n = 5) and *Atoh1*^{Hox2cKO} (n = 3) animals (P=0.0357, Mann-Whitney test); and in response to 8-kHz stimulation (grey bars) in control (n = 3) and *Atoh1*^{Hox2cKO} (n = 4) animals, (P=0.045, Mann-Whitney test).

(E) Quantification of the number of c-fos activated cells in response to 15 kHz stimulation in AVCN or MNTB, normalized to AVCN or MNTB total size, respectively, in control (n=5) and *Atoh1*^{Hox2cKO} (n = 3) animals (AVCN P=0.0001, MNTB P=0.035, Mann-Whitney tests).

(F) Quantification of the number of c-fos activated cells in response to 8 kHz stimulation in AVCN or MNTB, normalized to AVCN or MNTB total size, respectively, in control (n=3) and *Atoh1*^{Hox2cKO} (n = 3) animals, (AVCN P=0.0043, MNTB P=0.0112, Mann-Whitney tests).

(G-H) Quantification of the distance travelled and speed of control (n = 18) and *Atoh1*^{Hox2cKO} (n = 18) animals in a discriminative fear-conditioning set-up show no significant difference (P = 0.2, Unpaired, two-tailed, Student's t-test).

(**I**) Comparison of fear-acquisition in control (n = 18) and *Atoh1*^{Hox2cKO} (n = 18) animals in a discriminative fear-conditioning set-up showed no significant differences between the control and mutant animals (Two-way ANOVA).

Supplementary Table 1. Differentially expressed genes after conditional deletion of *HoxPG2* (*Math1*$^{HoxPG2cKO;ROSA::tdTomato}$ at E18.5) (FC>1.5; p-value: <0.01)			
Downregulated		**Upregulated**	
p-value	**Gene**	**p-value**	**Gene**
1.89E-21	**Rps2-ps13**	0.000623845	**2310061I04Rik**
1.78E-14	**Rps2-ps10**	0.000926733	**Gabra4**
3.53E-12	**Gjb4**	7.39E-05	**Lrp8**
0.000541891	**Gm15840**	0.000389868	**Arl4a**
0.000455243	**Olfr807**	0.000335416	**Lhfp**
0.000128156	**1110036E04Rik**	0.000251023	**Cdh4**
0.000223086	**Gm11392**	0.000482318	**Tspan7**
0.00071059	**Gm12189**	0.000384484	**Tshz2**
5.26E-05	**Gm13658**	0.00077407	**Scoc**
0.000885436	**Olfr303**	0.000460932	**Rps28**
4.68E-05	**Gm15195**	0.00085514	**Ccdc28b**
0.000308087	**4930544G11Rik**	0.000109473	**Rnf150**
0.00023023	**n-R5s47**	0.000651321	**Coa3**
0.000867387	**Gm13560**	3.04E-05	**Frmd5**
0.000438233	**Gm14153**	0.000133482	**Slc36a1**
1.57E-29	**Gm13225**	0.000379228	**Slco3a1**

0.000226314	**Olfr152**	5.29E-07	**Nr2f2**
0.000644571	**Treml1**	0.000111646	**St8sia1**
0.000756921	**Gm13761**	0.00053064	**Sertm1**
0.000514864	**Vmn2r-ps84**	0.000265627	**Ptchd2**
0.000558109	**Gm22275**	0.000254223	**Rims1**
0.000440961	**Gnat3**	0.000654587	**Lrrc75b**
1.08E-08	**BC023719**	0.000481373	**Lrrtm3**
0.000621457	**Olfr341**	0.000902409	**1110001J03Rik**
0.000224889	**Gm10466**	0.000952431	**Grin1**
1.37E-08	**H2-T10**	1.79E-05	**Ppfia2**
0.000113848	**mt-Tf**	5.92E-07	**Sez6**
2.23E-25	**Pde1c**	2.92E-06	**Tbc1d9**
1.12E-16	**Padi4**	0.000370343	**Rps4l**
4.66E-05	**Gjb1**	0.000735424	**Dnm1**
0.000426866	**Nme8**	7.30E-05	**Dlgap1**
7.68E-12	**C1qa**	0.000582484	**BC046401**
0.000211601	**Gpr144-ps**	0.000186088	**Ptprj**
0.000547063	**Gpr132**	0.000163443	**H2-T24**
0.000947333	**Slc5a4a**	0.000306544	**Gm15663**

0.000808336	**Psmb9**	1.27E-06	**Fam65b**
8.17E-42	**Hoxb2**	0.000203016	**Shank2**
0.000229635	**Osgin1**	0.000660468	**Clcf1**
0.0003973	**5430416O09Rik**	0.000639392	**Miip**
8.49E-06	**Laptm5**	0.000220269	**Gabrb1**
1.00E-07	**1700001O22Rik**	2.72E-05	**Mlf1**
0.000839499	**Acrv1**	0.000138904	**Nptx1**
2.51E-07	**9330185C12Rik**	2.12E-05	**Arhgap20**
0.000276331	**Gm22116**	0.000567825	**Galnt14**
9.18E-05	**Ren1**	1.27E-05	**Slc35f1**
4.22E-07	**Gm5105**	0.000289561	**Tmsb15l**
7.54E-05	**Cx3cr1**	0.000711185	**Lin7a**
0.000365137	**Aif1**	0.000462311	**Gm13139**
1.16E-05	**G530011O06Rik**	0.000230868	**Fam196a**
0.000750009	**AI467606**	0.000106992	**ENSMUSG00000078821**
1.96E-05	**Rbp4**	0.000266552	**Tmsb15b2**
1.29E-06	**Gm14403**	1.18E-05	**Cdh11**
0.00073571	**Mylk2**	6.01E-06	**Lrrtm4**
2.45E-21	**Me1**	0.00094462	**Glt1d1**

7.56E-05	**Lect1**	0.000479324	**Tmem179**
0.000588468	**Clec4e**	9.19E-05	**Negr1**
0.000603925	**Gm831**	8.08E-05	**Rspo2**
0.000473517	**Itgal**	0.000385444	**Grm5**
1.34E-06	**Slfn9**	0.000793117	**Prdm16**
3.57E-06	**P2ry12**	0.000795853	**Olfm3**
4.65E-11	**Pygl**	1.01E-05	**Ly6h**
0.000434101	**Cngb1**	0.000952019	**Dmtn**
7.87E-08	**Rassf9**	2.61E-06	**Rorb**
0.000255169	**Mal**	0.000153033	**Fbxo44**
0.000157721	**A2m**	0.000236873	**Chl1**
3.07E-06	**Tlr6**	0.000239208	**Ucma**
1.76E-05	**Gm4792**	5.15E-05	**Ankrd6**
0.000163213	**Prdm1**	2.79E-06	**Cdh13**
1.55E-07	**4931429I11Rik**	0.000272334	**Fgd5**
0.000173447	**Gm15726**	6.45E-05	**Lrfn5**
0.000681465	**Wnt3a**	0.000266222	**Sh3rf3**
0.000181698	**Irf8**	0.000897309	**Stxbp2**
5.58E-05	**B430212C06Rik**	0.000525103	**Cdh7**

2.39E-06	**Tmod4**	0.000108269	**Map3k5**
1.81E-06	**Wdr96**	2.86E-06	**Cttnbp2**
3.11E-09	**Gsta4**	0.00017407	**Plch2**
0.000598282	**Gm2093**	0.000622717	**Slc26a1**
7.78E-05	**Cldn1**	8.95E-05	**Frem2**
0.00095558	**Gm15606**	6.85E-05	**Slitrk4**
3.77E-09	**Hpgds**	0.000159549	**Ank1**
1.38E-06	**F13a1**	0.000924442	**Rapgef3**
7.82E-06	**Ccdc68**	0.000728184	**Sncb**
0.000512721	**Gm20475**	0.00017033	**Fxyd6**
1.83E-10	**Slc35f4**	9.76E-05	**Kcnd2**
0.000387204	**Strc**	0.000284922	**Calb2**
2.15E-05	**Gm27868**	3.19E-05	**Rpl34**
0.000658973	**Myof**	1.20E-06	**Syt7**
7.49E-05	**Slc39a12**	0.000246105	**Ablim1**
1.07E-06	**Col8a1**	0.000546103	**4930506M07Rik**
0.000488278	**Mroh8**	9.16E-06	**Csf2ra**
7.77E-06	**H2-K1**	4.57E-06	**Ajap1**
0.000632787	**ENSMUSG00000079246**	0.000646305	**Gm5454**

0.000144532	**Igf2**	6.54E-05	**Vstm2a**
0.000257446	**Npc1l1**	2.00E-05	**Col27a1**
0.0005042	**Gm22814**	0.000471633	**Perp**
1.88E-11	**Gm10263**	9.10E-05	**Vegfc**
0.000203654	**C130046K22Rik**	1.09E-05	**Ptpn5**
8.62E-05	**Gm15049**	0.000659492	**Adap1**
0.000954417	**Tubd1**	2.41E-05	**Camk2b**
5.12E-08	**Calml4**	0.000136411	**Gfra4**
0.000403218	**Ccdc3**	0.000366378	**Glra2**
1.17E-08	**Clrn1**	8.33E-09	**Ehd3**
0.000426655	**Gm26776**	0.000207858	**Cacna1i**
9.73E-11	**Eya1**	0.000378163	**Ppargc1b**
7.95E-07	**Zfp503**	0.000739787	**Dennd1c**
1.18E-08	**Kcnn1**	0.000981787	**ENSMUSG00000073231**
0.000216426	**Ly75**	0.000153755	**Rims4**
5.87E-08	**Impg2**	9.13E-05	**Bend5**
6.16E-06	**Hotairm1**	9.44E-05	**Mpped1**
0.000849337	**Rec8**	0.000777437	**9330158H04Rik**
1.29E-06	**Klhl1**	3.17E-10	**Epb4.1l4b**

6.63E-06	**Gm12846**	0.000122602	**Rpph1**
0.000924415	**Gldn**	0.000832598	**Ralyl**
2.46E-06	**Ror2**	1.69E-09	**Rnf157**
1.16E-05	**Nts**	7.41E-06	**Ptprr**
2.65E-07	**Mybpc1**	3.42E-05	**Nrg3**
1.77E-06	**Pou3f3**	0.0002475	**Arhgef15**
7.65E-05	**Mbnl3**	4.29E-05	**Dleu7**
0.000934658	**A230052G05Rik**	0.000122031	**Smim3**
1.15E-09	**Meis2**	0.000563504	**Gpr88**
0.000593361	**Fkbp10**	1.32E-06	**Etv1**
0.000814807	**Lhx1**	7.06E-10	**Id4**
5.31E-06	**Neurod4**	2.19E-05	**Igsf5**
0.000116249	**Gm9990**	0.000540653	**Nrsn2**
0.000150446	**Slc2a5**	6.36E-05	**Fstl5**
0.000467964	**Ccdc80**	6.58E-05	**Ankrd34a**
1.93E-06	**Nefm**	0.000315006	**Pnoc**
6.77E-07	**Slit2**	8.67E-10	**Slc6a17**
1.08E-05	**Gpc4**	0.000828294	**Elmod1**
0.000276373	**Greb1**	1.54E-12	**Cacna1g**

1.09E-05	**Fam210b**	1.12E-05	**Chrm2**
4.01E-05	**Opcml**	0.000911349	**C1qtnf4**
0.000765809	**Ccl28**	2.80E-05	**Hfm1**
2.96E-11	**Flrt3**	4.74E-05	**Rasgrf1**
8.38E-05	**Dab2**	0.000183604	**4930586N03Rik**
0.000781186	**9130024F11Rik**	0.000845895	**Resp18**
7.29E-08	**Inadl**	0.000587275	**Tcerg1l**
0.000361433	**5830432E09Rik**	8.75E-05	**Prrt4**
0.000187035	**Ung**	3.71E-07	**Mctp1**
0.000159608	**Cadps2**	0.000854768	**Slc27a2**
5.68E-05	**Gm10182**	1.39E-11	**Irak1bp1**
1.63E-10	**Nhlh1**	0.000772104	**S100a10**
0.000831644	**Gm15723**	8.09E-07	**Pcp4**
0.000647727	**4930545L23Rik**	0.000204397	**Krt222**
0.000528056	**Tph1**	0.000110094	**Pcdh11x**
0.000784405	**4930529M08Rik**	0.000442883	**Hs3st2**
3.82E-07	**Adi1**	9.68E-09	**Cyp26b1**
6.54E-05	**Rwdd3**	0.000102999	**Oprm1**
0.000359416	**Rsad1**	4.21E-05	**Trank1**

6.58E-06	**Lmo3**	6.87E-07	**Cygb**
5.71E-08	**Gm16140**	8.13E-05	**Klhl14**
7.92E-05	**Hddc3**	1.00E-07	**Csmd3**
3.34E-06	**Vav3**	0.000793474	**Cidea**
3.05E-10	**Stard4**	1.75E-06	**Bmp6**
1.76E-09	**Gm20488**	2.51E-06	**Zim1**
0.000500726	**Nfkbiz**	3.08E-16	**Tmem132b**
4.76E-08	**Gab1**	1.94E-05	**Col15a1**
3.37E-07	**Camk4**	0.000259581	**Lrrc3b**
0.000154261	**Piezo1**	2.13E-05	**4930426D05Rik**
3.01E-05	**Akap2**	5.98E-05	**Trpc4**
0.000614432	**Satb2**	2.49E-05	**Dpp10**
1.53E-07	**Epb4.1l4a**	4.22E-05	**Fgf10**
0.00030522	**Atic**	3.39E-05	**Morc2b**
0.000696997	**Insm1**	5.05E-06	**Ooep**
4.15E-10	**Cdon**	2.30E-09	**Cdhr1**
0.000572998	**Il1rap**	3.92E-05	**Bmp2**
0.000506918	**Phka1**	3.28E-07	**Gm11346**
2.10E-05	**Gm7809**	2.07E-05	**Gm26658**

0.00030688	**Wwc1**	2.16E-11	**Svep1**
4.31E-05	**BC052040**	0.000382884	**ENSMUSG00000058736**
3.28E-05	**Pgm2**	1.15E-06	**Gm26889**
1.88E-08	**Myo1b**	0.000280809	**Igf1**
0.000476048	**Rin2**	0.000372377	**Fam19a1**
6.87E-05	**Gadd45a**	5.80E-07	**Caln1**
0.000281474	**Dock5**	2.78E-06	**Ankrd63**
1.30E-06	**Vat1l**	0.000966392	**Gm10654**
0.000112068	**Abtb2**	2.32E-07	**Mal2**
7.10E-06	**Gm12892**	0.000968496	**Gm15940**
0.0004633	**Limd1**	8.36E-07	**Fxyd2**
0.000208903	**Myo6**	4.10E-06	**Drd5**
0.000568973	**Mcm2**	8.92E-07	**2610305D13Rik**
4.94E-05	**Prkd3**	0.00033206	**1700012C14Rik**
0.00017685	**Plcd1**	1.34E-08	**Gm13157**
8.49E-06	**Dach2**	0.000187466	**BC049715**
0.000275831	**Pcsk9**	0.000120364	**Gm27199**
2.81E-07	**Sphkap**	1.50E-12	**Syt4**
0.000286397	**Palm2Akap2**	5.48E-05	**Gm15691**

1.88E-07	**Plcb1**	3.12E-29	**AA465934**
0.0006579	**BC034090**	5.51E-20	**C920006O11Rik**
0.000912943	**Cxcl14**	5.10E-09	**Obp1a**
7.65E-05	**Tmem229a**	2.40E-15	**Rprml**
0.000126019	**Barhl2**	1.03E-12	**2610528A11Rik**
0.000248458	**Ptch2**	0.000928569	**Gm13213**
3.96E-05	**Gm9825**	1.56E-218	**Hoxb1**
0.000185225	**Golm1**		
0.000383375	**Abcc8**		
1.64E-07	**Sema6a**		
0.000602091	**Gm11868**		
0.000564864	**Dpp6**		
3.90E-05	**Gm11223**		
0.00058412	**Gm12435**		
0.000269621	**Iqgap2**		
0.000445802	**Trhde**		
5.19E-07	**Meis1**		
9.87E-06	**Fbxl3**		
0.000109256	**Tnfaip8**		

0.000163237	**Rai14**		
3.05E-05	**Usp25**		
1.18E-05	**Medag**		
1.55E-05	**Ebf3**		
0.000974033	**Trim28**		
2.62E-05	**Nrip1**		

Supplementary Table 2. GO enrichment analysis					
GO ANALYSIS: DOWNREGULATED : BIOLOGICAL PROCESSES					
Term	**Background frequency**	**Sample frequency**	**Expected**	**+/-**	**P-value**
multicellular organismal development (GO:0007275)	3813	57	2.74E+01	+	2.62E-06
single-multicellular organism process (GO:0044707)	5798	74	4.17E+01	+	5.23E-06
system development (GO:0048731)	3264	50	2.35E+01	+	1.44E-05
multicellular organismal process (GO:0032501)	5971	74	4.29E+01	+	1.91E-05
single-organism developmental process (GO:0044767)	4310	59	3.10E+01	+	3.18E-05
developmental process (GO:0032502)	4321	59	3.10E+01	+	3.49E-05
positive regulation of biological process (GO:0048518)	3907	53	2.81E+01	+	2.53E-04
nervous system development (GO:0007399)	1617	30	1.16E+01	+	2.67E-04
anatomical structure development (GO:0048856)	3829	52	2.75E+01	+	3.24E-04
organ development (GO:0048513)	2411	38	1.73E+01	+	4.42E-04
embryonic organ development (GO:0048568)	424	14	3.05E+00	+	4.93E-04
sensory organ development (GO:0007423)	490	15	3.52E+00	+	5.36E-04
positive regulation of cellular process	3511	48	2.52E+01	+	8.09E-04

(GO:0048522)					
embryonic retina morphogenesis in camera-type eye (GO:0060059)	7	3	5.03E-02	+	3.53E-03
neurogenesis (GO:0022008)	1209	23	8.68E+00	+	3.55E-03
generation of neurons (GO:0048699)	1136	22	8.16E+00	+	4.19E-03
cell differentiation (GO:0030154)	2807	39	2.02E+01	+	6.04E-03
single-organism process (GO:0044699)	11813	110	8.49E+01	+	6.63E-03
neuron differentiation (GO:0030182)	764	17	5.49E+00	+	7.15E-03
cellular developmental process (GO:0048869)	2946	40	2.12E+01	+	7.84E-03
embryonic organ morphogenesis (GO:0048562)	287	10	2.06E+00	+	8.74E-03
positive regulation of embryonic development (GO:0040019)	11	3	7.90E-02	+	1.34E-02
cell development (GO:0048468)	1321	23	9.49E+00	+	1.37E-02
inner ear morphogenesis (GO:0042472)	101	6	7.26E-01	+	1.79E-02
negative regulation of smooth muscle cell chemotaxis (GO:0071672)	2	2	1.44E-02	+	1.79E-02
positive regulation of gene expression (GO:0010628)	1255	22	9.02E+00	+	1.81E-02
cellular component movement (GO:0006928)	922	18	6.62E+00	+	2.21E-02
regulation of cell differentiation (GO:0045595)	1295	22	9.30E+00	+	2.82E-02
response to stimulus (GO:0050896)	6812	71	4.89E+01	+	2.88E-02
epithelium development (GO:0060429)	859	17	6.17E+00	+	2.93E-02
organ morphogenesis (GO:0009887)	780	16	5.60E+00	+	3.08E-02

positive regulation of cell adhesion (GO:0045785)	160	7	1.15E+00	+	3.11E-02
tissue development (GO:0009888)	1402	23	1.01E+01	+	3.29E-02
positive regulation of cellular biosynthetic process (GO:0031328)	1407	23	1.01E+01	+	3.46E-02
localization of cell (GO:0051674)	630	14	4.53E+00	+	3.56E-02
cell motility (GO:0048870)	630	14	4.53E+00	+	3.56E-02
biological regulation (GO:0065007)	10055	95	7.22E+01	+	3.65E-02
positive regulation of transcription, DNA-templated (GO:0045893)	1141	20	8.20E+00	+	3.83E-02
pallium development (GO:0021543)	117	6	8.40E-01	+	3.93E-02
regulation of smooth muscle cell chemotaxis (GO:0071671)	3	2	2.16E-02	+	4.00E-02
positive regulation of RNA biosynthetic process (GO:1902680)	1153	20	8.28E+00	+	4.39E-02
cell migration (GO:0016477)	566	13	4.07E+00	+	4.41E-02
positive regulation of metabolic process (GO:0009893)	2230	31	1.60E+01	+	4.59E-02
positive regulation of biosynthetic process (GO:0009891)	1436	23	1.03E+01	+	4.63E-02
ear morphogenesis (GO:0042471)	121	6	8.69E-01	+	4.70E-02
microglial cell activation (GO:0001774)	17	3	1.22E-01	+	4.79E-02
inner ear development (GO:0048839)	176	7	1.26E+00	+	5.51E-02
positive regulation of RNA metabolic process (GO:0051254)	1178	20	8.46E+00	+	5.78E-02
locomotion (GO:0040011)	830	16	5.96E+00	+	6.11E-02

positive regulation of neural precursor cell proliferation (GO:2000179)	46	4	3.30E-01	+	6.51E-02
localization (GO:0051179)	3818	45	2.74E+01	+	6.59E-02
regulation of developmental process (GO:0050793)	1775	26	1.28E+01	+	7.11E-02
cerebral cortex development (GO:0021987)	87	5	6.25E-01	+	7.95E-02
positive regulation of macromolecule metabolic process (GO:0010604)	1991	28	1.43E+01	+	7.96E-02
neuron development (GO:0048666)	603	13	4.33E+00	+	8.00E-02
positive regulation of macromolecule biosynthetic process (GO:0010557)	1311	21	9.42E+00	+	8.74E-02
embryonic morphogenesis (GO:0048598)	538	12	3.86E+00	+	9.87E-02
eye morphogenesis (GO:0048592)	140	6	1.01E+00	+	1.01E-01
negative regulation of hippo signaling (GO:0035331)	5	2	3.59E-02	+	1.10E-01
skeletal muscle satellite cell differentiation (GO:0014816)	5	2	3.59E-02	+	1.10E-01
brain development (GO:0007420)	475	11	3.41E+00	+	1.24E-01
ear development (GO:0043583)	203	7	1.46E+00	+	1.28E-01
GO ANALYSIS: DOWNREGULATED: MOLECULAR FUNCTION					
Term	**Background frequency**	**Sample frequency**	**Expected**	**+/-**	**P-value**

protein binding (GO:0005515)	7091	80	5.09E+01	+	1.10E-04
calmodulin binding (GO:0005516)	151	9	1.09E+00	+	1.43E-04
binding (GO:0005488)	11596	107	8.33E+01	+	8.14E-03
phosphatidylinositol-4,5-bisphosphate binding (GO:0005546)	40	4	2.87E-01	+	1.73E-02
phosphatidylinositol phosphate binding (GO:1901981)	91	5	6.54E-01	+	4.37E-02
phosphatidylinositol bisphosphate binding (GO:1902936)	57	4	4.09E-01	+	6.48E-02
chemorepellent activity (GO:0045499)	7	2	5.03E-02	+	9.60E-02

GO ANALYSIS: DOWNREGULATED: CELLULAR COMPONENT

Term	Background frequency	Sample frequency	Expected	+/-	P-value
plasma membrane part (GO:0044459)	1786	26	1.28E+01	+	2.93E-02
membrane-bounded vesicle (GO:0031988)	2861	36	2.06E+01	+	3.45E-02
vesicle (GO:0031982)	3091	38	2.22E+01	+	3.66E-02
extracellular region part (GO:0044421)	3243	39	2.33E+01	+	4.68E-02

GO ANALYSIS: UPREGULATED: BIOLOGICAL PROCESSES

Term	Background frequency	Sample frequency	Expected	+/-	P-value

neurogenesis (GO:0022008)	1209	28	8.90E+00	+	1.32E-05
synaptic transmission (GO:0007268)	381	15	2.81E+00	+	3.32E-05
nervous system development (GO:0007399)	1617	32	1.19E+01	+	4.81E-05
cell-cell signaling (GO:0007267)	557	17	4.10E+00	+	1.68E-04
homophilic cell adhesion via plasma membrane adhesion molecules (GO:0007156)	76	7	5.60E-01	+	3.30E-04
regulation of neuronal synaptic plasticity (GO:0048168)	51	6	3.76E-01	+	4.58E-04
regulation of long-term neuronal synaptic plasticity (GO:0048169)	33	5	2.43E-01	+	9.60E-04
generation of neurons (GO:0048699)	1136	23	8.36E+00	+	2.00E-03
system development (GO:0048731)	3264	45	2.40E+01	+	2.91E-03
cell-cell adhesion via plasma-membrane adhesion molecules (GO:0098742)	108	7	7.95E-01	+	3.17E-03
cell-cell adhesion (GO:0098609)	108	7	7.95E-01	+	3.17E-03
primary metabolic process (GO:0044238)	7043	28	5.19E+01	-	3.22E-03
regulation of membrane potential (GO:0042391)	249	10	1.83E+00	+	3.30E-03
regulation of synaptic plasticity (GO:0048167)	120	7	8.84E-01	+	6.17E-03
regulation of nervous system development (GO:0051960)	621	15	4.57E+00	+	1.11E-02
anatomical structure morphogenesis (GO:0009653)	1820	29	1.34E+01	+	1.15E-02

multicellular organismal development (GO:0007275)	3813	48	2.81E+01	+	1.47E-02
anatomical structure development (GO:0048856)	3829	48	2.82E+01	+	1.63E-02
metabolic process (GO:0008152)	7936	36	5.84E+01	-	1.88E-02
positive regulation of cell-matrix adhesion (GO:0001954)	33	4	2.43E-01	+	2.04E-02
regulation of synaptic transmission (GO:0050804)	254	9	1.87E+00	+	2.22E-02
organic substance metabolic process (GO:0071704)	7278	32	5.36E+01	-	2.25E-02
regulation of osteoblast differentiation (GO:0045667)	106	6	7.80E-01	+	2.65E-02
single-organism localization (GO:1902578)	2415	34	1.78E+01	+	2.80E-02
positive regulation of developmental process (GO:0051094)	855	17	6.30E+00	+	3.73E-02
regulation of cell communication (GO:0010646)	2354	33	1.73E+01	+	3.87E-02
regulation of neurogenesis (GO:0050767)	553	13	4.07E+00	+	4.50E-02
regulation of steroid hormone biosynthetic process (GO:0090030)	17	3	1.25E-01	+	5.15E-02
regulation of ossification (GO:0030278)	174	7	1.28E+00	+	5.98E-02
response to ammonium ion (GO:0060359)	44	4	3.24E-01	+	6.05E-02
positive regulation of hydrolase activity	502	12	3.70E+00	+	6.71E-02

(GO:0051345)					
lung growth (GO:0060437)	4	2	2.95E-02	+	7.44E-02
single-organism developmental process (GO:0044767)	4310	50	3.17E+01	+	7.59E-02
cell adhesion (GO:0007155)	665	14	4.90E+00	+	7.86E-02
regulation of phosphate metabolic process (GO:0019220)	1549	24	1.14E+01	+	7.92E-02
developmental process (GO:0032502)	4321	50	3.18E+01	+	8.07E-02
single-organism transport (GO:0044765)	2246	31	1.65E+01	+	8.11E-02
regulation of signaling (GO:0023051)	2349	32	1.73E+01	+	8.12E-02
regulation of phosphorus metabolic process (GO:0051174)	1554	24	1.14E+01	+	8.29E-02
biological adhesion (GO:0022610)	673	14	4.96E+00	+	8.83E-02
regulation of cell differentiation (GO:0045595)	1295	21	9.53E+00	+	1.04E-01
bone mineralization involved in bone maturation (GO:0035630)	5	2	3.68E-02	+	1.16E-01
locomotory behavior (GO:0007626)	195	7	1.44E+00	+	1.17E-01
positive regulation of epithelial cell proliferation (GO:0050679)	142	6	1.05E+00	+	1.24E-01
neurotransmitter transport (GO:0006836)	94	5	6.92E-01	+	1.26E-01
detection of stimulus (GO:0051606)	1259	1	9.27E+00	-	1.37E-01
ion transport (GO:0006811)	1049	18	7.72E+00	+	1.38E-01
regulation of cell development (GO:0060284)	707	14	5.21E+00	+	1.42E-01

membrane depolarization (GO:0051899)	98	5	7.22E-01	+	1.51E-01
positive regulation of positive chemotaxis (GO:0050927)	25	3	1.84E-01	+	1.57E-01
regulation of hormone biosynthetic process (GO:0046885)	25	3	1.84E-01	+	1.57E-01
positive regulation of osteoblast differentiation (GO:0045669)	58	4	4.27E-01	+	1.69E-01
cellular metabolic process (GO:0044237)	6803	32	5.01E+01	-	1.75E-01
regulation of positive chemotaxis (GO:0050926)	26	3	1.91E-01	+	1.76E-01
cellular nitrogen compound metabolic process (GO:0034641)	3845	14	2.83E+01	-	1.90E-01
sensory organ development (GO:0007423)	490	11	3.61E+00	+	1.94E-01

GO ANALYSIS: UPREGULATED: MOLECULAR FUNCTION

Term	Background frequency	Sample frequency	Expected	+/-	P-value
calcium ion binding (GO:0005509)	525	19	3.87E+00	+	1.09E-06
ion channel activity (GO:0005216)	368	11	2.71E+00	+	7.32E-03
substrate-specific channel activity (GO:0022838)	379	11	2.79E+00	+	9.44E-03
passive transmembrane transporter activity (GO:0022803)	396	11	2.92E+00	+	1.38E-02

channel activity (GO:0015267)	396	11	2.92E+00	+	1.38E-02
low voltage-gated calcium channel activity (GO:0008332)	3	2	2.21E-02	+	1.72E-02
cation binding (GO:0043169)	3686	45	2.71E+01	+	2.21E-02
substrate-specific transporter activity (GO:0022892)	887	17	6.53E+00	+	2.33E-02
transporter activity (GO:0005215)	1062	19	7.82E+00	+	2.42E-02
ion transmembrane transporter activity (GO:0015075)	731	15	5.38E+00	+	2.62E-02
gated channel activity (GO:0022836)	303	9	2.23E+00	+	3.28E-02
substrate-specific transmembrane transporter activity (GO:0022891)	778	15	5.73E+00	+	4.96E-02
metal ion binding (GO:0046872)	3606	43	2.66E+01	+	5.19E-02
growth factor activity (GO:0008083)	144	6	1.06E+00	+	5.43E-02
calcium channel activity (GO:0005262)	99	5	7.29E-01	+	6.47E-02
catalytic activity (GO:0003824)	5232	22	3.85E+01	-	6.67E-02
Ras guanyl-nucleotide exchange factor activity (GO:0005088)	106	5	7.80E-01	+	8.74E-02
BMP receptor binding (GO:0070700)	7	2	5.15E-02	+	9.19E-02
transmembrane transporter activity (GO:0022857)	852	15	6.27E+00	+	1.22E-01
extracellular ligand-gated ion channel activity (GO:0005230)	68	4	5.01E-01	+	1.23E-01
calcium ion transmembrane transporter activity (GO:0015085)	116	5	8.54E-01	+	1.29E-01
ligand-gated channel activity (GO:0022834)	131	5	9.65E-01	+	2.18E-01

ligand-gated ion channel activity (GO:0015276)	131	5	9.65E-01	+	2.18E-01
voltage-gated calcium channel activity (GO:0005245)	39	3	2.87E-01	+	2.26E-01
chloride transmembrane transporter activity (GO:0015108)	82	4	6.04E-01	+	2.41E-01
glutamate receptor binding (GO:0035254)	40	3	2.95E-01	+	2.43E-01

GO ANALYSIS: UPREGULATED: CELLULAR COMPONENT

Term	Background frequency	Sample frequency	Expected	+/-	P-value
synapse part (GO:0044456)	438	21	3.23E+00	+	1.10E-09
synapse (GO:0045202)	633	24	4.66E+00	+	4.28E-09
neuron part (GO:0097458)	1059	28	7.80E+00	+	3.10E-07
cell junction (GO:0030054)	868	24	6.39E+00	+	1.96E-06
synaptic membrane (GO:0097060)	243	13	1.79E+00	+	2.75E-06
postsynaptic membrane (GO:0045211)	205	11	1.51E+00	+	3.04E-05
somatodendritic compartment (GO:0036477)	666	19	4.90E+00	+	3.86E-05
neuron projection (GO:0043005)	895	22	6.59E+00	+	5.60E-05
membrane part (GO:0044425)	6702	79	4.93E+01	+	6.02E-05
intrinsic component of membrane (GO:0031224)	5910	70	4.35E+01	+	3.80E-04
cell projection (GO:0042995)	1655	29	1.22E+01	+	7.73E-04

neuronal cell body (GO:0043025)	470	14	3.46E+00	+	7.94E-04
membrane (GO:0016020)	8948	93	6.59E+01	+	9.37E-04
nucleus (GO:0005634)	5735	20	4.22E+01	-	1.05E-03
dendrite (GO:0030425)	431	13	3.17E+00	+	1.45E-03
integral component of membrane (GO:0016021)	5773	67	4.25E+01	+	1.45E-03
cell body (GO:0044297)	530	14	3.90E+00	+	2.92E-03
plasma membrane part (GO:0044459)	1786	29	1.32E+01	+	3.12E-03
cell periphery (GO:0071944)	4996	59	3.68E+01	+	3.79E-03
plasma membrane (GO:0005886)	4895	58	3.60E+01	+	4.14E-03
ion channel complex (GO:0034702)	235	9	1.73E+00	+	4.73E-03
transmembrane transporter complex (GO:1902495)	251	9	1.85E+00	+	7.75E-03
transporter complex (GO:1990351)	254	9	1.87E+00	+	8.47E-03
dendritic spine (GO:0043197)	109	6	8.03E-01	+	1.17E-02
integral component of plasma membrane (GO:0005887)	762	16	5.61E+00	+	1.20E-02
neuron spine (GO:0044309)	113	6	8.32E-01	+	1.42E-02
cellular_component (GO:0005575)	20914	163	1.54E+02	+	2.53E-02
intrinsic component of plasma membrane (GO:0031226)	818	16	6.02E+00	+	2.62E-02
postsynaptic density (GO:0014069)	130	6	9.57E-01	+	2.97E-02
nuclear part (GO:0044428)	1835	3	1.35E+01	-	3.26E-02
ionotropic glutamate receptor complex (GO:0008328)	50	4	3.68E-01	+	3.71E-02
cell projection membrane	203	7	1.50E+00	+	5.61E-02

(GO:0031253)					
nuclear lumen (GO:0031981)	1370	2	1.01E+01	-	1.40E-01
synaptic vesicle (GO:0008021)	122	5	8.98E-01	+	1.50E-01
cell projection part (GO:0044463)	739	13	5.44E+00	+	2.30E-01

Chapter 3: Manuscript in press (*European Journal of Neuroscience*)

"Parallel pathways from motor and somatosensory cortex for controlling whisker movements in mice."

Abstract

Primary somatosensory barrel cortex (S1) plays an important role in representing and processing tactile inputs from the whiskers. Besides sensory processing, S1 also has a role in motor control, wherein it drives retraction of the contralateral whisker (Matyas et al., 2010). Primary whisker motor cortex (M1), on the other hand, drives a second distinct motor program, which closely resembles exploratory whisking. However, the synaptic signaling pathways that control these different motor programs are unknown. In this study, we propose, that these programs are driven via distinct subnuclei in the brainstem. Having confirmed the motor programs driven by S1 and M1 using ChR2 optogenetics, we used a combination of anterograde tracing from the cortex and Rabies-based retrograde tracing from the whisker pad to map the pathway from cortex to the motor neurons in the facial nucleus. The major innervation target of S1 was the spinal trigeminal nucleus (SpV), while M1 preferentially innervated the medially lying reticular formation (RF). Retrograde rabies tracing from identified whisker pad muscles revealed an ordered topography of motor neurons in the facial nucleus with the extrinsic nasolabialis (retractor muscle) motor neurons lying dorsal to the intrinsic follicular (protractor muscle) motor neurons. Transynaptic rabies tracing from the same muscles revealed a major hotspot of extrinsic muscle premotor neurons in SpV interpolaris (SpVi) and a second hotspot lying in the ventral region of the RF. The intrinsic muscle premotor neurons were concentrated in the intermediate reticular formation (iRF) and none were found in SpVi. Our data are consistent with the hypothesis that activity in S1 drives contralateral whisker retraction via SpVi, whereas activity in M1 evokes exploratory whisking via iRF.

Author contribution statement: I contributed to the design of the study, performed all the anterograde and retrograde tracings and characterization of the cells (Fig. 2, 3, 4, 6, 7) and contributed to preparing the manuscript.

European Journal of Neuroscience – Neurosystems
Revision of: EJN-2014-07-21893
6th October 2014

Parallel pathways from motor and somatosensory cortex for controlling whisker movements in mice

Varun Sreenivasan[1=], Kajari Karmakar[2,3=], Filippo M. Rijli[2,3] and Carl C.H. Petersen[1]

[1]Laboratory of Sensory Processing, Brain Mind Institute, Faculty of Life Sciences, École Polytechnique Fédérale de Lausanne (EPFL), Lausanne, Switzerland.

[2]Friedrich Miescher Institute for Biomedical Research, Basel, Switzerland.

[3]University of Basel, Basel, Switzerland.

[=]**The first two authors contributed equally to this study.**

Correspondence to be addressed to:

Carl Petersen,
Laboratory of Sensory Processing,
Brain Mind Institute, Faculty of Life Sciences,
École Polytechnique Fédérale de Lausanne (EPFL),
CH-1015 Lausanne, Switzerland.

Telephone: ++41 21 693 1721
Fax: ++41 21 693 8353
E-mail: carl.petersen@epfl.ch

Filippo M. Rijli,
Friedrich Miescher Institute for Biomedical Research,
Maulbeerstrasse 66,
CH-4058 Basel, Switzerland.

Telephone: ++41 61 696 0436
Fax: ++41 61 697 3976
E-mail: filippo.rijli@fmi.ch

Running Title: Parallel pathways for whisker motor control
Keywords: optogenetics, rabies virus, sensorimotor cortex, premotor neurons, facial motor neurons
No. of text pages: 26 No. of figures: 7
No. of words: 8,967 (Manuscript total), 213 (Abstract) and 495 (Introduction)

Abstract

Mice can gather tactile sensory information by actively moving their whiskers to palpate objects in their immediate surroundings. Whisker sensory perception therefore requires integration of sensory and motor information, which occurs prominently in the neocortex. The signaling pathways from the neocortex for controlling whisker movements are currently poorly understood in mice. Here, we delineate two pathways, one originating from primary whisker somatosensory cortex (wS1) and the other from whisker motor cortex (wM1) that control qualitatively distinct movements of contralateral whiskers. Optogenetic stimulation of wS1 drove retraction of contralateral whiskers, while stimulation of wM1 drove rhythmic whisker protraction. To map brainstem pathways connecting these cortical areas to whisker motor neurons, we used a combination of anterograde tracing using adenoassociated virus injected into neocortex and retrograde tracing using monosynaptic rabies virus injected into whisker muscles. Our data are consistent with wS1 driving whisker retraction by exciting glutamatergic premotor neurons in the rostral spinal trigeminal interpolaris nucleus, that in turn activate the motor neurons innervating the extrinsic retractor muscle *nasolabialis*. The rhythmic whisker protraction evoked by wM1 stimulation might be driven by excitation of excitatory and inhibitory premotor neurons in the brainstem reticular formation innervating both intrinsic and extrinsic muscles. Our data therefore begin to unravel the neuronal circuits linking the neocortex to whisker motor neurons.

Introduction

Mice actively explore their environment using their mystacial whiskers, which they move back-and-forth at high frequencies (5-20 Hz) to scan the immediate space surrounding their snouts. When a moving whisker encounters an object, the whisker bends, which exerts force at its base, driving action potentials in mechanosensitive primary sensory neurons of the trigeminal ganglion. These sensory neurons release glutamate onto postsynaptic neurons in trigeminal brainstem nuclei, from which multiple parallel sensory pathways emerge providing whisker-related tactile sensory information to other brainstem circuits, cerebellar circuits, superior colliculus and the

thalamocortical system (Petersen, 2007; Diamond *et al.*, 2008; Bosman *et al.*, 2011). To generate a coherent percept of the environment, the actively acquired sensory information must be processed in the context of motor commands, e.g. to localize an object the mouse must know where the whisker was at the time of whisker-object contact (Curtis & Kleinfeld, 2009). Conversely, sensory signals affect the motor commands controlling whisker movement, e.g. mice rapidly change whisking patterns upon active touch, presumably to enhance information flow (Mitchinson *et al.*, 2007; Crochet *et al.*, 2011). Understanding whisker tactile sensory perception therefore requires the investigation of the interactions between sensory and motor systems (Kleinfeld & Deschenes, 2011). Whereas the pathways for processing whisker sensory information have been the subject of intense investigation, much less is known about the pathways involved in whisker motor control.

The whiskers are moved by both intrinsic muscles (which are entirely located within the mystacial whisker pad) and extrinsic muscles (which attach to the mystacial pad but are anchored externally) (Dörfl, 1982; Haidarliu *et al.*, 2010). Each intrinsic muscle forms a sling around an individual whisker, which upon contraction causes the whisker to protract, pivoting around the whisker insertion point in the pad. The rhythmic contraction of intrinsic muscles is thought to be the most important process underlying exploratory whisking (Berg & Kleinfeld, 2003). On the other hand, the extrinsic muscles move the whole whisker pad and are thought to play an important role during whisker retraction (Berg & Kleinfeld, 2003). Intrinsic and extrinsic muscles are both under control of motor neurons located in the lateral facial nucleus (Klein & Rhoades, 1985; Herfst & Brecht, 2008). Classical retrograde and anterograde tracing revealed a large number of brain regions projecting to (or near to) the lateral facial nucleus (Hattox *et al.*, 2002). To specifically label premotor neurons, genetically engineered monosynaptic rabies virus (Wickersham *et al.*, 2007) lacking the glycoprotein G can be injected into muscle to infect motor neurons expressing rabies G (Stepien *et al.*, 2010). The rabies virus in the motor neurons is thus trans-complemented and can cross one synapse to infect premotor neurons. A previous study mapped the premotor neurons for whisker muscles using rabies virus expressing fluorescent proteins (Takatoh *et al.*, 2013). Here, we extend these previous findings by analyzing the overlap of cortical projections with whisker premotor neurons, revealing distinct

circuits for controlling different whisker movements originating from wM1 and wS1 (Matyas *et al.*, 2010; Petersen, 2014).

Materials and methods

All experiments were performed in accordance with the Swiss Federal Veterinary Office, under authorization 1628 issued by the 'Service de la consommation et des affaires vétérinaires' of the 'Canton de Vaud'.

ChR2 virus injection

Adult (6-9 week old) male and female Emx1-Cre mice (B6.Cg-Emx1$^{tm1\ (Cre)Krj/J}$ (RRID: IMSR_JAX:005628); Cre recombinase expressed from the endogenous Emx1 locus) were deeply anesthetized with isoflurane and the body temperature was maintained at 36°C by a heating pad. The skull was exposed and the periosteum was removed by gently scraping with a scalpel. The skull was then cleaned with Betadine. A light-weight metal head-post was fixed to the right hemisphere with cyano-acrylate glue (Henkel). A thin layer of glue was also applied over the left hemisphere to protect the skull. A chamber was made by building a wall with dental cement (Paladur) along the edge of the bone covering the left hemisphere. Dental cement was also used to reinforce the attachment of the head-post. Intrinsic signal optical imaging was carried out to map the position of the C2 barrel column in wS1. All whiskers except C2 were trimmed and the chamber over the left hemisphere was filled with warm Ringer's solution and covered with a glass cover slip. The whisker was deflected at 10 Hz for 4 s with a piezo actuator and the resulting intrinsic signal response was imaged under 630 nm illumination by a CMOS camera (Photon Focus) (Grinvald *et al.*, 1986). The images were processed by custom routines written in LabView. To express ChR2 in excitatory neurons, we used an AAV2/5 virus expressing double-floxed humanized ChR2 (histidine 134 converted to arginine) fused to EYFP under the control of the EF1α promoter (AAV2/5.DIO.EF1α.hChR2(H134R).EYFP virus made by Penn Vector Core). Injections were targeted either to the C2 barrel column (identified through intrinsic signal optical imaging) or to wM1 at the stereotaxic co-ordinate 1 mm anterior and 1 mm lateral to Bregma. A large craniotomy (approximately 3 mm in diameter) was made over wS1 or wM1. The dura was left intact. An injection pipette (internal tip

diameter ~20 μm) was tip-filled with the virus solution and lowered into the brain. Injections (~350 nl each) were carried out at two different depths (300 μm and 700 μm below the pia) to infect cells in both supra- and infra-granular layers of the neocortex. The pipette was allowed to remain in the brain for 5 minutes before being retracted slowly over a period of 8-10 minutes to prevent backflow of the virus along the shaft. A cranial window was made with a circular cover slip (4 mm diameter) that was gently placed over the craniotomy. The edges were sealed with cyano-acrylate glue and dental cement (Matyas *et al.*, 2010). Three to four weeks after injection, the cranial window was assessed for YFP fluorescence using an epifluorescence microscope.

Optogenetic stimulation

For the optogenetic stimulus, we used a multimode fiber-optic cable (Thorlabs; NA 0.37; 400 μm) coupled to a 473 nm blue LED (Luxeon Rebel). The outer cladding of one end of the cable was stripped and this end was glued to the LED and reinforced with epoxy and dental cement. The other end of the fiber was also stripped and mounted on a manipulator (Luigs and Neumann), and was lowered on to the cortical surface until the tip of the fiber-optic cable touched the cranial window. The light stimulus consisted of trains of 5 ms light flashes delivered at 50 Hz (25 pulses) or single 5 ms light flashes. The light power was approximately 10 mW.

Quantification of whisker movement

The contralateral C2 whisker was filmed at 500 Hz with a high-speed camera (Redlake). Before applying the optogenetic stimulus, a 600 ms baseline period was recorded. All trials where the whisker was moving during this baseline period were discarded. Whisker angle was quantified using custom routines written in IgorPro (Wavemetrics). Power spectral density (PSD) of whisker movements upon 50 Hz blue light stimulation was calculated on a 200 ms time window before the offset of the light stimulus. The PSD was computed by squaring the amplitude spectrum, and then dividing by two times the bin size. The 5 – 20 Hz band (whisking band) power was calculated by integrating the PSD over 5 – 20 Hz.

Rabies virus injection in the whisker pad

The SAD-ΔG-Rabies:EGFP or SAD-ΔG-Rabies:mCherry viruses were produced in B7GG (BHK-B19G2) cells expressing glycoprotein for complementation as described previously (Wickersham et al., 2010) (DNA kindly provided by E. Callaway and virus kindly provided by B. Roska). Wild-type mice (male and female) at postnatal day 6 (P6) were anesthetized by hypothermia by keeping them on ice for 5 minutes prior to injection. For retrograde tracing of the extrinsic and intrinsic motor neurons in the same animal, one of the SAD-ΔG-Rabies viruses was injected selectively into the extrinsic *nasolabialis* muscle (caudal end) and the other was injected into the intrinsic follicular muscle (C2 whisker follicle) on the right side. The volume of virus (titer: $2x10^6$ transducing units/µl) injected into both muscles was 1.5 µl. The animals were perfused with 4% PFA at P8. In a different set of experiments, to confirm the cholinergic identity of labeled motor neurons, 1.5 µl of SAD-ΔG-Rabies:EGFP was injected into either the extrinsic or intrinsic muscle of ChAT-Cre x (LoxP-Stop-LoxP)-tdTomato animals (B6;129S6-*ChAT*$^{tm1(cre)Lowl}$/J (RRID: IMSR_JAX: 006410) x B6;129S6-Gt(ROSA)26Sor$^{tm9(CAG\text{-}tdTomato)Hze}$/J (RRID: IMSR_JAX: 007908) Jackson Laboratory). For the trans-synaptic labeling experiments, SAD-ΔG-Rabies was mixed with Herpes Simplex Virus 1-Glycoprotein (HSV1-G) virus (volume ratio of HSV: Rabies; 1:2; 1.5 µl of mixture) (Biovex) (Yonehara *et al.*, 2011), a replication-defective virus engineered to express rabies glycoprotein for complementation. The SAD-ΔG-Rabies plus HSV1-G mix was injected at P6 into intrinsic or extrinsic muscles and the animals were sacrificed at P11.

In some experiments, SAD-ΔG-Rabies injections in the whisker pad were coupled with anterograde tracing of cortical axons. An AAV vector encoding EGFP under the control of the synapsin promoter was used (AAV2/1.hSynapsin.EGFP.WPRE.bGH virus made by Penn Vector Core). 200-500 nl of the virus was injected stereotaxically into either wS1 (1.5 mm posterior and 2.5 – 3 mm lateral to Bregma) or wM1 (1 mm anterior and 1 mm lateral to Bregma) of P5 pups (left cortical hemisphere). SAD-ΔG-Rabies:mCherry and HSV1-G were injected unilaterally into the right whisker pad of P6 animals. The animals were sacrificed at P11.

In situ hybridization and immunohistochemistry

Animals were perfused with 4% PFA. For cryostat sections, the tissue was cryoprotected in 10% sucrose (Fluka) (diluted in PBS) and embedded in a solution containing 7.5% gelatin (Sigma) and 10% sucrose in PBS before being frozen at -80°C. Coronal cryostat sections (30 μm) were cut. *In situ* hybridization against digoxigenin labeled antisense RNA probes of *Gad67* (Allen Brain Atlas, Gad1-RP_040324_01_F01) or *Vglut2* (Allen Brain Atlas, Slc17a6-RP_050921_01_E03) was carried out as described in the Perkin Elmer, TSA Plus fluorescence kit manual. The RNA probes were prepared by polymerase chain reaction amplification of mouse cDNA using primers for Gad67 (Forward: TGT GCC CAA ACT GGT CCT; Reverse: TGG CCG ATG ATT CTG GTT) and Vglut2 (Forward: CCA AAT CTT ACG GTG CTA CCTC; Reverse: TAG CCA TCT TTC CTG TTC CACT). The template cDNA was synthesized from total RNA extracted from E14.5 mouse brains. The amplicons were then cloned into pCRII-TOPO vector using a TOPO TA cloning kit (Life Tehnologies). The cloned plasmids were linearized by *XhoI* restriction digestion and the antisense probes were transcribed using the Sp6 RNA polymerase (Promega). For the *in situ* hybridization, the cryostat sections were post-fixed in 4% PFA in PBS. After washing in PBS, the sections were incubated overnight at 68°C in a probe solution (diluted in hybridization buffer, 1:100) in a humid chamber. Following hybridization and washing, the sections were blocked with 2% blocking reagent (Roche) for 1.5 hours at room temperature and then incubated overnight at 4°C with anti-digoxigenin antibody conjugated to horseradish peroxidase (1:100, Roche Applied Science, Cat# 11207733910, RRID: AB_514500). After washing, the *in situ* signal was developed with TSA Plus fluorescein kit (Perkin Elmer). Following the revelation of the *in situ* signals, the sections were washed in PBS and then blocked with 5% bovine serum albumin in PBS for 1.5 hours at room temperature. The sections were then incubated with rabbit anti-RFP antibody (1:200, Rockland Immunochemicals Inc., Cat# 600-401-379, RRID: AB_2209751) overnight at 4°C. Finally, they were rinsed and incubated with donkey anti-rabbit Alexa 568 (1:200, Life Technologies, Cat# A10042, RRID: AB_11180183) for 2 hours at room temperature.

Alignment of brainstem slices with schematic maps

Individual coronal brainstem sections were manually overlaid with the corresponding map from the Paxinos and Franklin Mouse Brain Atlas, 2001. The autofluorescence of the brainstem enables the spinal trigeminal tract, the inferior cerebellar peduncle, the medial longitudinal fasciculus and the pyramidal tract to be clearly visible. Other landmarks included the midline, the fourth ventricle and the central canal. Care was taken to ensure that all the landmarks on the sections were aligned with the map. The boundaries of the brainstem nuclei were taken to be at the positions marked on the map.

Whisker pad anatomy

Animals that were injected with SAD-ΔG-Rabies into the extrinsic *nasolabialis* muscle or the intrinsic follicular muscle (C2 whisker follicle), were transcardially perfused with 4% PFA in PBS. The heads were collected and were post-fixed in 4% PFA in PBS at 4°C overnight. They were then transferred to 20% sucrose in PBS solution for 2 days, following which they were embedded in OCT compound (Tissue-Tek, Pimos) and allowed to freeze on dry ice. Sagittal sections of 50 µm thickness were made using a cryostat.

Statistical analysis

All data are presented as mean ± SEM. Normality of data distributions was assessed using the Anderson-Darling normality test. For normally distributed data, statistical significance was assessed with Student's t-test for paired or unpaired observations. For non-normally distributed data, statistical significance was assessed with Wilcoxon's rank sum test (unpaired observations) and signed rank test (paired observations).

Results

wS1 and wM1 drive antagonistic movements of the contralateral whisker

Our first goal was to characterize the differences in whisker movements driven by wS1 and wM1 (Haiss & Schwarz, 2005; Petersen, 2007; Matyas *et al.*, 2010; Petersen, 2014). To this end, we expressed a Cre-dependent Channelrhodopsin-2 (ChR2) virus in wS1 and wM1 of Emx1-Cre mice. In these mice, the expression of Cre recombinase is restricted to excitatory neurons of the neocortex (Chan *et al.*, 2001). Stimulation of wS1

with a 50 Hz light train caused a sustained retraction of the contralateral whisker, whereas stimulation of wM1 with a 50 Hz light train caused a rhythmic protraction of the contralateral whisker (wS1: -7.3 ± 1.1 degrees, n = 10 mice; wM1: 6.0 ± 0.9 degrees, n = 8 mice; $p = 10^{-7}$, Student's t-test for unpaired observations) (Figures 1A-1C) (Matyas *et al.*, 2010). The latencies of wS1 and wM1 driven movements were not significantly different (wS1: 23.2 ± 6.6 ms, n = 10 mice; wM1: 36.5 ± 5.5 ms, n = 8 mice; p = 0.1, Wilcoxon's rank-sum test) (Figure 1C). The rhythmicity of the movements were significantly different with wS1 driving a non-rhythmic whisker movement and wM1 driving a rhythmic whisker movement (5-20 Hz power for wS1: 5.1 ± 1.8 deg^2, n = 10 mice; 5-20 Hz power for wM1: 32.5 ± 6.6 deg^2, n = 8 mice; $p = 1.8 \times 10^{-4}$, Wilcoxon's rank-sum test) (Figure 1D).

Long stimulus trains have been shown to elicit complex movements that may involve the recruitment of other cortical areas and complex motor circuits (Graziano *et al.*, 2002; Harrison *et al.*, 2012). We therefore repeated the experiments with single brief light pulses. A single 5-ms light flash delivered to wS1 robustly evoked a small retraction of the contralateral whisker, following which the animal initiated whisking, while a 5-ms light flash delivered to wM1 caused a small protraction (wS1: -1.4 ± 0.4 degrees, n = 6 mice; wM1: 1.9 ± 0.4 degrees, n = 5 mice; $p = 10^{-4}$, Student's t-test for unpaired observations) (Figures 1E and 1F). The latencies of the whisker movements evoked by single 5-ms light flashes delivered to wS1 and wM1 were not significantly different (wS1: 14 ± 1 ms, n = 6 mice; wM1: 34.4 ± 5.7 ms, n = 5 mice; p = 0.06, Wilcoxon's rank-sum test) (Figure 1F). Thus, wS1 and wM1 drive qualitatively distinct types of whisker movements, with wS1 driving a sustained backward movement and wM1 driving a rhythmic forward movement.

Whisker motor neurons in the lateral facial nucleus

In order to understand how wS1 and wM1 cortex can drive whisker movements, we investigated the anatomical pathways involved in generating whisker motion. We began by studying the motor neurons that control forward and backward movements of the whisker. We focused our attention on the upper extrinsic muscle *nasolabialis* and the intrinsic muscles of the whisker pad. *Nasolabialis* is anchored outside the pad and extends between the vibrissa rows where it attaches superficially under the skin (Dorfl,

1982; Berg & Kleinfeld, 2003). Contraction of this muscle results in a posterior translation of the entire whisker pad, thus driving retraction of the individual whiskers. On the other hand, the intrinsic follicular muscles are located entirely within the whisker pad. Each intrinsic muscle wraps around the base of a whisker follicle to form a sling and is superficially attached to the skin surrounding the whisker that is immediately posterior. Contraction of the intrinsic muscle causes the base of the follicle to move posteriorly thereby causing the whisker to pivot and protract (Dorfl, 1982; Berg & Kleinfeld, 2003). In order to retrogradely trace the location of the motor neurons, we injected the glycoprotein-deleted rabies (Rabies-ΔG) (Wickersham *et al.*, 2007) encoding EGFP or mCherry into muscle of P6 mice and sacrificed them at P8 (Figure 2A). Analysis of the injections sites revealed that the injections were distinct and were localized to the intrinsic follicular muscle within the whisker pad and the extrinsic *nasolabialis* muscle anchored externally, respectively (Figure 2B). The cholinergic identity of the motor neurons was confirmed by injecting Rabies-ΔG-EGFP into either the extrinsic or the intrinsic muscles of ChAT-Cre x LSL-tdTomato mice (which express the red fluorescent protein tdTomato in all cholinergic neurons) (Figures 2C and 2D). Injection of Rabies-ΔG-mCherry into the extrinsic muscle and Rabies-ΔG-EGFP into the intrinsic muscle (or *vice versa*), of the same animal, revealed an ordered distribution of motor neurons in the facial nucleus, where the extrinsic motor neurons were always located dorsally with respect to the intrinsic motor neurons within the lateral facial nucleus (Figures 2E and 2F) (Klein & Rhoades, 1985; Takatoh *et al.*, 2013). No neurons were labeled in other nuclei of the brainstem.

Intrinsic and extrinsic whisker premotor neurons in the brainstem

We were next interested in mapping the brainstem areas containing premotor neurons that synapse onto these distinct motor neuron pools. Rabies-ΔG injected into muscle is retrogradely transported to motor neurons, but the absence of the gene encoding for the glycoprotein renders it incapable of trans-synaptic spread. To allow the trans-synaptic movement of rabies, an additional retrograde virus encoding the rabies glycoprotein can be co-injected into the muscle, which will then trans-complement Rabies-ΔG in the motor neurons resulting in monosynaptic spread (Stepien *et al.*, 2010). To label the

premotor neurons, we injected a Herpes Simplex Virus serotype 1 vector encoding the rabies glycoprotein (HSV1-G) (Yonehara *et al.*, 2011) along with the Rabies-ΔG into extrinsic muscle (Figure 3A), intrinsic muscle (Figure 3A) or both muscles (Figure 4A) of P6 mice and sacrificed them at P11.

We found that the premotor neurons of these two muscles were intermingled in many brainstem areas, with very few double-labelled cells (Figure 4). In agreement with a previous study (Takatoh *et al.*, 2013), we found intermingled premotor neurons for both extrinsic and intrinsic whisker muscles in: spinal trigeminal oralis nucleus (Sp5O) (Figures 3B and 4B); the vestibular nuclei (Ve) (Figures 3B and 4B); the lateral para-gigantocellular nucleus (LPG); Bötzinger/Pre-Bötzinger complexes; intermediate reticular formation (IRt) (Figures 3C and 4C); gigantocellular reticular formation (GIRt); parvocellular reticular formation (PCRt) (Figures 3D and 4D); medullary dorsal reticular formation (MdD) (Figure 3E).

We also found striking differences in the premotor distributions for intrinsic and extrinsic whisker muscles in some brainstem regions. Intrinsic premotor neurons were particularly dense along the mediodorsal to lateroventral axis of the IRt with some cells also located more medially in GIRt. In contrast, extrinsic premotor neurons were dense in the ventrolateral aspect of Sp5Ir, whereas there were very few intrinsic premotor neurons located in Sp5Ir. To quantify, we counted rabies labeled premotor neurons, on the side of the brainstem ipsilateral to the injection, in coronal sections spanning Sp5O until Sp5Ic, and compared the total number of cells counted to the number of cells located in Sp5Ir and IRt for the extrinsic and intrinsic muscles (Figure 3F). The fraction of extrinsic premotor neurons located in Sp5Ir was significantly higher than the fraction of intrinsic premotor neurons located in Sp5Ir (extrinsic fraction in Sp5Ir: 36 ± 12 %, n = 5 mice; intrinsic fraction in Sp5Ir: 8 ± 3 %, n = 5 mice; $p = 0.005$, Student's t-test for unpaired observations). Conversely, the fraction of intrinsic premotor neurons located in IRt was significantly higher than the fraction of extrinsic premotor neurons located in IRt (extrinsic fraction in IRt: 23 ± 6 %, n = 5 mice; intrinsic fraction in IRt: 45 ± 12 %, n = 5 mice; $p = 0.01$, Student's t-test for unpaired observations) (Figure 3F).

In summary, the premotor neurons for intrinsic and extrinsic whisker muscles were distributed in a largely intermingled manner over a large part of the brainstem. However, there were two major differences: IRt was dominated by intrinsic premotor

neurons for controlling whisker protraction, and Sp5Ir was dominated by extrinsic premotor neurons for controlling whisker retraction.

Cortical innervation of the brainstem

Having identified the locations of the motor and premotor neurons for extrinsic and intrinsic whisker muscles, we next investigated the axonal innervation of the brainstem from wS1 and wM1. We injected an AAV virus encoding EGFP into either wS1 or wM1 of adult animals and studied the cortical axons in the contralateral brainstem (Figure 5A). We found very little overlap in the brainstem regions innervated by wS1 and wM1. wS1 projected strongly to ventral Sp5O (Figure 5B); Sp5Ir (Figure 5C); Sp5Ic (Figure 5D) and Sp5C (Figure 5E). wM1 projected strongly to Sp5O, PCRt, GIRt, IRt, MdV and MdD (Figure 5B-5E). wM1 also weakly innervated a dorsal portion of Sp5Ir (Figure 5C). In addition, wM1 projected to the ventrolateral portion of FN. To quantify, we normalized the axon intensity in the spinal trigeminal nucleus (Sp5) and the reticular formation (Rt) to the background fluorescence (Figure 5F). The wS1 innervation of Sp5 was significantly stronger than the innervation of Rt (normalized axon intensity in Sp5: 2.2 ± 0.2; normalized axon intensity in Rt: 1.1 ± 0.04, n = 3 mice; p = 0.03, Student's t-test for paired observations). Conversely, the wM1 innervation of Rt was significantly stronger than the innervation of Sp5 (normalized axon intensity in Sp5: 1.4 ± 0.1; normalized axon intensity in Rt: 1.9 ± 0.3, n = 4 mice; p = 0.03, Student's t-test for paired observations) (Figure 5F). Overall, these data indicated a complementary distribution of wS1 and wM1 axons innervating the brainstem, with wS1 projecting more laterally (spinal trigeminal nuclei) and wM1 projecting more medially (brainstem reticular formation) (Figure 5F).

wS1 axons innervate extrinsic premotor neurons in Sp5Ir

Of the brainstem regions receiving dense wS1 innervation, only the Sp5Ir nucleus contained a major group of premotor neurons, mostly composed of extrinsic premotor neurons and only few intrinsic premotor neurons (Figures 3 and 4). The wS1 axons could therefore innervate extrinsic premotor Sp5Ir neurons.

However, our axonal mapping was carried out in adult mice whereas the retrograde rabies labeling of premotor neurons from muscle injections only works well

in young animals. We therefore injected AAV-EGFP into wS1 and Rabies-ΔG-mCherry + HSV1-G into the contralateral extrinsic muscle of P6 mice and analysed the fixed brains at P11. We found a similar axonal innervation of the brainstem in young as compared to adult mice. Coronal sections confirmed that wS1 axons projected into the Sp5Ir region containing extrinsic premotor neurons (Figure 6A). Imaged at high resolution with confocal microscopy (Figure 6B), we found cortical axons in close apposition with trans-synaptically labeled extrinsic premotor neurons. We counted the number of appositions at the dendrites of these premotor neurons to be 0.07 ± 0.009 appositions/µm of dendrite (11 dendrites from 3 premotor cells in 2 mice). These data indicate that wS1 and Sp5Ir extrinsic premotor neurons are likely to be synaptically connected.

We next investigated the neurotransmitter phenotype of Sp5Ir premotor neurons by *in situ* hybridization for *GAD67* and *Vglut2*. The analysis revealed that the large extrinsic premotor neurons labeled in Sp5Ir were glutamatergic (Figure 6C). A few of the smaller extrinsic premotor neurons were GABAergic (Figure 6C). Since the large glutamatergic extrinsic premotor neurons located in Sp5Ir receive excitatory input from pyramidal neurons of the contralateral wS1, we reason that wS1 → Sp5Ir (extrinsic premotor) → FN (extrinsic motor) constitutes a motor circuit in which stimulation of wS1 could drive retraction of the contralateral whisker (Figure 6D).

wM1 axons innervate the FN and IRt

We were next interested in the motor circuits downstream of wM1. A previous study reported the presence of monosynaptic connections from wM1 onto motor neurons in the FN of the rat (Grinevich *et al.*, 2005). Accordingly, we observed AAV-EGFP-labeled wM1 axons projecting to the ventrolateral aspect of the contralateral FN labeled in ChAT-Cre x LSL-td-Tomato mice (Figure 7A). Furthermore, trans-synaptic rabies tracing from the intrinsic muscle also identified intrinsic premotor neurons in frontal and wM1 cortex (Figure 7B). In contrast, very few cortical neurons were labeled when trans-synaptic rabies virus was injected into extrinsic muscle. Thus, wM1 might contribute to controlling whisker movements by directly synapsing onto the motor neurons innervating intrinsic muscles.

A major innervation site of the wM1 axons in the brainstem was the PCRt (Figure 5D). However, in our rabies tracing experiments, we did not consistently find

premotor cells localized in PCRt and in the cases where we did, they were few in number and did not display any specific distribution or clustering. Furthermore, lesioning the PCRt has little effect upon whisker movements (Moore *et al.*, 2013).

Next we investigated the wM1 projections in the IRt. A whisking central pattern generator in the brainstem has been suggested to be localized in the ventral part of the IRt, lying medial to the nucleus ambiguus (NA) (Moore *et al.*, 2013). Since the NA contains cholinergic neurons, it is easily distinguishable in the ChAT-Cre x LSL-tdTomato animals (Figure 7C). We found that wM1 innervated the region of the IRt near to the NA (Figure 7C*, middle*). This region was a major hotspot of intrinsic premotor neurons (Figure 7C*, right*). To investigate the potential overlap of the wM1 axons with these premotor neurons, we injected AAV-EGFP into wM1 and Rabies-ΔG-mCherry + HSV1-G into the contralateral intrinsic muscle of P6 mice and sacrificed them at P11. Coronal sections showed that in the IRt, the wM1 axons came into close apposition with the trans-synaptically labeled intrinsic premotor neurons (Figure 7D). We counted the number of appositions at the dendrites of these premotor neurons to be 0.06 ± 0.008 appositions/μm of dendrite (11 dendrites from 3 premotor cells in 2 mice). The rabies-labeled population of premotor neurons in the IRt contained both $GAD67^+$ inhibitory neurons, as well as $Vglut2^+$ excitatory neurons (Figure 7E). wM1 might thus innervate both excitatory and inhibitory intrinsic premotor neurons. In addition, the same brainstem region also harbors extrinsic premotor neurons. wM1 innervation of IRt (and surrounding brainstem reticular regions) might thus drive rhythmic whisker protraction through a complex network of inhibitory and excitatory premotor neurons for both intrinsic and extrinsic muscles, which might constitute an oscillatory central pattern generator (Figure 7F) (Moore *et al.*, 2013).

Discussion

To further our understanding of the cortical circuits involved in whisker motor control, we characterized the whisker movements driven by wS1 and wM1. Optogenetic stimulation of wS1 evoked whisker retraction while optogenetic stimulation of wM1 evoked whisker protraction that was rhythmic (Figure 1). We used modified rabies virus to map whisker motor (Figure 2) and premotor (Figures 3 and 4) neurons, and we investigated the axonal projections from wS1 and wM1 to the brainstem using AAV

virus (Figure 5). We examined the regions with the most prominent overlap between cortical axons and premotor neurons finding that wS1 axons strongly overlap with extrinsic premotor neurons located in the Sp5Ir (Figure 6) and that wM1 axons overlap with intrinsic premotor neurons in IRt (Figure 7). In addition we found that wM1 innervates the intrinsic motor neurons in FN (Figure 7). Together our results suggest that wS1 and wM1 control distinct whisker movements through two parallel motor pathways.

Distinct whisker premotor neuron subpopulations for intrinsic and extrinsic muscles

Rabies virus has been used extensively as a retrograde trans-synaptic tracer to map motor circuits in the mammalian brain. Pioneering work used replicating rabies virus to trace motor control circuits across multiple synapses (Ugolini, 1995; Rathelot & Strick, 2006). Monosynaptic inputs can be traced using genetically modified rabies virus (Wickersham *et al.*, 2007) and this approach has recently been applied to map premotor neurons (Stepien *et al.*, 2010; Esposito *et al.*, 2014; Takatoh *et al.*, 2013). Our results investigating the premotor circuits for whisker motor control are in good agreement with a previous study by Takatoh *et al.* (2013). The extrinsic muscle *nasolabialis*, which is involved in retracting the whisker, is innervated by motor neurons located in a more dorsal part of the lateral FN compared to the motor neurons innervating the intrinsic follicular muscles involved in protracting the whisker (Figure 2). The premotor neurons providing input to these distinct motor neuron pools are also largely segregated with very few double-labelled premotor neurons (Figure 4). In some regions of the brainstem (such as Sp5O, LPG and caudal IRt) the premotor neurons for intrinsic and extrinsic muscle are intermingled (Figures 3 and 4). However, in other parts of the brainstem there are large differences in the density of premotor neurons innervating intrinsic and extrinsic muscles. The most prominent differences are in Sp5Ir, which is strongly dominated by extrinsic premotor neurons with very few intrinsic premotor neurons, and IRt, which is dominated by intrinsic premotor neurons (Figures 3 and 4). The rhythmic back-and-forth movements of the whiskers during exploration are largely driven by the intrinsic muscles. The prominence of intrinsic premotor neurons in IRt is consistent with an important role in whisking for this brainstem region, which has been suggested to form the central pattern generator (Moore *et al.*, 2013).

The mechanisms of trans-synaptic spread of rabies virus is unknown and, recently, the specificity of retrograde versus anterograde transport has been called into question (Zampieri *et al.*, 2014). In our experiments, we do not find evidence for anterograde trans-synaptic spread. If the rabies virus was spreading in an anterograde direction, then one would expect to see trans-synaptic labeling of neurons in the sensory trigeminal nuclei via infection of the trigeminal primary sensory neurons. However, we did not find any rabies-labeled neurons in the principal trigeminal (Pr5) nucleus or in the caudal sector of spinal trigeminal interpolaris nucleus (Sp5Ic). Thus, under our experimental conditions, the trans-synaptic labeling of neurons with rabies virus is retrograde and therefore useful for analyzing premotor circuits.

Distinct motor circuits driven from wS1 and wM1

The subcortical axonal projections from wS1 and wM1 follow largely parallel pathways innervating neighboring and largely non-overlapping brain areas (Matyas *et al.*, 2010). In the brainstem we found very little overlap in the regions innervated by wS1 and wM1 (Figure 5). Projections from wS1 almost exclusively innervated the spinal trigeminal nuclei, including a ventral portion of Sp5O, lateral aspects of both rostral and caudal Sp5I and medial Sp5C. In contrast wM1 primarily innervated PCRt, IRt, GIRt, MdV and MdD, while largely avoiding the spinal trigeminal nuclei. These distinct patterns of cortical innervation from wS1 and wM1 are likely to differentially activate the whisker premotor neurons in the brainstem.

To try to define the possible downstream motor circuits activated by cortical stimulation, we examined the overlap in the axonal projections from cortex with the locations of whisker premotor neurons. Because wS1 axons specifically innervate the spinal trigeminal nuclei (Figure 5) and the majority of premotor neurons located in the spinal trigeminal nuclei are from the extrinsic muscle (Figures 3 and 4), we further investigated possible interactions finding close apposition of wS1 axon with extrinsic premotor neurons (Figure 6). This raises the possibility that wS1 drives whisker retraction through a simple circuit wS1 → Sp5Ir (extrinsic premotor) → FN (extrinsic motor) (Figure 6D). In future experiments it will be important to specifically inactivate the neurons in this proposed circuit to test this hypothesis.

Motor circuits in the brainstem downstream of wM1 appear more complex. In part, whisker movements evoked by wM1 might be driven by direct monosynaptic input onto motor neurons in the FN (Grinevich *et al.*, 2005). Indeed, we found axons from wM1 innervating ventrolateral FN, where intrinsic motor neurons are located and we also found monosynaptically-connected premotor neurons in motor and frontal cortex from rabies injections into the intrinsic muscle. However, latencies for whisker movement evoked by wM1 stimulation were not shorter than the latencies for whisker movement evoked by wS1 stimulation. The direct monosynaptic innervation of FN motor neurons by wM1 may therefore not be the most important circuit by which wM1 drives whisker movement. The densest axonal innervation from wM1 was found in PCRt, IRt, GIRt, MdV and MdD, which contain premotor neurons for both intrinsic and extrinsic muscles. The IRt, especially the region medial and dorsal to nucleus ambiguus, contains a very high density of intrinsic premotor neurons (Figures 3D and 4C) and is strongly innervated by wM1 (Figures 5 and 7). Rhythmic whisker protraction driven by stimulation of wM1 might therefore be driven by a circuit wM1 → IRt (intrinsic premotor) → FN (intrinsic motor) (Figure 7F). Specific inactivation of the neurons in this proposed circuit will be critical to test this hypothesis in future experiments.

The movements evoked by wM1 stimulation are also more complex than those evoked by wS1. wM1 not only drives protraction, but also rhythmic whisking (involving both protraction and retraction), whereas wS1 stimulation drives a constant whisker retraction. The greater complexity of the whisker movements evoked by wM1 stimulation may result from activation of more complex central pattern generator circuits in the brainstem, which might also interact with the controllers of other orofacial movements (Moore *et al.*, 2013).

Functional implications and future perspectives

The whisker movements evoked by wS1 and wM1 are qualitatively different and likely serve distinct functional roles during behavior. The whisker retraction driven by wS1 might serve as a useful negative feedback signal, reducing the flow of incoming sensory information. The rhythmic whisker protraction evoked by wM1 stimulation resembles exploratory whisking and is thus likely involved in enhancing the flow of incoming

information. These two different cortical regions thus evoke whisker movements with opposing purposes likely through distinct motor circuits explored in this study. It is unknown if similar antagonistic cortical motor circuits exist in other systems and species.

Motor control by sensory cortex is unusual (Matyas *et al.*, 2010) and it is possible that it is a unique specialization of the whisker system. The intrinsic muscles that drive whisking are also unusual in having no spindles for proprioception, and the motor control by wS1 might then provide valuable sensory input to the whisker motor system. On the other hand motor control by sensory cortex might be of general importance, e.g. premotor neurons have been reported to be found in the macaque primary somatosensory cortex (Rathelot & Strick, 2006). In future experiments it will therefore be important to re-examine cortical motor maps and the possible downstream motor circuits in different species and systems.

Acknowledgments

This work was supported by grants from the Swiss National Science Foundation, the European Research Council, and the Novartis Research Foundation. We thank Ed Callaway for rabies DNA constructs, Botond Roska for rabies viruses, Nathalie Vilain for antisense RNA probes and the EPFL-BIOP for help with imaging. We thank Silvia Arber, Alexandros Kyriakatos, Ferenc Matyas and Celine Mateo for helpful discussions. The authors have no competing interests.

Abbreviations

ChR2, channelrhodopsin-2; FN, facial nucleus; GIRt, gigantocellular reticular formation; IRt, intermediate reticular formation; LPG, lateral para-gigantocellular reticular formation; MdD, medullary dorsal reticular formation, MdV, medullary ventral reticular formation; NA, nucleus ambiguus; PCRt, parvocellular reticular formation; Sp5C, spinal trigeminal nucleus caudalis; Sp5Ic, spinal trigeminal nucleus caudal interpolaris; Sp5Ir, spinal trigeminal nucleus rostral interpolaris; Sp5O, spinal trigeminal nucleus oralis; wM1, whisker motor cortex; wS1, whisker somatosensory cortex; Ve, vestibular nuclei.

References

Berg, R.W. & Kleinfeld, D. (2003) Rhythmic whisking by rat: Retraction as well as protraction of the vibrissa is under active muscular control. *J. Neurophysiol.* **89**, 104-117.

Bosman, L.W., Houweling, A.R., Owens, C.B., Tanke, N., Shevchouk, O.T., Rahmati, N., Teunissen, W.H., Ju, C., Gong, W., Koekkoek, S.K. & De Zeeuw, C.I. (2011) Anatomical pathways involved in generating and sensing rhythmic whisker movements. *Front. Integr. Neurosci.* **5**, 53.

Chan, C.H., Godinho, L.N., Thomaidou, D., Tan, S.S., Gulisano, M. & Parnavelas, J.G. (2001) Emx1 is a marker for pyramidal neurons of the cerebral cortex. *Cereb. Cortex* **11**, 1191-1198.

Crochet, S., Poulet, J.F.A., Kremer, Y. & Petersen, C.C.H. (2011) Synaptic mechanisms underlying sparse coding of active touch. *Neuron* **69**, 1160-1175.

Curtis, J.C. & Kleinfeld, D. (2009) Phase-to-rate transformations encode touch in cortical neurons of a scanning sensorimotor system. *Nat. Neurosci.* **12**, 492-501.

Diamond, M.E., von Heimendahl, M., Knutsen, P.M., Kleinfeld, D. & Ahissar, E. (2008) 'Where' and 'what' in the whisker sensorimotor system. *Nat. Rev. Neurosci.* **9**, 601-612.

Dörfl, J. (1982) The musculature of the mystacial vibrissa of the white mouse. *J. Anat.* **135**, 147-154.

Esposito, M.S., Capelli, P. & Arber, S. (2014) Brainstem nucleus MdV mediates skilled forelimb motor tasks. *Nature* **508**, 351-356.

Graziano, M.S., Taylor, C.S. & Moore, T. (2002) Complex movements evoked by microstimulation of precentral cortex. *Neuron* **34**, 841-851.

Grinevich, V., Brecht, M. & Osten, P. (2005) Monosynaptic pathway from rat vibrissa motor cortex to facial motor neurons revealed by lentivirus based axonal tracing. *J. Neurosci.* **25**, 8250-8258.

Grinvald, A., Lieke, E., Frostig, R.D., Gilbert, C.D. & Wiesel, T.N. (1986) Functional architecture of cortex revealed by optical imaging of intrinsic signals. *Nature* **324**, 361-364.

Haiss, F. & Schwarz, C. (2005) Spatial segregation of different modes of movement control in the whisker representation of rat primary motor cortex. *J. Neurosci.* **25**, 1578-1587.

Haidarliu, S., Simony, E., Golomb, D. & Ahissar, E. (2010) Muscle architecture in the mystacial pad of the rat. *Anat. Rec.* **293**, 1192-1206.

Hattox, A.M., Priest, C.M. & Keller, A. (2002) Functional circuitry involved in the regulation of whisker movements. *J. Comp. Neurol.* **442**, 266-276.

Harrison, T.C., Ayling, O.G. & Murphy, T.H. (2012) Distinct cortical circuit mechanisms for complex forelimb movements and motor map topography. *Neuron* **74**, 397-409.

Herfst, L.J. & Brecht, M. (2008) Whisker movements evoked by stimulation of single motor neurons in the facial nucleus of the rat. *J. Neurophysiol.* **99**, 2821-2832.

Klein, B.G. & Rhoades, R.W. (1985) Representation of whisker follicle intrinsic musculature in the facial motor nucleus of the rat. *J. Comp. Neurol.* **232**, 55-69.

Kleinfeld, D. & Deschênes, M. (2011) Neuronal basis for object location in the vibrissa scanning sensorimotor system. *Neuron* **72**, 455-468.

Matyas, F., Sreenivasan, V., Marbach, F., Wacongne, C., Barsy, B., Mateo, C., Aronoff, R. & Petersen, C.C.H. (2010) Motor control by sensory cortex. *Science* **330**, 1240-1243.

Mitchinson, B., Martin, C.J., Grant, R.A. & Prescott, T.J. (2007) Feedback control in active sensing: rat exploratory whisking is modulated by environmental contact. *Proc. Biol. Sci.* **274**, 1035-1041.

Moore, J.D., Deschênes, M., Furuta, T., Huber, D., Smear, M.C., Demers, M. & Kleinfeld, D. (2013) Hierarchy of orofacial rhythms revealed through whisking and breathing. *Nature* **497**, 205-210.

Paxinos, G. & Franklin, K. (2001) The mouse brain in stereotaxic coordinates. 2nd edition. Academic Press, San Diego.

Petersen, C.C.H. (2007) The functional organization of the barrel cortex. *Neuron* **56**, 339-355.

Petersen, C.C.H. (2014) Cortical control of whisker movement. *Annu. Rev. Neurosci*. **37**, 183-203.

Rathelot, J.A. & Strick, P.L. (2006) Muscle representation in the macaque motor cortex: An anatomical perspective. *Proc. Natl. Acad. Sci. USA* **103**, 8257-8262.

Stepien, A.E., Tripodi, M. & Arber, S. (2010) Monosynaptic rabies virus reveals premotor network organization and synaptic specificity of cholinergic partition cells. *Neuron* **68**, 456-472.

Takatoh, J., Nelson, A., Zhou, X., Bolton, M.M., Ehlers, M.D., Arenkiel, B.R., Mooney, R. & Wang, F. (2013) New modules are added to vibrissal premotor circuitry with the emergence of exploratory whisking. *Neuron* **77**, 346-360.

Ugolini, G. (1995) Specificity of rabies virus as a transneuronal tracer of motor networks: Transfer from hypoglossal motorneurons to connected second-order and higher order central nervous system cell-groups. *J. Comp. Neurol.* **356**, 457-480.

Wickersham, I.R., Lyon, D.C., Barnard, R., Mori, T., Finke, S., Conzelmann, K., Young, J. & Callaway, E.M. (2007) Monosynptic restriction of transsynaptic tracing from single genetically targeted neurons. *Neuron* **53**, 639-647.

Yonehara, K., Balint, K., Noda, M., Nagel, G., Bamberg, E. & Roska, B. (2011) Spatially asymmetric reorganization of inhibition establishes a motion sensitive circuit. *Nature* **469**, 407-410.

Zampieri, N., Jessell, T.M. & Murray, A.J. (2014) Mapping sensory circuits by anterograde transsynaptic transfer of recombinant rabies virus. *Neuron* **81**, 766-778.

Figure Legends

Figure 1. Movements of the contralateral whisker driven by wS1 and wM1. (A) Widefield image of a fixed brain where ChR2-expressing virus had been injected into wS1 (*top left*). 50 Hz blue light stimulation of wS1 drove retraction of the contralateral whisker (*bottom left*). Coronal section showing the injection site localized to wS1 (*right*). (B) Widefield image of a fixed brain where ChR2-expressing virus had been injected into wM1 (*top left*). 50 Hz blue light stimulation of wM1 drove rhythmic protraction of the contralateral whisker (*bottom left*). Coronal section showing the injection site localized to wM1 (*right*). Coronal sections in panels A and B were counter-stained with DAPI**.** (C) Quantification of whisker movement amplitudes (*above*) and movement latencies (*below*) for the 50 Hz stimulus delivered to wS1 and wM1. The amplitude of the evoked movement was significantly different (n = 10 mice for wS1; n = 8 mice for wM1; $p = 10^{-7}$). The latency of the evoked movement was not significantly different (n = 10 mice for wS1; n = 8 mice for wM1; p = 0.1). (D) Power spectral density (PSD) of the wS1 and wM1 driven whisker movements upon 50 Hz blue light stimulation (*above).* The PSD was calculated on a 200 ms time window before the offset of the light stimulus. The 5-20 Hz band (whisking band) power was significantly higher for wM1 compared to wS1 (*below*), indicating that wM1-evoked movement is more rhythmic than wS1-evoked movement (n = 10 mice for wS1; n = 8 mice for wM1; $p = 1.8 \times 10^{-4}$). Light traces are for individual mice. Dark traces show grand average spectra. (E) A single 5 ms blue light pulse delivered to wS1 drove a small but robust retraction of the contralateral whisker (*above*) while a 5 ms blue light pulse delivered to wM1 drove a small but robust protraction of the contralateral whisker (*below*). Lighter traces indicate single trials while darker traces indicate the average for the mouse. (F) Quantification of whisker movement amplitudes (*above*) and movement latencies (*below*) for the single 5 ms stimulus delivered to wS1 and wM1. The amplitude of the evoked movement was significantly different (n = 6 mice for wS1; n = 5 mice for wM1; $p = 10^{-4}$). The latency of the evoked movement was not significantly different (n = 6 mice for wS1; n = 5 mice for wM1; p = 0.06).

Figure 2. The facial nucleus contains two distinct whisker motor neuron populations that drive antagonistic muscles. (A) Schematic showing the strategy used to label the motor neurons in the facial nucleus. Two different glycoprotein deleted Rabies viruses (Rabies-ΔG) encoding EGFP and mCherry were injected unilaterally into the right follicular (intrinsic protractor) and right *nasolabialis* (extrinsic retractor) muscles. (B) Sagittal section of the whisker pad where Rabies-ΔG was targeted to the *nasolabialis* muscle (*top*) and the C2 follicular muscle (*bottom*). The top and bottom panels are from different animals. The pad has been counterstained with DAPI. (C) Cholinergic identity of the rabies-labeled extrinsic motor neurons was confirmed by injecting Rabies-ΔG-EGFP in the extrinsic muscle of ChAT-Cre x LSL-tdTomato animals. Double labeled extrinsic motor neurons were present in the dorsal aspect of the lateral facial nucleus. (D) Cholinergic identity of the rabies labeled intrinsic motor neurons was confirmed by injecting Rabies-ΔG-EGFP in the intrinsic muscle of ChAT-Cre x LSL-tdTomato animals. Double labeled intrinsic motor neurons were present in the ventral aspect of the lateral facial nucleus. (E) Coronal section through the ipsilateral brainstem at the level of the facial nucleus (FN) from an animal that received Rabies-ΔG-EGFP in the intrinsic muscle and Rabies-ΔG-mCherry in the extrinsic muscle. The red cells are the motor neurons of the extrinsic muscle while the green cells are the motor neurons of the intrinsic muscle. The coronal section is overlaid with a schematic drawing (Paxinos & Franklin, 2001). (F) Group data from 7 animals that were injected with Rabies-ΔG of one colour in the extrinsic muscle and Rabies-ΔG of the other colour in the intrinsic muscle. Red circles indicate the positions of the extrinsic *nasolabialis* muscle motor neurons, while green circles indicate the positions of the intrinsic follicular muscle motor neurons in the FN. The motor neurons were always located in the lateral part of the FN and the extrinsic motor neurons were located in the dorsal aspect of the lateral FN, while intrinsic motor neurons were located more ventrally.

Figure 3. Extrinsic and intrinsic premotor neurons are distributed across the ipsilateral brainstem. (A) Schematic drawing showing the strategy used to label the premotor neurons of the extrinsic and intrinsic muscles. Rabies injections were targeted to either the right extrinsic (*left*) or the right intrinsic (*middle*) muscle in individual animals. Trans-complementation was achieved by co-injecting the Herpes simplex virus

serotype 1 encoding the rabies glycoprotein (HSV-G). Sagittal schematic of the brain showing the rostro-caudal positions (blue dashed lines) corresponding to the coronal sections in the subsequent panels (*right*). Yellow circle indicates Bregma. (B) Coronal section at the level of the spinal trigeminal oralis nucleus (Sp5O). Extrinsic premotor neurons (red) were located in the vestibular nuclei (Ve), the Sp5O and the lateral paragigantocellular nucleus (LPG) (*left*). Intrinsic premotor neurons (green) were located in the intermediate reticular formation (IRt), the Sp5O and the LPG (*middle*). (C) Coronal section at the level of the rostral part of the spinal trigeminal interpolaris nucleus (Sp5Ir). Extrinsic premotor neurons were located in the Sp5Ir and an area spanning the GIRt and the LPG nuclei (*left*). Intrinsic premotor neurons were located in the IRt (*middle*). The Sp5Ir contained very few intrinsic premotor neurons. (D) Coronal section at the level of the caudal part of the spinal trigeminal interpolaris nucleus (Sp5Ic). Extrinsic premotor neurons were located in the GIRt, IRt and ventral portion of the parvocellular reticular formation (PCRt) (*left*). Intrinsic premotor neurons were located in the IRt (*middle*). Some intrinsic premotor cells were also scattered in the PCRt (*middle*). The Sp5Ic contained very few extrinsic or intrinsic premotor cells. (E) Coronal section at the level of the spinal trigeminal caudalis nucleus (Sp5C). Extrinsic (*left*) and intrinsic (*middle*) premotor neurons were located in the medullary dorsal reticular formation (MdD) and the IRt. The Sp5C did not contain either extrinsic or intrinsic premotor cells. The coronal images in panels B to E are overlaid with the corresponding schematic drawings (Paxinos & Franklin, 2001). Simplified schematic maps of premotor neurons are summarized based on consistent results from 5 mice for each injection (*right*). Red regions indicate areas with many extrinsic premotor neurons, green regions show high density of intrinsic premotor neurons, and the brown regions indicate areas occupied by both extrinsic and intrinsic premotor neurons. (F) Quantification of number of labeled extrinsic premotor neurons (n = 5 mice, *far left*) and intrinsic premotor neurons (n = 5 mice, *middle left*). In Sp5Ir, the fraction of extrinsic premotor neurons was significantly higher than the fraction of intrinsic premotor neurons (*middle right*). In the IRt, the fraction of intrinsic premotor neurons was significantly higher than the fraction of extrinsic premotor neurons (*far right*).

Figure 4. Double labeling of extrinsic and intrinsic premotor neurons in the ipsilateral brainstem. (A) Schematic showing the strategy used to label premotor

neurons of the extrinsic and intrinsic muscles in the same animal. Two different Rabies-ΔG viruses encoding EGFP and mCherry were injected unilaterally on the right side of the same mouse into the intrinsic muscle and extrinsic muscle respectively (*left*). Trans-complementation was achieved by co-injecting the Herpes simplex virus serotype 1 encoding the rabies glycoprotein (HSV-G). Sagittal schematic of the brain showing the rostro-caudal positions (blue dashed lines) corresponding to the coronal sections in the subsequent panels (*right*). Yellow circle indicates Bregma. (B**)** Coronal section through the FN and Sp5O in a mouse that received Rabies-ΔG-mCherry + HSV-G in the extrinsic muscle and Rabies-ΔG-EGFP + HSV-G in the intrinsic muscle. Note the intermingled cell distributions in Sp5O and LPG. (C) Coronal section through Sp5Ir of the same mouse. Note the presence of red extrinsic premotor neurons and absence of green intrinsic premotor neurons in Sp5Ir. The IRt has a large number of green intrinsic premotor neurons. (D) Coronal section through Sp5Ic of the same mouse. The Sp5Ic contains neither extrinsic nor intrinsic premotor neurons. Also note the presence of green intrinsic premotor neurons in the IRt region near the NA. The coronal images in panels B to D are overlaid with the corresponding schematic drawings (*right*) (Paxinos & Franklin, 2001). The premotor neuron distributions observed in double-labelled mice were consistent across 4 mice.

Figure 5. Cortical axons in the contralateral brainstem. (A) AAV virus encoding EGFP was injected into either wS1 (*left*) or wM1 (*middle*) of adult mice. Sagittal schematic of the brain showing the rostro-caudal positions (blue dashed lines) corresponding to the coronal sections in the subsequent panels (*right*). Yellow circle indicates Bregma. (B) Coronal sections at the level of Sp5O. At this level, wS1 axons densely innervated the ventral Sp5O (*left*) while wM1 axons innervated GIRt, the lateral facial nucleus (FN) and the PCRt (*middle*). (C) Coronal sections at the level of Sp5Ir. At this level, wS1 axons densely innervated the Sp5Ir (*left*) while wM1 axons densely innervated the PCRt and diffusely innervated the IRt and GIRt (*middle*). (D) Coronal sections at the level of Sp5Ic. At this coronal level, wS1 axons densely innervated the Sp5Ic (*left*) while wM1 axons densely innervated the PCRt and diffusely innervated the IRt and GIRt (*middle*). (E) Coronal sections at the level of Sp5C. At this coronal level, wS1 axons densely innervated the Sp5C (*left*) while wM1 axons broadly innervated the MdD, IRt and MdV nuclei (*middle*). The coronal images in panels B to E

are overlaid with corresponding schematic drawings (*right*) (Paxinos & Franklin, 2001). (F) Quantification of axon intensity in the spinal trigeminal nuclei (Sp5) and the reticular formation (Rt) in animals that received the virus injection in wS1 (*left*) and wM1 (*middle*). The axon intensity was normalized to the background fluorescence (dashed line at 1). Sp5 received significantly stronger input than the Rt from wS1, while the Rt received significantly stronger input than Sp5 from wM1. Schematic drawing showing the distribution of axons from wS1 and wM1 (*right*). Coronal maps were aligned to the images and a contour was drawn around the axon termination sites. The maps were then superimposed. Note that wS1 largely innervates the spinal trigeminal nuclei, while wM1 largely innervates the reticular formation. Some overlap is evident in Sp5O, the ventral part of PCRt and the MdD.

Figure 6. Extrinsic premotor neurons in Sp5Ir receive input from contralateral wS1. (A) Coronal schematic drawing at the level of the Sp5Ir (*left*) (Paxinos and Franklin, 2001). Blue dotted box indicates the area shown in the right panel. AAV virus encoding EGFP was injected into wS1 in the left hemisphere, to label the cortical axons in the brainstem. In the same animal, Rabies-ΔG-mCherry + HSV-G was injected into the right extrinsic muscle to label the premotor neurons. In the contralateral Sp5Ir, the wS1 axons densely innervated the region containing extrinsic premotor neurons (*right*). (B) Orthogonal projections in XY, XZ and YZ planes show close apposition between the cortical axon (green) and the premotor neuron (red) located in Sp5Ir. (C) The neurotransmitter phenotypes of the labeled neurons in Sp5Ir were determined with fluorescent *in situ* hybridization. The large cells in Sp5Ir were negative for GAD67 (*top*) but were positive for Vglut2 (*bottom*). These cells were excitatory. A few smaller cells in Sp5Ir were positive for GAD67 (*top*) and negative for Vglut2 (*bottom*). These cells were inhibitory. (D) Schematic showing a possible motor circuit by which wS1 might drive whisker retraction.

Figure 7. Intrinsic motor neurons in FN and premotor neurons in IRt receive input from contralateral wM1. (A) Coronal section through the facial nucleus (FN) of a ChAT-Cre x LSL-tdTomato mouse. The corresponding schematic drawing is overlaid (*left*). To investigate the potential innervation of FN by wM1, an AAV virus encoding

EGFP was injected into wM1 of ChAT-Cre x LSL-tdTomato mice. The wM1 axons (green) project to the contralateral FN, predominantly in the ventral aspect (*middle*). The images in the left and middle panels are of the same slice. High resolution confocal image of the ventro-lateral FN, showing the EGFP expressing wM1 axons in close apposition with the tdTomato expressing motor neurons (*right*). (B) If wM1 neurons synapse directly onto the motor neurons located in the ventro-lateral FN, then Rabies-ΔG + HSV-G injections in the intrinsic muscle should label premotor neurons in wM1 (*left*). Coronal schematic drawing (Paxinos & Franklin, 2001) at the level of wM1 (*middle*) with a blue dotted box indicating the area of wM1 shown in the right panel. Intrinsic premotor neurons were present in wM1 with labeled neurons located in layers 5 and 6 (*right*). The inset shows a labeled cell in wM1 at higher resolution. (C) Coronal schematic drawing (Paxinos & Franklin, 2001) at the level of the nucleus ambiguus (NA) (*left*). Blue box indicates the area of the IRt shown in the middle and right panels. The wM1 axons projected to the IRt region near to the NA (*middle*). This region was also a major hotspot of intrinsic premotor neurons (*right*). (D) AAV virus encoding EGFP was injected into wM1 of the left hemisphere, to label the cortical axons in the brainstem. In the same mouse, Rabies-ΔG-mCherry + HSV-G was injected into the right intrinsic muscle to label the premotor neurons. In the right IRt, the wM1 axons innervated the intrinsic premotor neurons near to the NA (*left*). Orthogonal projections in XY, XZ and YZ planes show close apposition between the cortical axon (green) and the premotor neuron (red) located in the IRt (*right*). (E) The neurotransmitter phenotypes of the labeled neurons in the IRt were determined with fluorescent *in situ* hybridization. The population of labeled intrinsic premotor neurons in the IRt contained GAD67 positive inhibitory neurons (*top*) as well as Vglut2 positive excitatory neurons (*bottom*). (F) Schematic drawing of a possible circuit by which wM1 might drive whisker movement. The '+' indicates excitatory intrinsic premotor neurons and '–' indicates inhibitory intrinsic premotor neurons in the IRt. Together, these might constitute an oscillator that drives rhythmic whisker protraction.

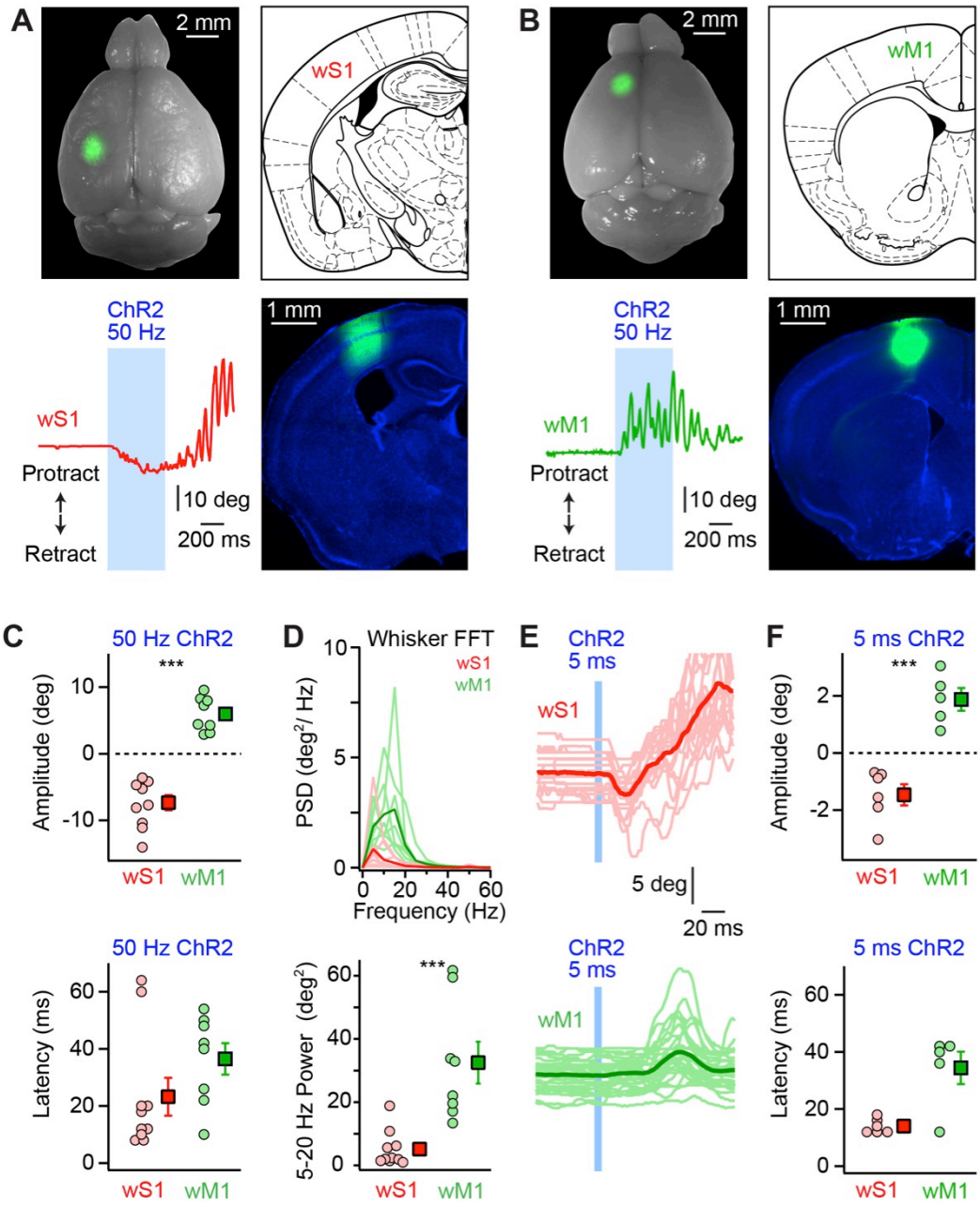

Figure 1
Sreenivasan, Karmakar et al.

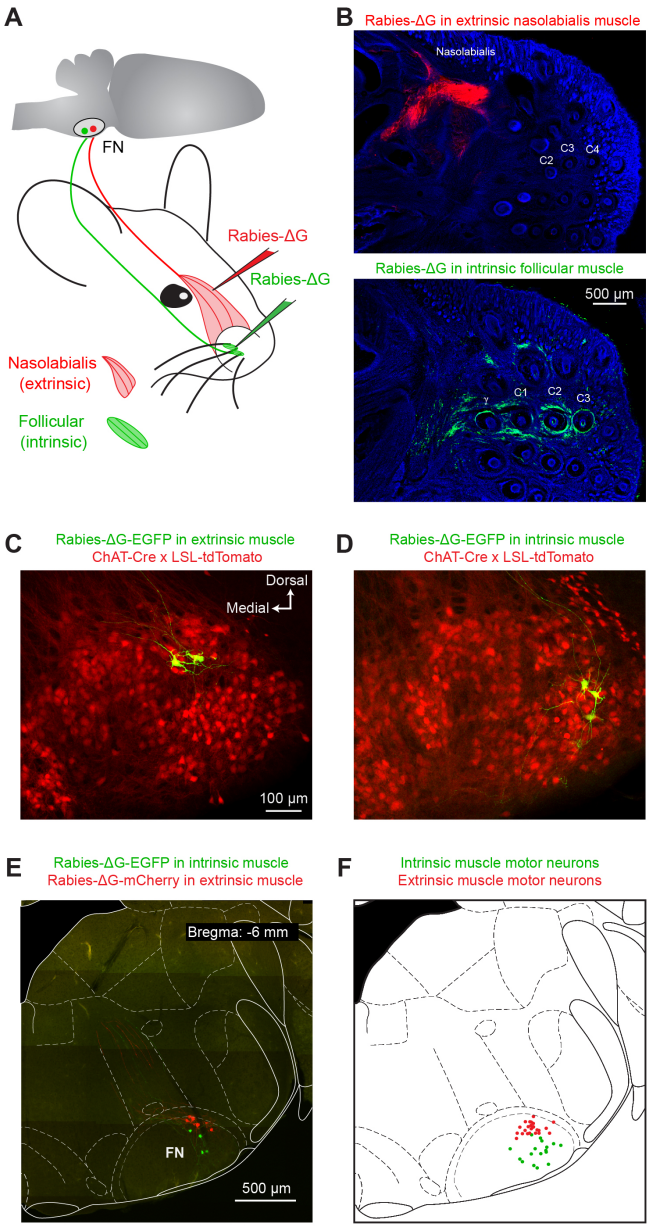

Figure 2
Sreenivasan, Karmakar et al.

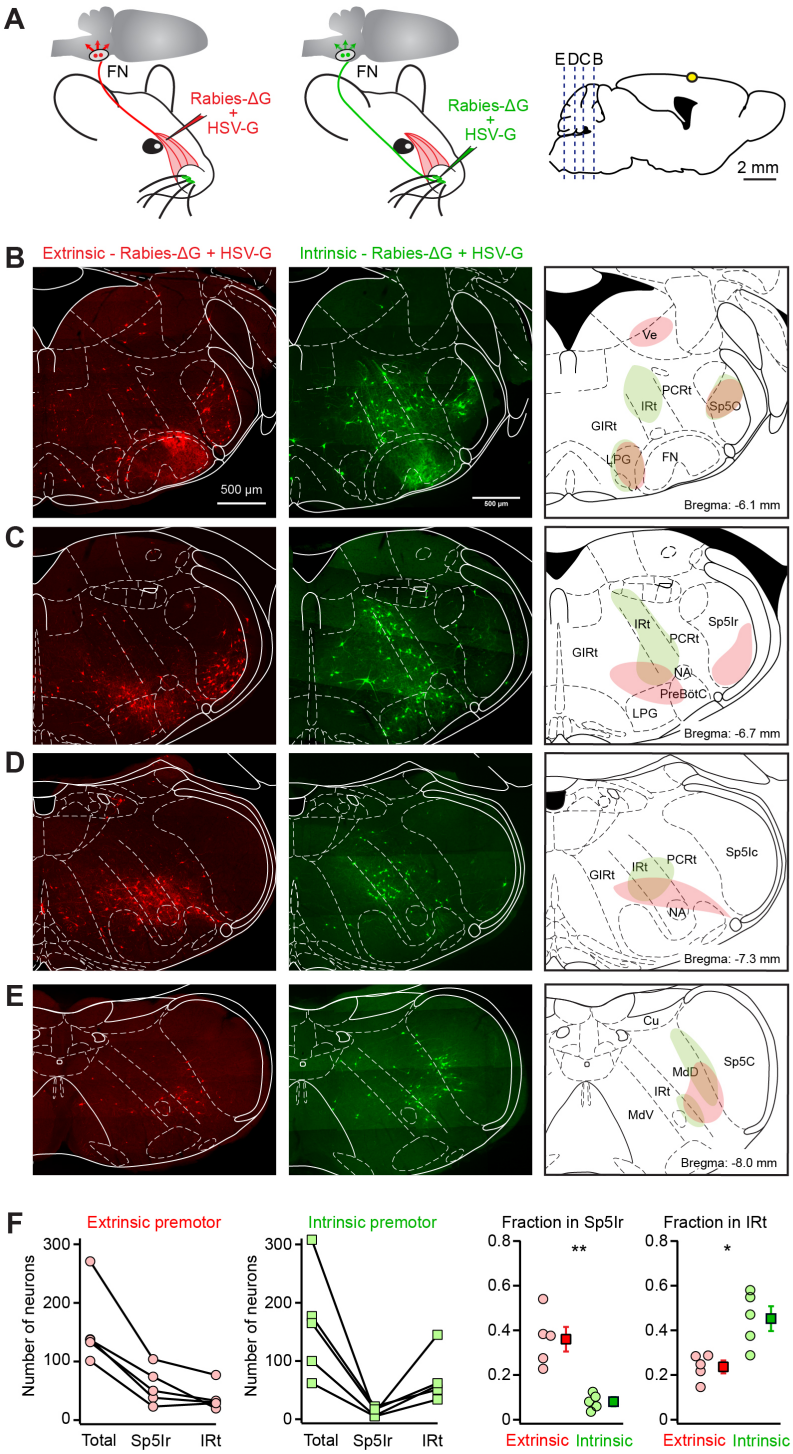

Figure 3
Sreenivasan, Karmakar et al.

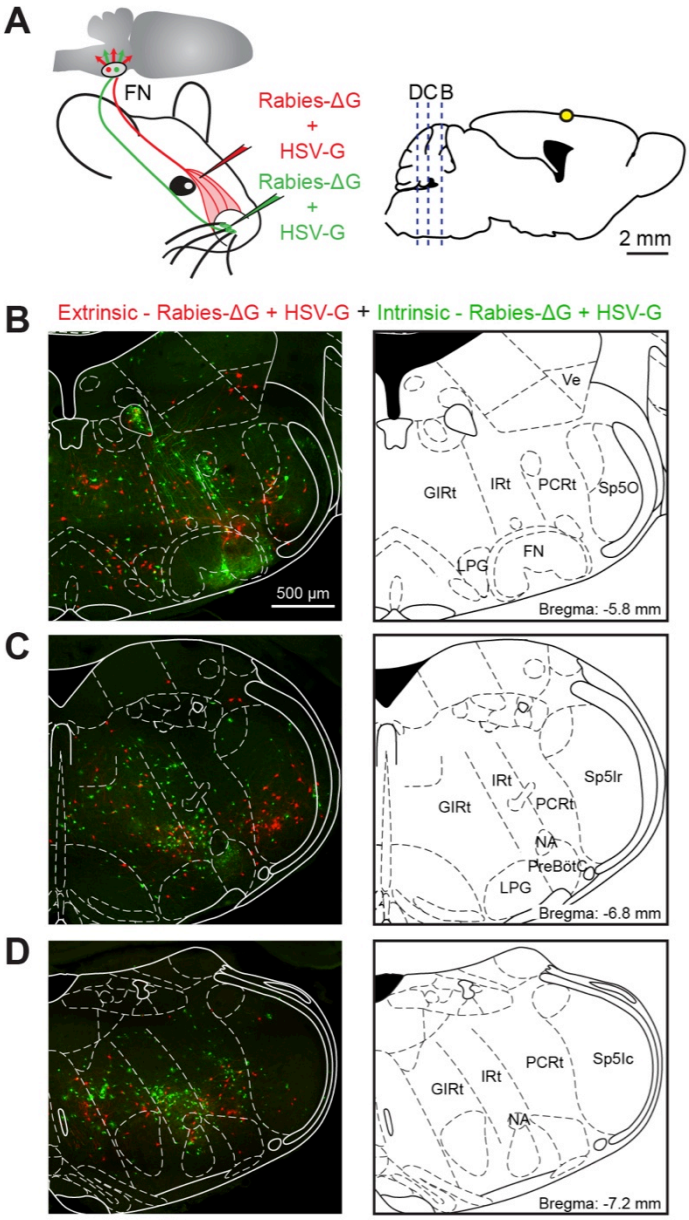

Figure 4
Sreenivasan, Karmakar et al.

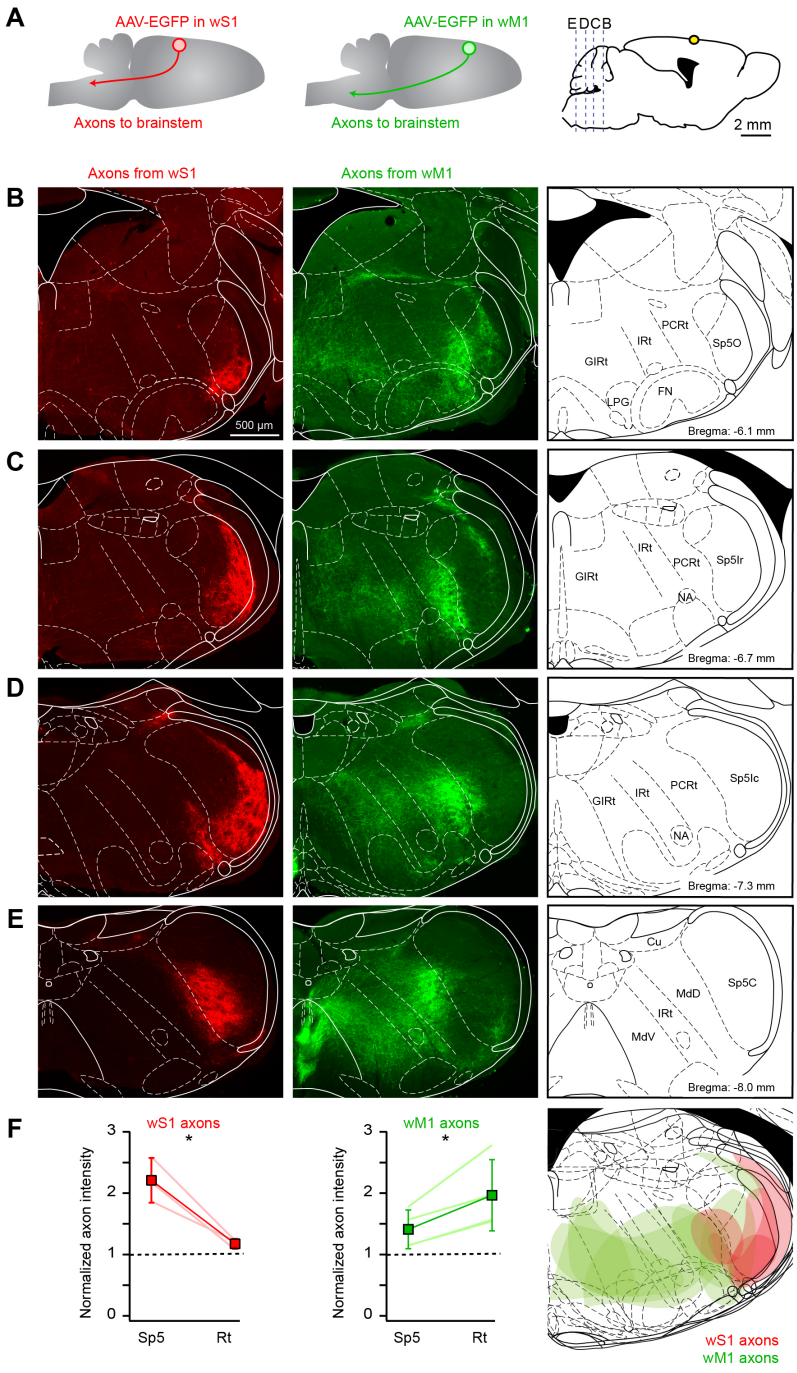

Figure 5
Sreenivasan, Karmakar et al.

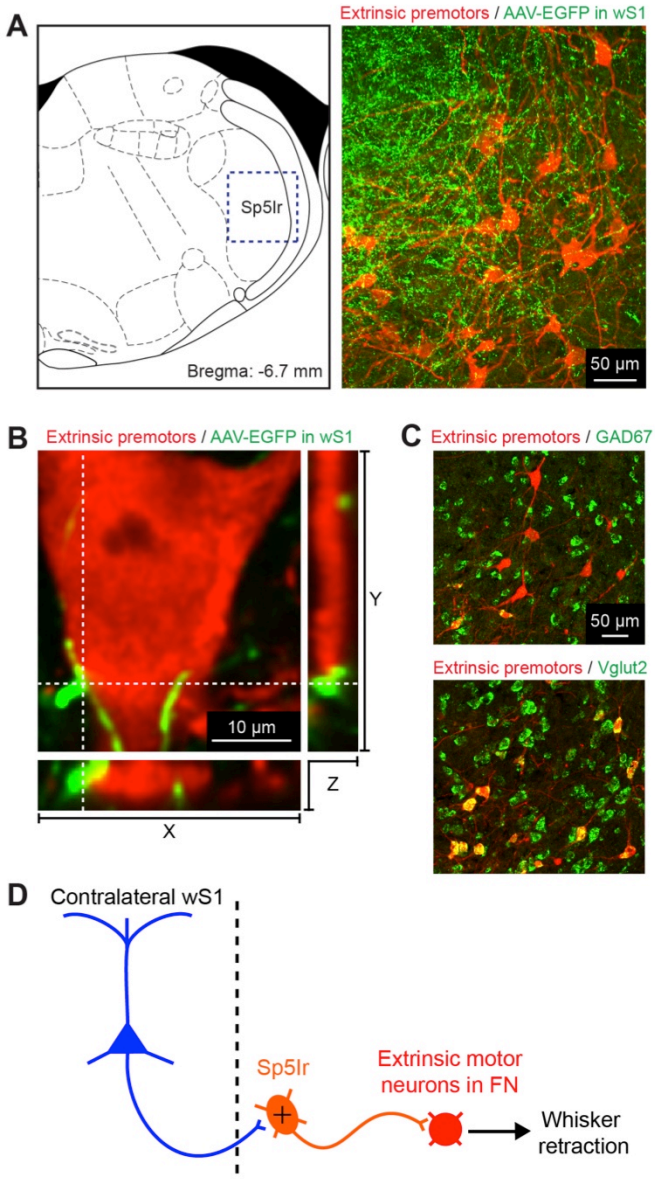

Figure 6
Sreenivasan, Karmakar et al.

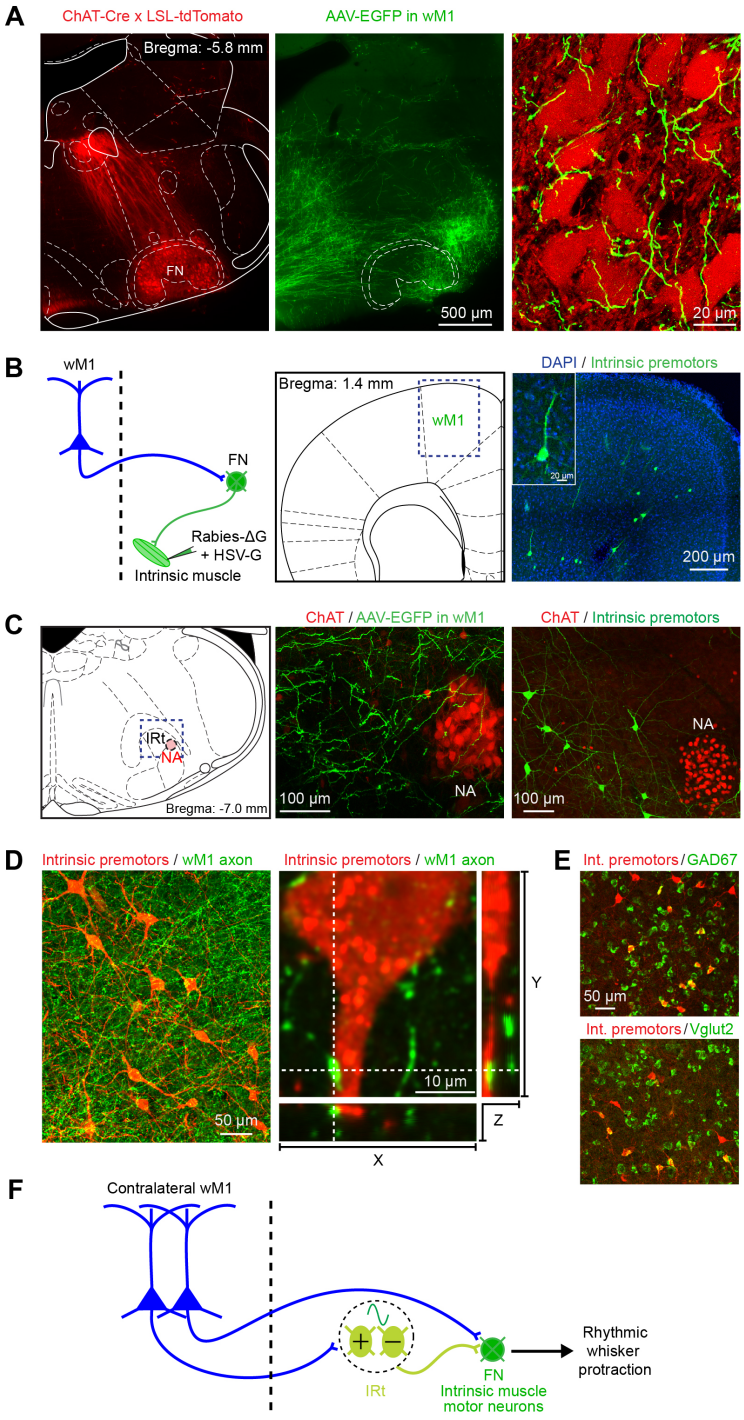

Figure 7
Sreenivasan, Karmakar et al.

Chapter 4: Discussion and Outlook

Hox transcription factors assume a multitude of roles in the development of hindbrain neuronal circuits. Hox genes are involved in different stages of development. They are essential for specifying the rhombomeric progenitor pools in the early stages of embryonic development into their future neuronal fates (Kiecker and Lumsden, 2005), in providing topographic information during migration of the neurons into their future nucleus; as well as in providing topographic specification in setting up the input-output connectivity of the neurons with their upstream and downstream partner nuclei (Philippidou and Dasen., 2013; Di Bonito et al., 2013; Narita and Rijli, 2009; Oury et al., 2006; Di Meglio et al., 2013). In our study, we show the influence of Hox genes on even later stages of development, i.e. during the refinement and maturation of the brainstem auditory circuits.

The tonotopic organization of the auditory circuits and their topographic connectivity is essential for efficient sound processing and sound frequency discrimination. The tonotopic organization of the auditory nuclei is also present in the ventral cochlear nucleus (VCN), in the auditory brainstem (Kandler et al., 2009). The anterior ventral cochlear nucleus (AVCN), subdivision of the VCN, arises from rhombomeres (r) r2-r3 during development and is characterized by expression of Hox paralogous group 2 (*Hox PG2)* genes throughout embryonic stages and early postnatal stages. *Hox PG2* genes, *Hoxa2* and *Hoxb2* have been shown to specify the development of the VCN (Di Bonito et al., 2013; Narita and Rijli, 2009). Earlier study by Di Bonito et al., 2013, showed that *Hoxa2* and *Hoxb2* specify different subdivisions of the VCN during development. Di Bonito et al., 2013 showed that whereas *Hoxa2* is involved in AVCN formation and in developing the VCN-MNTB (medial nucleus of trapezoid body) connectivity (essential for sound localization), *Hoxb2* is more influential in the development of the posterior ventral cochlear nucleus (PVCN) and the efferent pathways from the hindbrain to the cochlea, part of the olivocochlear system. However, an involvement of *Hox PG2* genes in the tonotopic organization and in the topographic mapping of the AVCN input-output connectivity has not yet been shown. Since Hox genes are determinants of topographic specificity, we looked into the influence of *Hox PG2* genes on the tonotopic development of the AVCN.

Our results show that the conditional deletion of *Hox PG2* genes using a *Cre* driver line that specifically targets the postmitotic bushy cells in the AVCN, doesnot affect the gross tonotopic organization of the AVCN. The spiral ganglion (SG) afferent fibers responding to different frequencies also project to the AVCN in the correct tonotopic order along the dorso-ventral axis of the AVCN. Our results are in agreement with previous observations that the tonotopic development of the auditory circuits is pre-determined and developmentally hard-wired. The tonotopic order of brainstem auditory nuclei is also reportedly unperturbed in absence of sound and in deaf animals, suggesting that it is laid out very early in development and possibly depends on the temporal order of patterning of the nuclei (Kandler et al., 2009; Leake et al., 2006; Koundakjian et al., 2009), rather than on any molecular topographic determinant. However, our observations that the SG afferents in the *Hox PG2* mutants, though projecting in the correct tonotopic order, but targeting a broader area in the AVCN is interesting. This is reminiscent of the studies from cats, which shows that labeled SG afferents project to a broader area in the cochlear nucleus (CN) of newborn kittens, relative to the targeted area in the adult cats. Also, similar broadening of SG afferents has been observed in deaf cats, in the absence of activity (Leake et al., 2002; Ryugo et al., 1997). Thus, this suggests tonotopic maps once formed, undergoes refinement, which involves sharpening of the SG afferents target area in the AVCN. Our results show that in absence of *Hox PG2*, the sharpening of the bands in the AVCN is affected. In addition, due to the specificity of the *Cre* driver ($Math1^{Cre}$) that specifically targets post-mitotic neurons, we bypass the effects due to early deletion of *Hox PG2* genes reported earlier (Di Bonito et al., 2013) and donot observe any transformation of the VCN subdivisions in our conditional *Hox PG2* mutants.

Tonotopic organization in all brainstem auditory nuclei undergo extensive refinements in order to form spatially restricted well-defined bands encoding specific frequencies, during pre-natal and post-natal stages of development. Such refinement of tontopic bands is influenced by activity, both pre-hearing spontaneous activity as well as post-hearing sound induced activity. Due to the technical difficulties involved in studying SG afferents to the VCN in adult animals, most studies on tonotopic refinement are concentrated on the inhibitory projections from MNTB to lateral superior olivary complex (LSO) (Kandler et al., 2009; Clause et al., 2014). Change in firing patterns of spontaneous activity has shown to impair the spatial restriction of the

MNTB projections within well-defined bands in the LSO due to lack of post hearing refinement of MNTB axons (Clause et al., 2014). Similar results have also been shown with congenitally deaf mice where refinement is interrupted (Walmsley et al. 2006; Cao et al., 2008) due to lack of activity or alteration in patterns of acitivity. Thus activity plays an essential role in refining the auditory circuits both during pre-hearing and post-hearing phases. Thus, next we needed to check if the conditional *Hox PG2* mutants were able to form functional connections and relay activity to the AVCN from the periphery.

To check if the conditional *Hox PG2* mutants form functional connections between the SG afferents and the AVCN principal neurons, we performed auditory stimulation experiments with pure frequency tones and checked for c-Fos (early response gene) activation patterns in the AVCN. Our results suggested that the SG afferents transmitted the acoustic signals to the AVCN and DCN, as bands of c-Fos labeled activated neurons were observed in the mutants similar to the controls. The positions of the activated neuronal bands were also in accordance with the tonotopic organization, such that neurons activated in response to higher pure tone frequency was more dorsally located and neurons activated in response to lower pure tone sound frequency were more ventrally located in the AVCN. However, replicating the earlier described phenotype of the SG afferents in the AVCN, the c-Fos bands were significantly broader along the tonotopic axis in the mutants compared to the control. To investigate whether this affected their hearing, we subjected the mutants and control animals to an auditory tone based fear-conditioning experiment, where we coupled a foot shock to one pure tone (CS+) and played another neighboring pure tone without presenting a foot shock (CS-). Our results showed that the mutants were able to associate the auditory cues with the foot shock, freezing in response to the sound cue; suggesting that their hearing function was intact. However, the conditional *Hox PG2* mutants failed to discriminate between the CS+ and CS-, freezing in response to both the tones; whereas, the control showed freezing response only to the CS+ tone. Thus, though the hearing function was itself not affected, however, the ability to discriminate two neighboring sound frequencies was significantly compromised in the absence of the *Hox PG2* genes. This lack of discrimination could be explained on the basis of the broadening of the tonotopic bands in the conditional *Hox PG2* mutants. In the mutants, the c-Fos labeled bands corresponding to the two neighboring pure tone frequencies

were significantly broader than in the controls, resulting in reduced separation between them. Also overlapping between activated neuronal bands responding to two neighboring frequencies was observed in the mutant AVCN in some cases. This broadening and overlapping of activated neurons in the AVCN suggest the possibility of activation of individual principal neurons in AVCN by multiple pure tone frequencies, which may result in decreased resolution of tonotopic representation and reduced discrimination of sound frequencies in the *Hox PG2* deficient mutants. This enlargement of isofrequency bands could be a consequence of the lack of refinement of SG afferents targeting the AVCN in the *Hox PG2* mutants. Our results also suggest that the lack of refinement of the SG afferents is not a transient phenotype and is maintained even at later stages in the conditional *Hox PG2* mutants.

Similar broadening of c-Fos activated neuronal bands in the DCN has been reported earlier in *Ephrinb2* heterozygous mutants (homozygotes mutants are lethal), where a significant broader spread of the activated neurons along the tonotopic axis was observed (Miko et al., 2007). Due to the similarity in the phenotype, we considered *Ephrinb2* as a possible candidate for a *Hox PG2* downstream effector molecule. Using RNA solid sequencing, we looked for deregulated genes in the conditional *Hox PG2* mutants. Our results showed a significant decrease in *Ephrinb2* in our *HoxPG2* mutants. Eph/Ephrin axon guidance molecules are essential for topographic map formation in the visual system (McLaughlin and O'Leary, 2005). Mutant mice lacking Ephrins show functional changes in their cortical maps in response to both visual and somatosensory stimulations (Intskirveli et al., 2011). Due to their role in topographic map formation, Eph/Ephrin molecules could be involved in the formation of tontopic maps. In addition to their activity-independent roles in axon guidance, Eph/Ephrin signaling has been shown to be involved in maturation of synapses in an activity dependent manner (Klein 2009; Hruska et al., 2012). The downregulation of *Ephrinb2* in the conditional *Hox PG2* mutants and the similarity in the phenotypes in *Ephrinb2* heterozygous mutants and the conditional *Hox PG2* mutants, thus suggest that *Ephrinb2* may be functioning downstream of *Hox PG2* genes in the AVCN in the refinement and maturation of the tonotopic maps.

Our RNA sequencing data further show an upregulation of many proteins involved in synaptic transmission (such as NMDAR receptor subunit, NR1), neuronal synaptic plasticity, calcium ion binding and channel activity regulation, in the

conditional *Hox PG2* mutant AVCN. Calcium associated synaptic activity is involved in the proper formation of synapses and in maturation of synapses (Tritsch et al., 2010) in the auditory system. Also, several activity dependent processes involving elimination of axonal inputs and pruning of afferents are involved in the formation and maturation of the giant Endbulb of Held synapses, between SG afferents and AVCN bushy cells (Lu and Trussel., 2007). The elimination of axonal inputs during Endbulb formation is dependent on NMDAR quantal size as revealed from studies in chick (Tritsch et al., 2010; Lu and Trussel., 2007; Brenowitz and Trussel, 2001). Thus, this increase in NR1 and in calcium signaling molecules in the conditional *Hox PG2* mutants, led us to hypothesize that Endbulb of Held formation may be affected in these mutants. The Endbulb of Held is a complex synapse that acquires its final shape through multiple rounds of activity dependent refinement. In our *Hox PG2* conditional mutants, we observed not a loss of axonal terminals, but a reduction in the size of the axonal terminal and multiple large axonal terminals, innervating single bushy cell in the AVCN. This is in contrast with the Endbulbs in the controls, where a single axonal terminal is seen to have multiple branches, which together encapsulate the entire surface of the principal bushy cell in the AVCN. Thus, conditional deletion of *Hox PG2* genes in the bushy cells of AVCN results in alteration in synaptic maturation of the Endbulb synapses and multi-innervation of single bushy cells.

An interesting observation in our study is that adult single conditional *Hoxa2* or *Hoxb2* mutants also show similar phenotype in the auditory stimulation experiments as the compound *Hox PG2* mutants, more prominently in the conditional *Hoxb2* mutants. This is in particular interest, because single conditional mutants lack a phenotype at earlier developmental stages, whereas, the compound mutants already show a phenotype at such a stage. This could be attributed to the redundancy in the functional roles of the *Hox PG2* genes during development, thus one compensating for the lack of the other, resulting in mild or no phenotype, but in absence of both the genes, a significant phenotype is observed. However, at adult stages, single conditional mutants themselves show phenotypes similar to double mutants, which could suggest specific roles for individual *Hox PG2* genes during postnatal development, may be regulating different aspects of refinement.

Our present study supports additional roles for *Hox PG2* genes in later stages of development of the hindbrain auditory system, especially during stages when

refinement and maturation of circuits are predominant. Our study also opens up a repertoire of questions regarding the involvement of Hox genes in circuit formation and maturation. In addition to exploring the roles of individual *Hox PG2* genes in the maturation of the tonotopic precision, it would be interesting to explore the mechanism involved in the refinement of the already precise brainstem auditory circuits. Our study suggests involvement of Hox genes in regulating expression levels of activity regulating genes and genes involved in synapse maturation, thus, it would be interesting to further identify the direct pathways linking Hox genes to synaptic maturation.

The mystacial system in mice is an essential sensory system used to collect tactile information during navigation. Movements of the whiskers are under cortical control, with motor cortex (M1) controlling whisker protraction and somatosensory cortex (S1) controlling whisker retraction, during rhythmic whisking (Petersen, 2014). Blocking S1 activity has shown to affect whisker retraction and can also inhibit retraction mediated by activating M1 retraction center. The M1 and S1 mediated opposing whisker movements are considered to be mediated via two parallel pathways involving separate brainstem nuclei. In Matyas et al., 2010, it was proposed that M1 driven whisker protraction occurs via M1-iRT-FMN pathway, whereas, S1 driven whisker retraction occurs via S1-SpVi-FMN pathway. In this study, we confirm the above hypothesis, by anatomically tracing the entire circuits (from periphery to cortex) involved in retraction and protraction, using a combination of retrograde and anterograde tracing techniques. We used retrograde labeling from individual sets of retraction related extrinsic muscles to show a unique population of premotor neurons in the anterior SpVi in the brainstem. We also showed that these premotor neurons receive S1 cortical inputs by coupling anterograde tracing from the S1 cortex with the retrograde tracings. Similarly, we also showed that protraction associated intrinsic muscles are driven by premotors preferentially located in the iRT and receiving inputs from the M1 cortex. Our premotors distributions for tracing from both intrinsic and extrinsic muscles were in agreement with previously published results (Takatoh et al., 2013).

Though, we successfully outline the anatomical neuronal connectivity for whisker movement, it would be interesting to study the functional effects of inactivating different components of each pathway. Experiments targeting specific subsets of premotor neurons identified in both the pathways could help us understand their

specific roles in the control of whisker movements. Motor control by sensory cortex is very fascinating and suggests for possible sensory-motor interactions or feedback loops. Several feedback loops are known to exist in the whisker sensori-motor systems. Our study also identifies SpVi, sensory trigeminal nuclei, involved in whisker retraction control. It would also be very interesting to investigate further existence of additional sensori-motor loops at the hindbrain level.

Bibliography

Berg, R. W. and D. Kleinfeld. "Rhythmic Whisking by Rat: Retraction as Well as Protraction of the Vibrissae Is under Active Muscular Control." *J Neurophysiol* 89, no. 1 (2003): 104-17.

Brenowitz, S. and L. O. Trussell. "Maturation of Synaptic Transmission at End-Bulb Synapses of the Cochlear Nucleus. " J Neurosci 27, no. 23 (2001): 9487-98.

Borst, J. G. and J. Soria van Hoeve. "The Calyx of Held Synapse: From Model Synapse to Auditory Relay." *Annu Rev Physiol* 74, (2012): 199-224.

Cao, X.J., McGinley, M.J. & Oertel, D. "Connections and synaptic function in the posteroventral cochlear nucleus of deaf jerker mice. " *J. Comp. Neurol*. 510, 297–308 (2008)

Clause, A., G. Kim, M. Sonntag, C. J. Weisz, D. E. Vetter, R. Rubsamen and K. Kandler. "The Precise Temporal Pattern of Prehearing Spontaneous Activity Is Necessary for Tonotopic Map Refinement." *Neuron* 82, no. 4 (2014): 822-35.

Cramer, K. S. and M. L. Gabriele. "Axon Guidance in the Auditory System: Multiple Functions

of Eph Receptors." *Neuroscience* 277, (2014): 152-62.

Di Bonito, M., Y. Narita, B. Avallone, L. Sequino, M. Mancuso, G. Andolfi, A. M. Franze, L. Puelles, F. M. Rijli and M. Studer. "Assembly of the Auditory Circuitry by a Hox Genetic Network in the Mouse Brainstem." *PLoS Genet* 9, no. 2 (2013): e1003249.

Di Meglio, T., C. F. Kratochwil, N. Vilain, A. Loche, A. Vitobello, K. Yonehara, S. M. Hrycaj, B. Roska, A. H. Peters, A. Eichmann, D. Wellik, S. Ducret and F. M. Rijli. "Ezh2 Orchestrates Topographic Migration and Connectivity of Mouse Precerebellar Neurons." *Science* 339, no. 6116 (2013): 204-7.

Erzurumlu, R. S., Y. Murakami and F. M. Rijli. "Mapping the Face in the Somatosensory Brainstem." *Nat Rev Neurosci* 11, no. 4 (2010): 252-63.

Esposito, M. S., P. Capelli and S. Arber. "Brainstem Nucleus Mdv Mediates Skilled Forelimb Motor Tasks." *Nature* 508, no. 7496 (2014): 351-6.

Farago, A. F., R. B. Awatramani and S. M. Dymecki. "Assembly of the Brainstem Cochlear Nuclear Complex Is Revealed by Intersectional and Subtractive Genetic Fate Maps." *Neuron* 50, no. 2 (2006): 205-18.

Fox, K. and R. O. Wong. "A Comparison of Experience-Dependent Plasticity in the Visual and Somatosensory Systems." *Neuron* 48, no. 3 (2005): 465-77.

Fujiyama, T., M. Yamada, M. Terao, T. Terashima, H. Hioki, Y. U. Inoue, T. Inoue, N. Masuyama, K. Obata, Y. Yanagawa, Y. Kawaguchi, Y. Nabeshima and M. Hoshino. "Inhibitory and Excitatory Subtypes of Cochlear Nucleus Neurons Are Defined by Distinct Bhlh Transcription Factors, Ptf1a and Atoh1." *Development* 136, no. 12 (2009): 2049-58.

Haidarliu, S., E. Simony, D. Golomb and E. Ahissar. "Muscle Architecture in the Mystacial Pad of the Rat." *Anat Rec (Hoboken)* 293, no. 7 (2010): 1192-206.

Hruska, M. and M. B. Dalva. "Ephrin Regulation of Synapse Formation, Function and Plasticity." Mol Cell Neurosci 50, no. 1 (2012): 35-44.

Hsieh, C. Y., P. A. Nakamura, S. O. Luk, I. J. Miko, M. Henkemeyer and K. S. Cramer. "Ephrin-B Reverse Signaling Is Required for Formation of Strictly Contralateral Auditory Brainstem Pathways." *J Neurosci* 30, no. 29 (2010): 9840-9.

Huberman, A. D., M. B. Feller and B. Chapman. "Mechanisms Underlying Development of Visual Maps and Receptive Fields." *Annu Rev Neurosci* 31, (2008): 479-509.

Intskirveli, I., R. Metherate and K. S. Cramer. "Null Mutations in Ephb Receptors Decrease Sharpness of Frequency Tuning in Primary Auditory Cortex." *PLoS One* 6, no. 10 (2011): e26192.

Jackson, H. and T.N. Parks, "Functional Synapse elimination in the Developing Avian Cochlear Nucleus with simultaneous Reduction in Cochlear Nerve Axon Branching. " J Neurosc., Vol.2, No. 12, (1982):1736-1743

Kandler, K., A. Clause and J. Noh. "Tonotopic Reorganization of Developing Auditory Brainstem Circuits." *Nat Neurosci* 12, no. 6 (2009): 711-7.

Kiecker, C. and A. Lumsden. "Compartments and Their Boundaries in Vertebrate Brain Development." *Nat Rev Neurosci* 6, no. 7 (2005): 553-64.

Klein, R. "Bidirectional Modulation of Synaptic Functions by Eph/Ephrin Signaling." Nat Neurosci 12, no. 1 (2009): 15-20

Koundakjian, E. J., J. L. Appler and L. V. Goodrich. "Auditory Neurons Make Stereotyped Wiring Decisions before Maturation of Their Targets." *J Neurosci* 27, no. 51 (2007): 14078-88.

Lauer, A. M., C. J. Connelly, H. Graham and D. K. Ryugo. "Morphological Characterization of Bushy Cells and Their Inputs in the Laboratory Mouse (Mus Musculus) Anteroventral Cochlear Nucleus." *PLoS One* 8, no. 8 (2013): e73308.

Leake, P. A., G. T. Hradek, L. Chair and R. L. Snyder. "Neonatal Deafness Results in Degraded Topographic Specificity of Auditory Nerve Projections to the Cochlear Nucleus in Cats." *J Comp Neurol* 497, no. 1 (2006): 13-31.

Leake, P. A., R. L. Snyder and G. T. Hradek. "Postnatal Refinement of Auditory Nerve Projections to the Cochlear Nucleus in Cats." *J Comp Neurol* 448, no. 1 (2002): 6-27.

Limb, Charles J. and David K. Ryugo. "Development of Primary Axosomatic Endings in the Anteroventral Cochlear Nucleus of Mice." *Journal of the Association for Research in Otolaryngology* 1, no. 2 (2000): 103-119.

Lu, T. and L. O. Trussell. "Development and Elimination of Endbulb Synapses in the Chick Cochlear Nucleus." *J Neurosci* 27, no. 4 (2007): 808-17.

Manis, Paul B., Ruili Xie, Yong Wang, Glen S. Marrs and George A. Spirou. "The Endbulbs of Held." 41, (2012): 61-93.

Mann, Z. F. and M. W. Kelley. "Development of Tonotopy in the Auditory Periphery." *Hear Res* 276, no. 1-2 (2011): 2-15.

Maricich, S. M., A. Xia, E. L. Mathes, V. Y. Wang, J. S. Oghalai, B. Fritzsch and H. Y. Zoghbi. "Atoh1-Lineal Neurons Are Required for Hearing and for the Survival of Neurons in the Spiral Ganglion and Brainstem Accessory Auditory Nuclei." *J Neurosci* 29, no. 36 (2009):

11123-33.

Marrs, G. S. and G. A. Spirou. "Embryonic Assembly of Auditory Circuits: Spiral Ganglion and Brainstem." *J Physiol* 590, no. Pt 10 (2012): 2391-408.

Matyas, F., V. Sreenivasan, F. Marbach, C. Wacongne, B. Barsy, C. Mateo, R. Aronoff and C. C. Petersen. "Motor Control by Sensory Cortex." *Science* 330, no. 6008 (2010): 1240-3.

Michalski, N., N. Babai, N. Renier, D. J. Perkel, A. Chedotal and R. Schneggenburger. "Robo3-Driven Axon Midline Crossing Conditions Functional Maturation of a Large Commissural Synapse." *Neuron* 78, no. 5 (2013): 855-68.

Miko, I. J., P. A. Nakamura, M. Henkemeyer and K. S. Cramer. "Auditory Brainstem Neural Activation Patterns Are Altered in Epha4- and Ephrin-B2-Deficient Mice." *J Comp Neurol* 505, no. 6 (2007): 669-81.

Narita, Yuichi and Filippo M. Rijli. "Chapter 5 Hox Genes in Neural Patterning and Circuit Formation in the Mouse Hindbrain." 88, (2009): 139-167.

Oury, F., Y. Murakami, J. S. Renaud, M. Pasqualetti, P. Charnay, S. Y. Ren and F. M. Rijli. "Hoxa2- and Rhombomere-Dependent Development of the Mouse Facial Somatosensory Map." *Science* 313, no. 5792 (2006): 1408-13.

Petersen, C. C. "Cortical Control of Whisker Movement." *Annu Rev Neurosci* 37, (2014): 183-203.

Philippidou, P. and J. S. Dasen. "Hox Genes: Choreographers in Neural Development, Architects of Circuit Organization." *Neuron* 80, no. 1 (2013): 12-34.

Rubel, E. W. and B. Fritzsch. "Auditory System Development: Primary Auditory Neurons and Their Targets." *Annu Rev Neurosci* 25, (2002): 51-101.

Ryugo, D.K., Ponstaporn, T., Huchton., D.M. andJ. K. Niparko. "Ultrastructural Analysis of Primary Endings in Deaf White Cats: Morphologic Alterations in Endbulbs of Held". J. Comp. Neuorol: 385 (1997): 230-44.

Ryugo, D. K., K. L. Montey, A. L. Wright, M. L. Bennett and T. Pongstaporn. "Postnatal Development of a Large Auditory Nerve Terminal: The Endbulb of Held in Cats." *Hear Res* 216-217, (2006): 100-15.

Takatoh, J., A. Nelson, X. Zhou, M. M. Bolton, M. D. Ehlers, B. R. Arenkiel, R. Mooney and F. Wang. "New Modules Are Added to Vibrissal Premotor Circuitry with the Emergence of Exploratory Whisking." *Neuron* 77, no. 2 (2013): 346-60.

Tripodi, M., A. E. Stepien and S. Arber. "Motor Antagonism Exposed by Spatial Segregation and Timing of Neurogenesis." *Nature* 479, no. 7371 (2011): 61-6.

Tritsch, N. X., A. Rodriguez-Contreras, T. T. Crins, H. C. Wang, J. G. Borst and D. E. Bergles. "Calcium Action Potentials in Hair Cells Pattern Auditory Neuron Activity before Hearing Onset." *Nat Neurosci* 13, no. 9 (2010): 1050-2.

Walmsley, B., Berntson, A., Leao, R.N. & Fyffe, R.E. "Activity-dependent regulation of synaptic strength and neuronal excitability in central auditory pathways. " *J. Physiol.* (Lond.) 572, 313–321 (2006).

Wang, V. Y., M. F. Rose and H. Y. Zoghbi. "Math1 Expression Redefines the Rhombic Lip Derivatives and Reveals Novel Lineages within the Brainstem and Cerebellum." *Neuron* 48, no. 1 (2005): 31-43.

Wickersham, I. R., D. C. Lyon, R. J. Barnard, T. Mori, S. Finke, K. K. Conzelmann, J. A. Young and E. M. Callaway. "Monosynaptic Restriction of Transsynaptic Tracing from Single, Genetically Targeted Neurons." *Neuron* 53, no. 5 (2007): 639-47.

Young,E.D., and Oertel,D. 2010. Cochlear Nucleus. In Handbook of Brain Microcircuits, G.M. Shepherd, and S. Grillner, eds. (New York: Oxford), pp. 215-223.

Young ED, Oertel D. 2003. The Cochlear Nucleus. In: Synaptic Organization of the Brain, GM Shepherd editor, Oxford University Press, NY, Chapter 4, pp125-163.

Acknowledgements

I would like to thank my Ph.D supervisor Prof. Dr. Filippo M. Rijli for his guidance and support in performing all the experiments described in this thesis. I would also like to thank him for useful and enlightening discussions over results and for his encouragement in pursuing new ideas and difficult questions. I would like to thank my Thesis Committee members: Prof. Dr. Botond Roska and Dr. J.-F. Brunet and other participating members: Dr. Jan Pielage and Prof. Dr. Silvia Arber for being the Chair of the Committee.

I would also express my gratitude to my collaborators from EPFL, Switzerland, Varun Sreenivasan and Prof. Dr. C.C. Petersen for setting up a fruitful collaboration as well as for many interesting discussions. I would also like to thank Christian Mueller, Joao Bacelo and Milica Markovic of Andreas Luethi's group in FMI for their help in performing the behavioural experiments. I would like to thank Prof. Dr.Andreas Luethi for their collaboration.

I am grateful to all members of Rijli lab in FMI, Ahmad Bechara, Alberto Loche, Dominik Kraus, Nathalie Vilain, Sebastien Ducret, Maryline Minoux, Nicola Maiorano, Sjoerd Holwerda, Vanja Cankovic and Upasana Maheshwari, as well as to past members, Thomas Di Meglio, Claudius Kratochwil, Antonio Vitobello, Liseth Parra and Christophe Laummonerie. I am especially thankful to Yuichi Narita, who initiated me into the auditory research project and for his contribution in the study.

A special thanks to all the facilities in the FMI, especially to Christel Genoud, Raphael Thierry and Moritz Kirschmann, who helped in Image Processing, to the FAIM Imaging facilities, Histology, Genomics and members of the Animal Facility. I would also like to thank Kamill Balint for his help in setting up the viral production in our lab.

Last, but not the least, I would like to thank my family, especially my parents and husband for always being pillars of support.

Curriculum vitae

KAJARI KARMAKAR

Doctoral student

Friedrich Miescher Institute for Biomedical Research, Basel, Switzerland

Personal Information

Address	Landskronstrasse 20, 4056 Basel
Email	kajari.karmakar@fmi.ch; kajari.karmakar@gmail.com
Mobile	+41 789498693
Date of birth	18.11.1984
Nationality	Indian
Gender	Female

Education

2009 – present Ph.D Thesis, Friedrich Miescher Institute for Biomedical Research, Basel, Switzerland
Ph.D supervisor: Prof. Dr. Filippo M. Rijli
"Hox genes and tonotopic organization of auditory brainstem circuits."
(Detailed summary attached)

2006 – 2009 Masters in Biological Sciences (Integrated Ph.D.), Indian institute of Science, Bangalore, India
Master's thesis supervisor: Dr. Dipankar Chatterji
"A study on the functional and the regulatory roles of the Dps homologues in *Mycobacterium smegmatis*"

2003 – 2006 Bachelor in Science, Biochemistry (Hons.), Sri Venkateswara College, University of Delhi

Additional Research Projects

2011 – 2014 "Parallel pathways from motor and somatosensory cortex for controlling whisker movements in mice." - in collaboration with Varun Sreenivasan from Carl Petersen's laboratory, EPFL, Brain Mind Institute, Lausanne, Switzerland.

July 2007 – Nov 2007 "Mapping the epitope of the rABA-specific neutralizing monoclonal antibody."
Department of Biochemistry, Indian Institute of Science,

Bangalore, India
Project Supervisor - Prof. Anjali A. Karande

Jan 2007 – April 2007

"A study on the role of cuticular hydrocarbons in nestmate recognition in the Green Tree Ant (*Oecophylla smaragdina*)."
Centre for Ecological Sciences, Indian Institute of Science, Bangalore, India
Project Supervisor - Dr. Reneé M Borges

May 2005 – July 2005

"Trends in codon usage in closely related species of Bacillus"
Bioinformatics Centre and Human Genetics and Genomics Group, Indian Institute of Chemical Biology, Kolkata, India.
Project Supervisor - Dr. Chitra Dutta

Aug 2005 – Dec 2005

"Amplification of the gene rv1211 from Mycobacterium tuberculosis by Polymerase Chain Reaction and overexpressing the recombinant protein".
"Raising antibodies against purified rCAMLP using mice as the model".
Sri Venkateswara College, University of Delhi,
Project supervisors - Dr. P. Hemlatha Reddy and Dr. Nandita Narayanasamy

Publications

- ✓ Karmakar K, Narita Y, Loche A, Ducret S, Genoud C, Thierry R, Luthi A and Rijli, F. M. (2014): Hox genes and tonotopic organization of auditory brainstem circuits (manuscript in preparation).

- ✓ Sreenivasan V. *, Karmakar K. *, Rijli F.M. and Petersen C.C. (2014): Parallel pathways from motor and somatosensory cortex for controlling whisker movements in mice. (Manuscript submitted to European Journal of Neuroscience –Neurosystems)

  * Equal contribution

- ✓ Ghatak P, Karmakar K, Kasetty S, Chatterji D.(2011) Unveiling the role of Dps in the organization of mycobacterial nucleoid. PLoS One.Jan 24;6(1)

Scholarships

- ✓ Scholarship "International PhD program" funded by Friedrich Miescher Institute for Biomedical Research, Basel

- ✓ Scholarship “Integrated Ph.D program (Masters)” funded by Indian Institute of Science, Bangalore, India

- ✓ Awarded CSIR (Center for Scientific and Industrial Research) fellowship for conducting a research project in Indian Institute of Chemical Biology, Kolkata, India

Posters and Meetings

- ✓ Presented a poster in 2013 COST HOX and TALE Meeting, October 2-4, Egmond aan Zee (North Holland), The Netherlands

- ✓ Tenth Asian Conference on Transcription, Indian Institute of Science, Bangalore, 13th -16th January 2008 (ActX Conference)

Languages

English, Bengali, Hindi and German (Basic)